MODELING NON-LINEAR LARGE SCALE STRUCTURE USING LAGRANGIAN PERTURBATION THEORY

A Dissertation
Presented to the Faculty of the Graduate School
of Cornell University
in Partial Fulfillment of the Requirements for the Degree of
Doctor of Philosophy

by
Sharvari Mahendra Nadkarni
January 2011

© 2011 Sharvari Mahendra Nadkarni

ALL RIGHTS RESERVED

MODELING NON-LINEAR LARGE SCALE STRUCTURE USING LAGRANGIAN PERTURBATION THEORY

Sharvari Mahendra Nadkarni, Ph.D.

Cornell University 2011

Lagrangian Perturbation Theory (LPT) is a powerful method to model non-linear evolution of large scale structure analytically. This thesis investigates the convergence properties of this theory by applying it to a simple test problem - the spherical top-hat. The method of Largangian re-expansions is introduced to improve the convergence properties of the series. This method involves re-expanding the solution in overlapping time domains, each domain subject to a time of validity criteria. The results show that there is a trade-off between the Lagrangian order and number of steps; one can achieve the same accuracy with a lower order scheme and more time steps as that with a higher order scheme and a single step.

The method developed based on the top-hat is then applied to model evolution of inhomogeneous initial conditions. A numerical code is developed and tested. Tests of convergence with Lagrangian order, step size and grid size are presented.

BIOGRAPHICAL SKETCH

Sharvari Mahendra Nadkarni was born and raised in Mumbai, India, in the spacious expanse of a university campus. She obtained a BSc in Physics at Xavier's College before heading to the Indian Institute of Technology, Powai for a Masters in Physics. During those years she participated in reading projects on binary stars and introductory cosmology. Her Masters' project focussed on the atmospheric neutrino problem. Her inclination towards astrophysics and particle physics slowly transitioned to an interest in non-linear dynamics, thanks to the popular textbook by Steve Strogatz. She came to Cornell in 2001 with an open mind with regard to the area of specialization. Devoting her initial years in Cornell to experimental nano-biophysics, Sharvari decided, in her third year, that theory was her calling. She switched from nanometer scales to mega parsec scales and transitioned to cosmology. She spent the next six years on a long, winding and perturbative path in Lagrangian space. Sharvari leaves Ithaca, a place she now calls home, for India, and looks forward to pursuing exciting research in theoretical cosmology.

To all my teachers.

ACKNOWLEDGEMENTS

I would like to thank my advisor David Chernoff for his patience and guidance over the years and for always being available to talk about research. He has taught me the how to be a meticulous and self-critical scientist. I would like to thank Rachel Bean, Éanna Flanagan and Séamus Davis for serving on my committee. In addition, I would like to thank Rachel for her encouragement, interesting scientific discussions and for pointing out references that proved very useful for my research. I owe special thanks to Ira Wasserman for helping me stay on the graduation path and always urging me to think about broader applications of my work. My stay here would not have been possible without the support of the physics department. Ritchie Patterson, Saul Teukolsky and Jeevak Parpia provided support and advice in their capacity as department heads and DGS respectively. Thanks to Dan Wilcox for solving all my computer related problems; I will miss having his help. I would like to also thank Loling Song, the research associate who I worked with in my initial years here, for her mentoring.

I would like to thank all my friends who made Ithaca a very special place and Ithaca itself for being the warm place that it is. Thanks to my roommates Florencia Reali, Smita Chirputkar, Kirsten Leong and Jeandrew Brink for providing good company and interesting conversations over tea. It was fun to discuss science with Sarah Shandera, Jahan Dawlaty, Akshay Kulkarni, Amar Bhagwat, Sourish Basu, Tanja Hinderer, Paul Grabowski, Justin Vines and Manolis Papastergis. Thanks to my favorite musicians, especially A R Rahman, whose compositions always helped me keep my feet on the ground. Thanks to Krishna and Rani Athreya for making me feel at home in my first year and to Vinay and Saga Ambegaokar for making us a part of their family. Finishing the

B exam and thesis would have been impossible without Sudha, whose kindness, friendship, care and hospitality I will never be able to repay. And finally, thanks to my parents and in-laws for their patience and understanding and to Saikat for his love and support through the years.

TABLE OF CONTENTS

LIST OF TABLES

LIST OF FIGURES

CHAPTER 1

MOTIVATION AND OUTLINE

1.1 Motivation

The observed sky today shows a hierarchical pattern on large scales - galaxies aggregate to form clusters, clusters form superclusters and they are separated by large underdense voids and supervoids. The problem of modeling how exactly this structure developed from tiny seed fluctuations has been an active area of research for nearly four decades. Traditionally, perturbative methods have been restricted to linear scales and non-linear scales have been best tackled by N-body codes. However, analytical methods remain essential to highlight the physics behind simulations. Furthermore, cosmological observations have now established that the universe is accelerating, a finding that is inconsistent with the known constituents of the universe. Various explanations have been put forth to understand the origin of this acceleration, one of which is the existence of a new form of energy referred to as 'dark energy', parametrized by an equation of state w. One way of constraining the nature of dark energy is to follow the growth history of perturbations in such cosmologies. Given the plethora of phenomenological models and the time-consuming nature of N-body codes, alternate faster techniques based on perturbation schemes become especially useful for this task. In addition, numerical simulations cannot be started at very early epochs since the perturbations are small and the initial conditions can become contaminated by shot noise. In the current era of 'precision cosmology', this drawback may also prove to be significant. Therefore, analytic techniques to follow non-linear growth are necessary to serve as a bridge between linear theory and N-body codes.

The analytic description of a fluid is mainly carried out in either the Eulerian or Lagrangian frame. In the Eulerian frame, the density and velocity are the two main dependent variables and they are expressed as functions of fixed grid coordinates. On the other hand, the Lagrangian frame moves with the fluid and the main dependent variable is the position which is expressed as a function of the initial particle label. The density and velocity are reconstructed from their exact non-perturbative definitions, making the Lagrangian description a powerful tool to model non-linear evolution. This thesis focuses on perturbation theory in the Lagrangian frame i.e. Lagrangian Perturbation Theory (LPT) as a tool to model non-linearities.

1.2 Outline of the thesis

The thesis is outlined as follows.

- Chapter 2 gives a basic introduction to cosmological structure formation and a very brief introduction to LPT.
- Chapter 3 examines convergence properties of the Lagrangian expansion. It was shown in a paper by Sahni and Shandarin [70] that the LPT series did not converge when applied to spherical voids. This issue is examined in detail by applying the techniques of complex analysis to the exact solution of the spherical top-hat. It is demonstrated that to ensure convergence, it is always necessary to re-expand the solution in

overlapping time domains, each domain subject to a time of validity criteria. The variation of the leading order error with Lagrangian order and step size is characterized. The results indicate that the accuracy achieved by a higher order scheme with a single step can be achieved by a lower order scheme but with multiple steps.

- The results presented in the previous chapter are based on a spherical top-hat model. However, inhomogeneities in the universe arise from fluctuations in a Gaussian random field. Chapter 4 outlines the scheme to handle generic initial conditions and also serves as a documentation of a numerical code that has been developed and tested. The code is capable of evolving generic initial density and velocity perturbations using LPT expansions, in principle up to any order. Tests of convergence are presented. One section in this chapter is still under debate. The extensive appendices give the exact algorithm of implementing the Lagrangian scheme with multiple steps.
- Chapter 5 gives very preliminary results of an application of the code. If there were no perturbations at the initial time, then linear theory predicts simple relation between the density and velocity divergence fields. Based on the spherical top-hat evolution, this density-velocity relation is extended to non-linear densities. This result improves upon previous attempts by Bernardeau [10] and Bilicki and Chodorowski [12]. This evolution is compared across cosmologies with different dark energy equation of state and I propose that such a relation can be used to constrain the dark energy equation of state.

Chapter 3 has been accepted for publication in the *Monthly Notices of the Royal Astronomical Society* (MNRAS). Chapter 4 will be submitted to MNRAS.

One must note here that one of the major drawbacks of LPT is its inability to track evolution once particle trajectories have crossed. The techniques focussed on in this thesis do not address this issue. Some other approximations (which might involve including pressure effects) will have to be invoked to handle evolution beyond shell crossing.

1.3 Scope and applications

A good part of this thesis discusses the error control parameters of an LPT based scheme. One may well ask why a tool based on an approximate, perturbative scheme needs such a detailed error control analysis. The justification follows. As mentioned earlier, simulations have two main drawbacks; they are time consuming and limited by shot noise, which arises from the errors made in the discrete representation of a continuous density field. Correspondingly, one can think of two limits of application for this tool. One limit is where precision is not a premium, but time is. Applications which require simulations over a wide range of scales (big boxes) or a wide range of parameter space fall under this category. The second limit is where one requires precision (which usually comes at the cost of time) that cannot be provided by numerical simulations, due to their discrete particle nature. Simulations involving early dark energy models or evolution of primordial non-Gaussianities come under this category. Alternatively, there may be problems such as BAO reconstruction where the Lagrangian formulation is a natural choice. Even in the context of such applications, a recent paper by Carlson, Padmanabhan & White [23] emphasizes the need for error control, although they focus on Eulerian PT.

A list of possible applications are outlined below. Readers unfamiliar with the standard notations in cosmology may refer to the next chapter.

1.3.1 Reconstruction of Baryon Acoustic Oscillations (BAO)

Acoustic oscillations in the photon-baryon plasma that took place early in the history of the universe leave their mark as a peak at 150 h^{-1}Mpc in the correlation function of galaxies today. In linear theory, the scale of this peak is set by the radius of the sound horizon at decoupling which in turn depends on the cosmological parameters $\Omega_b h^{-2}$ and $\Omega_m h^{-2}$. If we assume these quantities to be well constrained by CMB data (WMAP 7-year results, Komatsu *et al* [43]) then, the BAO peak at 150 h^{-1}Mpc behaves like a standard ruler with which we can measure the angular diameter distance as a function of redshift, thus mapping out the Hubble parameter $H(z)$ and hence constraining the equation of state of dark energy. Although, in theory, a very promising probe to constrain dark energy, in practice, dynamics of galaxy clustering is not linear; non-linear effects degrade the BAO peak. Motions of the galaxies due to bulk flows towards a supercluster or away from a void tend to displace galaxies from their initial separation by about ~ 10 h^{-1}Mpc. This blurs the acoustic peak at 150 h^{-1}Mpc and correspondingly erases the higher harmonics in the power spectrum (Eisenstein, Seo, & White [33]). If the BAO signal is to be used for precision cosmology, then one must correct for such effects and reconstruct the peak.

The reconstruction involves correcting for galaxy positions, hence a natural framework to use is the Lagrangian formulation. The main contribution to the degradation comes from scales in the range $300h^{-1}$Mpc to $30h^{-1}$Mpc. Flows arising from scales larger than $300h^{-1}$Mpc correspond to a very small density contrast and displace both galaxies almost equally in the same direction. Non linearities due to clustering of haloes (scales less than $30h$Mpc^{-1}) are known to have a sub-dominant effect in degrading the peak. This range of scales is particularly well suited to be modeled by LPT. In a recent paper (Eisenstein *et al* [32]), reconstruction was performed using the Zeldovich approximation (first order LPT). The LPT based code has been developed to allow integration both forward and backward in time and taking multiple steps and/or using a higher order scheme will provide a more accurate reconstruction.

In addition to recovering the BAO peak, the same technique can also be used to reconstruct primordial fluctuations from a non-linear power spectrum (Frisch *et al* [35], Brenier *et al* [16]), although this application will require modeling scales smaller than the BAO reconstruction scales.

1.3.2 Weak lensing of high redshift supernovae

For little over a decade, Type Ia supernovae have provided compelling evidence that our universe is accelerating. The most common explanation for this is the presence of an alternate form of energy termed ‘dark energy’ described by an equation of state w. Future proposed missions such as the SuperNova Acceleration Probe (SNAP) and the Joint Dark Energy Mission (JDEM) aim to measure w precisely and determine whether or not it evolves with time by probing supernovae from higher and higher redshifts. Although the light curve of a Type Ia supernova provides an excellent standard candle to determine the luminosity distance-redshft relation, the lensing of the light due to intervening inhomogeneities degrades this relation (Holz & Wald [37]). Overdense (underdense) regions tend to magnify (demagnify) the image resulting in systematic correction to the inferred equation of state parameter w and the fractional density parameter $\Omega_{d.e}$. This effect is usually estimated by ray tracing through N-body simulations or Monte Carlo approximations to inhomogeneous universes (Vanderveld, Flanagan & Wasserman [79]). However, as the surveys improve, the maximum redshift probed will increase and it will be necessary to consider bigger simulation boxes. Although accurate, N-body simulations are time consuming and the LPT iterative scheme provides a faster approximate answer, at least for quasi-linear scales.

1.3.3 Evolution of non-Gaussian initial conditions

It is widely believed that quantum fluctuations during the inflationary epoch were responsible for seeding the perturbations that led to temperature anisotropies in the Cosmic Microwave Background (CMB) and the large scale structure (LSS) observed today. Observations are consistent with a Gaussian spectrum, predicted by the standard slow-roll, single field model of inflation. But they place only weak constraints on a non-Gaussian component. Self interactions in the standard inflation model or other non-standard mechanisms predict a non-Gaussian spectrum, providing theoretical motivation to look for such effects. Phenomenologically, this is usually written as $\langle\phi\rangle = \langle\phi_L\rangle + f_{NL}\langle\phi_L^2\rangle$, where ϕ_L represents the linear (Gaussian) gravitational potential, f_{NL} represents the parameter characterizing the degree of non-Gaussianity, $\langle\rangle$ denote averages over many ensembles (see Bartolo *et al* [5] for a detailed review). Although the simplest constraints on f_{NL} arise from temperature maps (CMB), density maps (observations of galaxies, or weak lensing maps) can act as complementary probes to constrain f_{NL}, in particular its scale dependence. Since the non-Gaussian perturbations are generated as a second order effect, any method that tracks their future evolution should include post-linear terms.

To date this problem has been tacked numerically by N-body simulations. However, N-body simulations suffer from shot noise due to their discrete particle representation of a continuous density field. This prevents them from starting at high redshifts ($z \sim 1000$) when the density contrasts are small. Furthermore, shot noise effects are worse for smaller scales (Baugh, Gaztañaga, Efstathiou [6], Sirko [73]). These are also the scales which enter the non-linear regime earlier, making the shot noise problem a serious limitation to model evolution of non-Gaussianities. Most N-body codes that track growth of non-Gaussian seeds start at $z \sim 50$, using the Zeldovich approximation to propagate initial conditions from $z \sim 1000$ to $z \sim 50$ (for example Dalal *et al* [28], Wagner *et al* [80]. Most of these employed $256^3 - 512^3$ particles with box sizes of 600 - 800 h^{-1} Mpc. More recent simulations start at $z \sim 99$ (Sefusatti *et al*, 2010) but they need to use 1024^3 particles to model mildly non-linear scales.

The simulation tool I have developed for this thesis, is based on Lagrangian Perturbation Theory (LPT). It is an intrinsically analytic approach that deals with continuous density and velocity fields. The simulation is not limited by shot noise effects and can be started at any post equipartition epoch. The number of initial functions i.e. initial density and velocity fields does not change with the starting epoch. The code employs the method of Lagrangian re-expansions (Nadkarni-Ghosh & Chernoff, 2010) which involves re-expanding the solution at discrete time intervals and allows one to obtain accurate results even at a finite order in perturbation theory. The errors in the simulation are controlled by three parameters; the Lagrangian order, the number of time steps and the size of the grid. A subsequent work (Nadkarni-Ghosh & Chernoff, in preparation) will show how the errors of the simulation scale with each of these parameters. The simulation can be easily modified to change the dark energy equation of state, allowing for the first time a combined study of dark energy and non-Gaussian effects.

1.3.4 Evolution of early dark energy cosmologies

Early Dark Energy (EDE) models are one of the many classes of phenomenological models put forth to explain dark energy (for example Wettrich [82], Doran & Robbers [30]). In these models dark energy is allowed to have a non-negligible contribution to the energy budget as early as recombination ($z \sim 1000$). While observational constraints from BBN & CMB (Bean, Hansen & Melchiorri [7]) and CMB, SN and LSS (Doran & Robbers [30]) suggest that this contribution is small, there are theoretically motivated models that support its existence (Wetterich [81], Albrecht and Skordis [2]). Not only does EDE change the acoustic peaks in the CMB (Bean *et al* [7]) and BAO scale (Linder & Robbers [47]), it also has an effect on structure formation. Bartelmann, Doran & Wetterich [4] have investigated the effect of EDE on haloes using the Press-Schecter formalism. However, the Press-Schecter theory is a semi-analytic theory based on the spherical collapse model and can be expected to give only approximate results. A more accurate modeling of the effect of EDE on non-linear structure has been carried out by Grossi & Springel [36] and Francis, Lewis & Linder [34], using N-body simulations. However, like most N-body simulations, these were started at later redshifts ($z \sim 49$ and $z \sim 24$ respectively). If EDE is indeed non-negligible at the epoch of recombination, then it would be useful to follow evolution from $z \sim 1000$ to model its effect on structure through the early ages of the Universe. An LPT based code can perform such a task.

CHAPTER 2

A BRIEF INTRODUCTION TO STRUCTURE FORMATION

This chapter lays out the standard notation used in cosmology and gives a brief introduction to structure formation.

2.1 Homogenous and Isotropic background universe

On large scales the universe is homogenous and isotropic. Until the early 1990's it was believed that the main constituents of the universe were radiation (photons and neutrinos) and matter (baryons and dark matter). However, observations of Type Ia supernovae in the late 1990's (Riess *et al* [68], Perlmutter *et al* [65]) suggested that the universe is accelerating, a feature that cannot be produced by radiation or matter. Since then three main hypotheses attempting to explain the observations have emerged. These are

1. Missing sources, i.e. there exists some form of energy called 'dark energy', that is unaccounted for in the energy budget of the universe.
2. Incorrect equations or infra-red corrections, i.e. Einstein's gravity is correct on small scales (solar system), but needs to be modified on large scales.
3. Effects of backreaction, i.e. the assumption of homogeneity and isotropy, which is implicit in the analysis of observations is incorrect and the analysis must include the effects of inhomogeneities.

The first hypothesis is perhaps the most popular and can be traced back to Einstein, who originally introduced a term called the cosmological constant Λ.

His motivation was to obtain a steady-state universe, a popular cosmological model at the time, but he later withdrew it following the observations by Edwin Hubble which established that the universe was expanding. Given the need for a dark energy, this term has seen a revival in cosmology. However, attempts to understand its fundamental nature have not been fruitful yet. One possible candidate is the quantum vacuum energy, however, its theoretically estimated value is 120 orders of magnitude greater than the observed value. This has led to many phenomenological models, and the many upcoming surveys such as JDEM (Joint Dark Energy Mission) or EUCLID will help constrain these models and unravel the true nature of dark energy.

The evolution of the expanding Universe is usually described by the scale factor $a(t)$. Einstein's equations dictate that $a(t)$ obeys

$$\frac{\ddot{a}}{a} = -\frac{4\pi G}{3}\sum\left[\rho(t) + 3p(t)\right] = -\frac{4\pi G}{3}\sum\rho(t)(1+3w), \tag{2.1}$$

where $\rho(t)$ and $p(t)$ are the energy density and pressure and the sum is over all the different components of the universe. Usually the scale factor today, a_0, is set to $a_0 = 1$. The redshift z is defined as $z = 1/a - 1$. The equation of state w relates the energy density to the pressure $w = p/\rho$. Conservation of energy-momentum gives

$$\frac{d}{dt}(\rho a^3) = -p\frac{da^3}{dt}. \tag{2.2}$$

From this it can be seen that the radiation and matter energy densities scale as $\rho_\gamma \sim a^{-4}$ ($w = -1/3$), $\rho_m \sim a^{-3}$ ($w = 0$) respectively. The cosmological constant has $w = -1$. The simplest phenomenological extension of this allows w to be a constant, not necessarily -1 (Caldwell, Dave & Steinhardt [22]). For such models, the dark energy density scales as $\rho_{d.e} \sim a^{-3(1+w)}$ and these are the models considered in the last chapter of this thesis.

At early times $z \gtrsim 10^4$, the universe is radiation dominated. The baryons and dark matter are coupled to the photons through Compton scattering and structure cannot grow. The period of recombination around $z \sim 1000$ marks the epoch where the photons decouple from the matter, matter energy density dominates and structure begins to grow. Throughout the era of structure formation, the background scale factor can be assumed to only depend on matter and dark energy. The equation for the scale factor is

$$\frac{\ddot{a}}{a} = -\frac{4\pi G}{3}\left(\frac{\rho_{m,0}+\rho_{b,0}}{a^3} + (1+3w)\frac{\rho_{d.e,0}}{a^{3(1+w)}}\right), \tag{2.3}$$

where, $\rho_{m,0}$, $\rho_{b,0}$ and $\rho_{d.e,0}$ are matter, baryon and dark energy densities today and G is Newton's gravitational constant. The quantity $H = \dot{a}/a$ is called the Hubble parameter and is related to the critical density (the density needed to make the universe flat) as $H_0^2 = 8\pi G\rho_{c,0}/3$. It is customary to write the energy densities today as fraction of the critical density,

$$\Omega_{m,0} = \frac{\rho_{m,0}}{\rho_{c,0}}, \tag{2.4}$$

$$\Omega_{b,0} = \frac{\rho_{b,0}}{\rho_{c,0}}, \tag{2.5}$$

$$\Omega_{d.e,0} = \frac{\rho_{d.e,0}}{\rho_{c,0}}. \tag{2.6}$$

This puts the Einstein equation and its integrated version (the Friedmann equation) into the form

$$\frac{\ddot{a}}{a} = -\frac{H_0^2}{2}\left(\frac{\Omega_{m,0}+\Omega_{b,0}}{a^3} + (1+3w)\frac{\Omega_{d.e,0}}{a^{3(1+w)}}\right), \tag{2.7}$$

$$H^2 = H_0^2\left(\frac{\Omega_{m,0}+\Omega_{b,0}}{a^3} + \frac{\Omega_{d.e,0}}{a^{3(1+w)}}\right). \tag{2.8}$$

Observations by WMAP set $H_0 = 100h$ km/s/Mpc, $h = 0.71$, $\Omega_{m,0} = 0.26$, $\Omega_{b,0} = 0.022$, $\Omega_{d.e,0} = 0.73$ and the universe is very close to being flat (Komatsu [43]). These are the form of the equations used in this thesis, however for the rest of the discussion, baryons and dark matter are jointly referred to as matter.

2.2 Linear Growth of inhomogeneities

This section presents the basics of linear theory in the Eulerian frame, which is the most commonly used analytic method to follow growth of structure.

On very large scales the dynamics of the universe is characterized by the scale factor described in the previous section. For small scales, much less than the horizon scale, Newtonian gravity is a good approximation and the density and velocity fields obey the continuity equation, Euler's equation and Newton's law of gravity. In the absence of baryons, one can neglect pressure effects and write

$$\frac{d\rho(\mathbf{r},\mathbf{t})}{dt} = -\rho(\mathbf{r},\mathbf{t})\nabla_r \cdot \mathbf{v}(\mathbf{r},\mathbf{t}), \quad (2.9)$$

$$\frac{d\mathbf{v}(\mathbf{r},\mathbf{t})}{dt} = -\nabla_r\phi(\mathbf{r},\mathbf{t}), \quad (2.10)$$

$$\nabla_r^2\phi(\mathbf{r},\mathbf{t}) = 4\pi G\rho(\mathbf{r},\mathbf{t}). \quad (2.11)$$

Here **r** refers to the physical Eulerian coordinate and the divergence operation'$\cdot$' is with respect to this variable. d/dt refers to the total derivative $\frac{d}{dt} = \frac{\partial}{\partial t}\big|_r + \mathbf{v}\cdot\nabla_r$.

When the perturbations are small, one can expand the density, velocity and potential around the background quantities,

$$\rho(\mathbf{r},\mathbf{t}) = \rho_b(t)(1+\delta(\mathbf{r},\mathbf{t})), \quad (2.12)$$

$$\mathbf{v}(\mathbf{r},\mathbf{t}) = \mathbf{v}_b(t) + \mathbf{v}_p(\mathbf{r},\mathbf{t}), \quad (2.13)$$

$$\phi(\mathbf{r},\mathbf{t}) = \phi_b(t) + \phi_p(\mathbf{r},\mathbf{t}), \quad (2.14)$$

where ρ, **v** and ϕ refer to the density, velocity and gravitational potential respectively. The background quantities are subscripted by 'b' and perturbed quantities are subscripted by 'p'. $\delta(\mathbf{r},\mathbf{t})$ is called the fractional density and $\mathbf{v}_p$ is called the 'peculiar velocity'.

Substituting in the above system equations and keeping the first order terms gives

$$\begin{aligned}\frac{d\delta}{dt} + \nabla_r \cdot \mathbf{v} &= 0, &(2.15)\\ \ddot{\delta} + 2H(a)\dot{\delta} - \frac{3}{2}H(a)^2\Omega_m(a)\delta &= 0. &(2.16)\end{aligned}$$

It is clear from this equation that the growth of the overdensity δ depends on the background cosmology through the density parameter $\Omega_m(a)$ and the Hubble parameter $H(a)$. Therefore, measuring the growth rate of structure can provide insights into the evolution history of the universe and constrain cosmological parameters. For the case of a matter dominated universe with $\Omega_m = 1$, eq. (2.16) has two solutions $\delta^+(t) \sim a(t) \sim t^{2/3}$ and $\delta^-(t) \sim H \sim 1/t$. Usually, initial conditions are chosen such that there are no decaying modes and there are no singularities in the solution at $t = 0$. Only the growing mode $\delta^+ \sim a$ remains. This gives $\dot{\delta} = H\delta$ and relates the velocity divergence to δ as $\nabla_r \cdot \mathbf{v}_p = -H\delta$. It is common to scale the velocity divergence by the Hubble constant giving $\nabla_r \cdot \mathbf{v}'_p = -\delta$, where $\mathbf{v}'_p = \mathbf{v}_p/H$.

At linear order, extending to more general cosmologies, this relationship is written in the form

$$\nabla_r \cdot \mathbf{v}'_p = -f(\Omega_m)\delta, \qquad (2.17)$$

where $f(\Omega_m) = d\ln\delta/d\ln a$. It was shown in 1976 by Peebles [63] that for purely matter cosmologies $f(\Omega_m) \simeq \Omega_m^{0.6}$. Extensions of this relation for cosmologies with a cosmological constant performed at linear order by Lahav *et al* (1991) [44] give $f(\Omega_m, \Omega_\Lambda) \simeq \Omega^{0.6} + \Omega_\Lambda/70(1 + \Omega_m/2)$, where Ω_Λ is the density parameter for the cosmological constant.

2.3 Non-linear growth

2.3.1 Higher order Eulerian PT

When the density contrast $\delta \sim 1$, linear theory breaks down and non-linear methods need to be used. One analytic technique is the natural extension of the linear theory outlined above i.e. higher order Eulerian perturbation theory. This involves expanding the functions as

$$\delta(\mathbf{r}, t) = \sum_{n=1}^{\infty} \delta^{(n)}(\mathbf{r}, t)\epsilon^n \tag{2.18}$$

$$\Theta(\mathbf{r}, t) = \sum_{n}^{\infty} \Theta^{(n)}(\mathbf{r}, t)\epsilon^n \tag{2.19}$$

where $\Theta = \nabla \cdot \mathbf{v}_p'$ and expansion parameter ϵ is proportional to the magnitude of the initial fractional density (or scaled velocity divergence) field $\delta(\mathbf{r}, t_0)$. A detailed review of higher order Eulerian perturbation theory can be found in Bernardeau *et al* [9] and shall not be discussed further.

2.3.2 Numerical Simulations and their limitation

Numerical simulations are the most popular choice to tackle growth in the non-linear regime. The basic algorithm of a numerical N-body code involves the following steps (see for e.g. Bagla & Padmanabhan [3]):

1. Set up the initial positions and velocities of the particles.
2. Solve for the force on each particle.
3. Move the particles forward a small time step based on this force and calculate the new position and velocity.

4. Perform diagnostic check for energy conservation.
5. Repeat step 2.

Although numerical simulations do a good job at getting the right answer, they are nevertheless approximations that involve a discrete representation of a continuous density field in a finite box. They cannot represent scales larger than the box size or smaller than the inter-particle spacing. The discrete particle representation gives rise to a shot noise limit which corresponds to the smallest density contrast that can be well represented with finite number of particles. This limit is larger for scales much smaller than the size of the box i.e. shot noise is greater for small scales. The earlier the starting redshift for the simulation, the smaller the density contrast that needs to be represented and higher the required resolution (Baugh, Gaztañaga, Efstathiou [6], Scoccimarro [71], Crocce & Scoccimarro [27], Sirko[73], Smith *et al* [74]).

The transfer function gives the linear theory amplitude of fluctuations at the end of the period of recombination. Ideally, one would like to follow the growth of structure exactly from then on. However, usually the shot noise constraint prevents N-body codes from starting at very early redshifts ($z \sim 1000$) and instead the Zeldovich approximation (linear LPT) is used to propagate the initial conditions from $z \sim 1000$ to $z \sim 50$. As mentioned in the previous chapter, this can prove to be a drawback for certain applications. Improvements using higher order LPT to start the simulations have been made by Scoccimarro [71], Crocce & Scoccimarro [27], but fundamentally, numerical simulations remain shot noise limited.

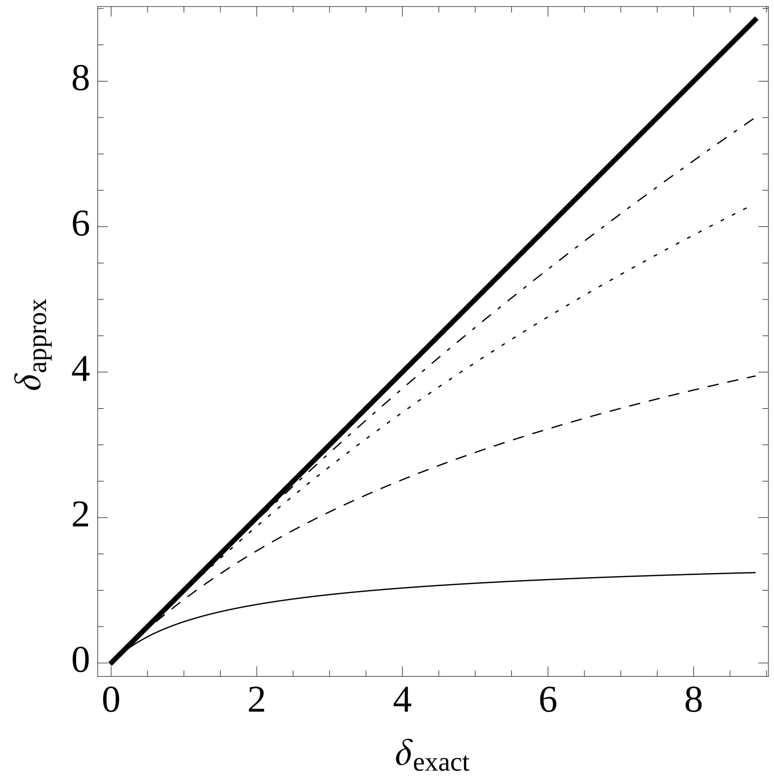

Figure 2.1: Different approximations to the density compared with the exact density from the spherical top-hat model. The linear Eulerian PT (EPT), first, second, third order LPT approximations are denoted by plain, dashed, dotted and dot-dashed lines respectively. The thick solid line denotes the exact value of the density. Note that the linear LPT performs significantly better than linear EPT because LPT is intrinsically non-linear in the density field. This makes LPT a very powerful tool to model non-linear structure. This figure is similar to fig.1 in Munshi *et al* [58].

2.3.3 Lagrangian Perturbation Theory

The other analytic approach to describe the fluid is Lagrangian Perturbation Theory. In the Lagrangian framework, the evolution of the fluid is tracked as a function of particle labels $\mathbf{X}$ and t i.e. $\mathbf{r} = \mathbf{r}(\mathbf{X}, t)$. The initial Lagrangian coordinate of a particle is defined as

$$\mathbf{X} = \frac{\mathbf{r}(t_0)}{a(t_0)}, \tag{2.20}$$

where $\mathbf{r}(t_0)$ is the Eulerian position of the particle and $a(t_0)$ is the background scale factor at the initial time. Let $\rho_m(\mathbf{X}, t_0)$ be the total density at the initial time. The perturbation is characterized by two quantities; the initial fractional overdensity

$$\delta(\mathbf{X}, t_0) = \frac{\rho_m(\mathbf{X}, t_0)}{\rho_{m,0}} - 1 \tag{2.21}$$

and the initial peculiar velocity

$$\mathbf{v}(\mathbf{X}, t_0) = \dot{\mathbf{r}}(t_0) - \dot{a}_0\mathbf{X}. \tag{2.22}$$

Below horizon scales, the equations obeyed by the position vector $\mathbf{r}(\mathbf{X}, t)$ are

$$\nabla_r \cdot \ddot{\mathbf{r}} = -4\pi G\left[\rho_m(\mathbf{r}, t) + \rho_{d.e}(t)(1 + 3w)\right], \tag{2.23}$$

$$\nabla_r \times \ddot{\mathbf{r}} = 0., \tag{2.24}$$

where $\rho_m(\mathbf{r}, t)$ and $\rho_{d.e}(t)$ are the total matter and dark energy densities respectively at time t and G is Newton's gravitational constant. ∇_r is the Eulerian gradient operator and the 'dot' denotes derivative with respect to time.

Conservation of mass implies that the density at any time t is given as

$$\rho_m(\mathbf{X}, t) = \frac{\rho_m(\mathbf{X}, t_0)J(\mathbf{X}, t_0)}{J(\mathbf{X}, t)}, \tag{2.25}$$

where $J(\mathbf{X}, t) = Det\left(\frac{\partial r_i}{\partial X_j}\right)$ is the Jacobian of the transformation relating the Eulerian and Lagrangian coordinate systems. This transformation is well defined until orbit crossing.

$\mathbf{r}(\mathbf{X}, t)$ is the main variable solved for in the Lagrangian framework. Note, that the density is reconstructed using exact definitions. Therefore, even though

$\mathbf{r}(\mathbf{X}, t)$ is solved for perturbatively, a first order expansion in the displacement field gives a higher than linear order approximation to the density field. Figure 2.1 shows the benefit of the LPT approximation over Eulerian PT for the case of a spherical top-hat system. The spherical top-hat system can be solved exactly and is described in detail in the next chapter.

CHAPTER 3

EXTENDING THE DOMAIN OF VALIDITY OF LPT

The material presented in this chapter has been accepted for publication in MNRAS (Nadkarni-Ghosh & David Chernoff [59]). The aim in this paper was to understand the convergence properties of the Lagrangian series. The exact solution for a spherical top-hat system is analyzed using the techniques of complex analysis. Based on this analysis, it is possible to predict exactly how long the series solution will be valid given general initial conditions. This time is referred to as the 'time of validity'. It is demonstrated that to ensure convergence, it is always necessary to re-expand the solution in overlapping time domains, each domain subject to the time of validity criteria. The errors in the solution are characterized as a function of Lagrangian order and time steps. It is found that a higher order scheme with fewer time steps can achieve the same accuracy as a lower order scheme with more time steps. This is an important aspect of the scheme that may be exploited when evolving inhomogeneous initial conditions with a numerical simulation.

3.1 Abstract

We investigate convergence of Lagrangian Perturbation Theory (LPT) by analyzing the model problem of a spherical homogeneous top-hat in an Einstein-deSitter background cosmology. We derive the formal structure of the LPT series expansion, working to arbitrary order in the initial perturbation amplitude. The factors that regulate LPT convergence are identified by studying the exact, analytic solution expanded according to this formal structure. The key methodology is to complexify the exact solution, demonstrate that it is analytic and apply well-known convergence criteria for power series expansions of analytic functions. The "radius of convergence" and the "time of validity" for the LPT expansion are of great practical interest. The former describes the range of initial perturbation amplitudes which converge over some fixed, future time interval. The latter describes the extent in time for convergence of a given initial amplitude. We determine the radius of convergence and time of validity for a full sampling of initial density and velocity perturbations.

This analysis fully explains the previously reported observation that LPT fails to predict the evolution of an underdense, open region beyond a certain time. It also implies the existence of other examples, including overdense, closed regions, for which LPT predictions should also fail. We show that this is indeed the case by numerically computing the LPT expansion in these problematic cases.

The formal limitations to the validity of LPT expansion are considerably more complicated than simply the first occurrence of orbit crossings as is often assumed. Evolution to a future time generically requires re-expanding the

solution in overlapping domains that ultimately link the initial and final times, each domain subject to its own time of validity criterion. We demonstrate that it is possible to handle all the problematic cases by taking multiple steps (LPT re-expansion).

A relatively small number ($\sim$ 10) of re-expansion steps suffices to satisfy the time of validity constraints for calculating the evolution of a non-collapsed, recombination-era perturbation up to the current epoch. If it were possible to work to infinite Lagrangian order then the result would be exact. Instead, a finite expansion has finite errors. We characterize how the leading order numerical error for a solution generated by LPT re-expansion varies with the choice of Lagrangian order and of time step size. Convergence occurs when the Lagrangian order increases and/or the time step size decreases in a simple, well-defined manner. We develop a recipe for time step control for LPT re-expansion based on these results.

3.2 Introduction

Understanding the non-linear growth of structure in an expanding universe has been an active area of research for nearly four decades. Simulations have been instrumental in illustrating exactly what happens to an initial power spectrum of small fluctuations but analytic methods remain essential for elucidating the physical basis of the numerical results. Perturbation theory, in particular, is an invaluable tool for achieving a sophisticated understanding.

The Eulerian and Lagrangian frameworks are the two principal modes of description of a fluid. The fundamental dependent variables in the Eulerian treatment are the density $\rho(\mathbf{x}, t)$ and velocity $\mathbf{v}(\mathbf{x}, t)$ expressed as functions of the grid coordinates $\mathbf{x}$ and time t, the independent variables. In perturbation theory the dependent functions are expanded in powers of a small parameter. For cosmology that parameter typically encodes a characteristic small spatial variation of density and/or velocity with respect to a homogeneous cosmology at the initial time. As a practical matter, the first-order perturbation theory becomes inaccurate when the perturbation grows to order unity. Subsequently one must work to higher order to handle the development of non-linearity (see Bernardeau *et al* [9] for a review) or adopt an alternative method of expansion.

In the Lagrangian framework, the fundamental dependent variable is the physical position of a fluid element or particle (terms used interchangeably here). The independent variables are a set of labels $\mathbf{X}$, each of which follows a fluid element, and the time. Usually $\mathbf{X}$ is taken as the position of the element at some initial time but other choices are possible. In any case, the physical position and velocity of a fluid element are $\mathbf{r} = \mathbf{r}(\mathbf{X}, t)$ and $\dot{\mathbf{r}}(\mathbf{X}, t)$, respectively. Knowledge of the motion of each fluid element permits the full reconstruction of the Eulerian density and velocity fields. In cosmological applications of Lagrangian perturbation theory (LPT), just like Eulerian perturbation theory, the dependent variables are expanded in terms of initial deviations with respect to a homogeneous background. The crucial difference is that the basis for the expansion is the variation in the initial position and position-derivative not the variation in the initial fluid density and velocity. The Eulerian density and velocity may be reconstructed from knowledge of the Lagrangian position using exact non-perturbative definitions. A linear approximation to the displacement field results in a non-linear expression for the density contrast. The Lagrangian description is well-suited to smooth, well-ordered initial conditions; a single fluid treatment breaks down once particle crossings begin, caustics form and the density formally diverges.

First-order LPT was originally introduced by Zeldovich [84] to study the formation of non-linear structure in cosmology. In his treatment the initial density field was taken to be linearly proportional to the initial displacement field (the "Zeldovich approximation"). These results were extended by many authors (Moutarde [57]; Buchert [20]; Bouchet *et al* [15]; Buchert & Elhers [21]; Buchert [17]; Munshi *et al* [58]; Catelan [24]; Buchert [18]; Bouchet [14]; Bouchet [13]; Elhers & Buchert [31]). The work pioneered by Bouchet focused on Zeldovich initial conditions and established the link between LPT variables and statistical observables. The work by Buchert as well as the paper by Ehlers & Buchert [31] formalized the structure of the Newtonian perturbative series for arbitrary initial conditions. A general relativistic version of the Zeldovich approximation was developed by Kasai [40] and other relativistic descriptions of the fluid in its rest frame were investigated by Matarrese & Terranova [53] and Matarrese *et al*([52, 51]). LPT has been used for many applications including, recently, the construction of non-linear halo mass functions by Monaco [55] and Scoccimarro & Sheth [72].

Not much has been written about the convergence of LPT although LPT expansions are routinely employed. Sahni & Shandarin [70] pointed out that the formal series solution for the simplest problem, the spherical top-hat, did not converge for the evolution of homogeneous voids. Figure 3.1 illustrates the conundrum that the LPT approximations diverge from the exact solution in a manner that worsens as the order of the approximation increases. The details will be described in the next section.

This paper explores LPT convergence for the spherical top-hat and identifies the root cause for the lack of convergence. The analysis naturally suggests a means of extending the range of validity of LPT. This generalization of LPT guarantees convergence to the exact solution of the model problem at all times prior to the occurrence of the first caustic.

Tatekawa [77] attempted to treat the divergence by applying the Shanks transformation to the LPT series. Although non-linear transformations can sum a divergent series, the correct answer is not guaranteed; comparison of several different methods is usually necessary to yield trustworthy results. Other approaches include the Shifted-Time-Approximation (STA) and Frozen-Time-Approximation (FTA) which have been investigated by Karakatsanis *et al* [39]. These schemes modify lower order terms to mimic the behavior of higher order terms and/or extend the range of applicability in time. None of these techniques are considered here.

The organization follows: §3.3 sketches the model problem, the evolution of a uniform sphere in a background homogeneous Einstein-deSitter cosmology. The LPT equations, the structure of the formal series and the term-by-term solution are outlined. §3.4 discusses the complexification of the LPT solution and convergence of the series. This section introduces the "radius of convergence" and the "time of validity" for LPT. §3.5 outlines the real and complex forms of the parametric solution and sets forth the equations that must be solved to locate the poles which govern the convergence. §3.6 presents numerical results for the time of validity and radius of convergence for a full range of possible initial conditions for the top-hat. The notion of mirror model symmetry is introduced and used to explain a connection in the convergence for

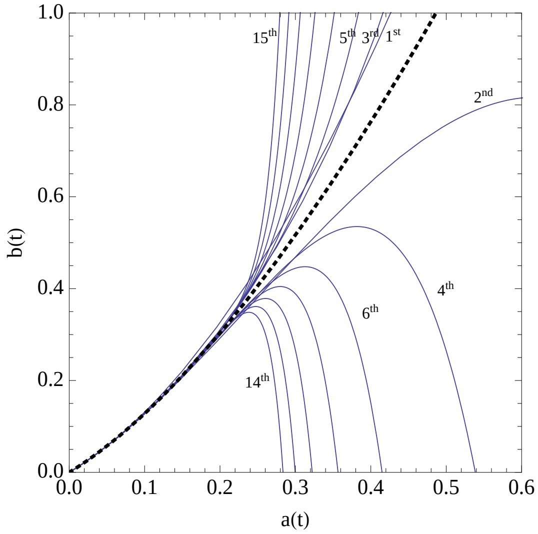

Figure 3.1: The time-dependent scale factor b of an initial spherical top-hat perturbation is plotted as a function of the background scale factor a. The perturbation is a pure growing mode, i.e. the density and velocity perturbations vanish at $t = 0$. The black dotted line is the exact solution. The smooth blue lines are the LPT results obtained by working successively to higher and higher order. Series with even (odd) final order lie below (above) the exact solution. Roughly speaking, LPT converges only for $a \lesssim 0.2$. Beyond that point *the higher order approximations deviate from the exact solution more than lower order ones*.

open and closed models. §3.7 shows that the time of validity may be extended by re-expanding the solution in overlapping domains that ultimately link the initial and final times, each domain subject to an individual time of validity criterion. The feasibility of this method is demonstrated in some examples. §3.8 summarizes the work.

3.3 The model problem and formal series solution

This section describes the governing equations, the initial physical conditions, the formal structure of the LPT series solution and the order-by-order solution.

3.3.1 Newtonian treatment

Consider evolution on sub-horizon scales after recombination in a matter-dominated universe. A Newtonian treatment of gravity based on solving Poisson's equation for the scalar potential and on evaluating the force in terms of the gradient of the potential gives an excellent approximation for non-relativistic dynamics. When there are no significant additional forces on the fluid element (e.g. pressure forces) then it is straightforward to eliminate the gradient of the potential in favor of $\ddot{\mathbf{r}}$, the acceleration. The governing equations are

$$\nabla_x \cdot \ddot{\mathbf{r}} = -4\pi G \rho(\mathbf{x}, t) \tag{3.1}$$

$$\nabla_x \times \ddot{\mathbf{r}} = 0 \tag{3.2}$$

where $\rho(\mathbf{x}, t)$ is the background plus perturbation density, G is Newton's gravitational constant and ∇_x is the Eulerian gradient operator. In the Lagrangian treatment, the independent variables are transformed $(\mathbf{x}, t) \rightarrow (\mathbf{X}, t)$ and the particle position $\mathbf{r} = \mathbf{r}(\mathbf{X}, t)$ adopted as the fundamental dependent quantity. For clarity note that $\mathbf{x}$ refers to a fixed Eulerian grid not a comoving coordinate.

3.3.2 Spherical top-hat

The starting physical configuration is a compensated spherical perturbation in a homogeneous background cosmology. The perturbation encompasses a constant density sphere about the centre of symmetry and a compensating spherical shell. The shell that surrounds the sphere may include vacuum regions plus regions of varying density. Unperturbed background extends beyond the outer edge of the shell. Physical distances are measured with respect to the centre of symmetry. At initial time t_0 the background and the innermost perturbed spherical region (hereafter, "the sphere") have Hubble constants H_0 and H_{p0}, and densities ρ_0 and ρ_{p0}, respectively. Let $r_{b,0}$ ($r_{p,0}$) be the physical distance from the centre of symmetry to the inner edge of the background (to the outer edge of the sphere) at the initial time. Let a_0, b_0 be the initial scale factors for the background and the sphere respectively. Two sets of Lagrangian coordinates $Y = r_{b,0}/a_0$ and $X = r_{p,0}/b_0$ are defined. A gauge choice sets $a_0 = b_0$. Appendix A.1 provides a figure and gives a somewhat more detailed chain of reasoning that clarifies the construction of the physical and Lagrangian coordinate systems. The initial perturbation is characterized by the independent parameters

$$\begin{aligned} \delta &= \frac{\rho_{p0}}{\rho_0} - 1 \\ \delta_v &= \frac{H_{p0}}{H_0} - 1. \end{aligned} \tag{3.3}$$

Finally, assume that the background cosmology is critical $\Omega_0 = 1$. The perturbed sphere has

$$\Omega_{p0} = \frac{1+\delta}{(1+\delta_v)^2}. \tag{3.4}$$

The physical problem of interest here is the future evolution of an arbitrary initial state unconstrained by the past history. In general, the background and the perturbation can have different big bang times. Initial conditions with equal big bang times will be analyzed as a special case of interest and imply an additional relationship between δ and δ_v.

While the previous paragraphs summarize the set up, they eschew the complications in modeling an inhomogeneous system in terms of separate inner and outer homogeneous universes. For example, matter motions within the perturbed inner region may overtake the outer homogeneous region so that there are problem-specific limits on how long solutions for the scale factors $a(t)$ and $b(t)$ remain valid. The appendix shows that there exist inhomogeneous initial configurations for which the limitations arising from the convergence of the LPT series are completely independent of the limitations associated with collisions or crossings of inner and outer matter-filled regions. A basic premise of this paper is that it is useful to explore the limitations of the LPT series independent of the additional complications that inhomogeneity entails.

3.3.3 Equation governing scale factors

During the time that the spherical perturbation evolves as an independent homogeneous universe it may be fully described in terms of the motion of its outer edge r_p. Write

$$r_p(t) = b(t)X \tag{3.5}$$

where $b(t)$ is the scale factor and X is the Lagrangian coordinate of the edge. The initial matter density of the homogeneous sphere $\rho(X, t_0) = \rho_{p0} = \rho_0(1 + \delta)$. The physical density of the perturbation at time t is

$$\rho(X, t) = \frac{\rho(X, t_0)J(X, t_0)}{J(X, t)} \tag{3.6}$$

where the Jacobian of the transformation relating the Lagrangian and physical spaces is

$$J(X, t) = \det\left(\frac{\partial \vec{r}}{\partial \vec{X}}\right). \tag{3.7}$$

Since eq. (4.3) implies $J(X,t) = b(t)^3$ and the choice $a_0 = b_0$ implies $J(X,t_0) = a_0^3$ the perturbation matter density at later times is

$$\rho_p(t) = \frac{\rho_0(1+\delta)a_0^3}{b(t)^3}. \tag{3.8}$$

Substituting for ρ_p and r_p in eq. (3.1) gives

$$\frac{\ddot{b}}{b} = -\frac{1}{2}\frac{H_0^2 a_0^3(1+\delta)}{b^3} \tag{3.9}$$

with initial conditions $b(t_0) = a_0$ and $\dot{b}(t_0) = \dot{a}_0(1+\delta_v)$. The curl of the acceleration (i.e. eq. (4.2)) vanishes by spherical symmetry. The corresponding equation for the background scale factor is

$$\frac{\ddot{a}}{a} = -\frac{1}{2}\frac{H_0^2 a_0^3}{a^3} \tag{3.10}$$

with initial conditions $a(t_0) = a_0$ and $\dot{a}(t_0) = \dot{a}_0 = a_0 H_0$. The solution for $b(t)$ will be expressed in terms of its deviations from $a(t)$.

In summary, the physical setup is an $\Omega_0 = 1$ background model and a compensated spherical top-hat (over- or underdense). The properties of interest are the relative scale factors $a(t)/a_0$ and $b(t)/a_0$ (the choice of a_0 is arbitrary and $b_0 = a_0$). The evolution of the relative scale factors is fully specified by H_0, H_{p0} and Ω_{p0} at time t_0. The perturbed physical quantities, H_{p0} and Ω_{p0}, may be equivalently specified by a choice of δ and δ_v. Appendix A.1 contains a systematic description and enumerates degrees of freedom, parameters, constraints, etc.

3.3.4 Perturbations in phase space

The initial density and velocity perturbations are taken to be of the same order in the formalism developed by Buchert [20, 17], Buchert & Ehlers [21] and Ehlers &

Buchert [31]. We assume the same ordering here. Write the initial perturbation (δ, δ_v) in terms of magnitude Δ and angle θ

$$\Delta = \sqrt{\delta^2 + \delta_v^2} \tag{3.11}$$

so that

$$\delta = \Delta \cos\theta \tag{3.12}$$

$$\delta_v = \Delta \sin\theta. \tag{3.13}$$

To map physical perturbations (δ, δ_v) in a unique manner to (Δ, θ) adopt the ranges $\Delta \geq 0$ and $-\pi < \theta \leq \pi$. Figure 3.2 (left panel) shows the phase space of initial perturbations. Since density is non-negative the regime of physical interest is $\delta \geq -1$. Open (closed) models with positive (negative) total energy are the regions that are unshaded (shaded). Initially expanding models, $1 + \delta_v > 0$, lie above the horizontal dashed line. The right panel of figure 3.2 summarizes the overall evolution of the system. The initial choice of δ and δ_v dictates the trajectory in the plane. Cosmologically relevant initial conditions generally assume there to be no perturbation at $t = 0$. We adopt the name "Zeldovich" initial conditions for models that satisfy this condition. This establishes a specific relation between δ and δ_v which is indicated by the sold blue line. The exact mathematical relationship is given in §3.6.4. Starting from a general initial point (δ, δ_v), the system as it evolves traces out a curve in phase space indicated by the blue arrows. There are three fixed points visible. The origin $(\delta, \delta_v) \equiv (0, 0)$, which corresponds to a unperturbed background model, is a saddle point. The vacuum static model at point $(-1, -1)$ is a unstable node and the vacuum, expanding model at $(-1, 0.5)$ is a degenerate attracting node. Far to the right and below the dashed line the models collapse to a future singularity. The phase portrait illustrates that the trajectories either converge to the vacuum,

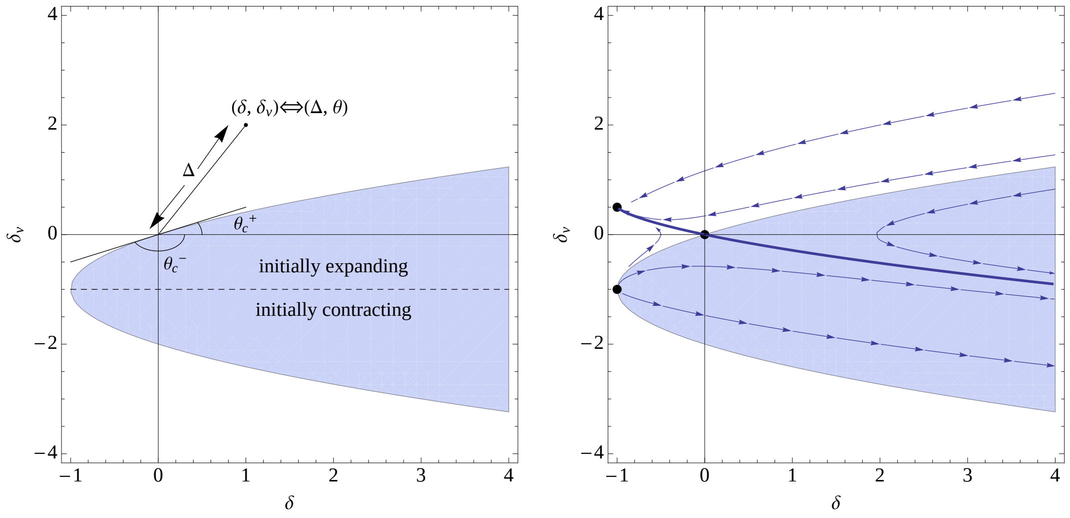

Figure 3.2: Phase diagram of density and velocity perturbations (δ, δ_v). Physical initial conditions require $-1 < \delta < \infty$ and $-\infty < \delta_v < \infty$. The left panel highlights the qualitatively different initial conditions. The shaded (unshaded) region corresponds to closed (open) model with negative (positive) total energy. For small Δ, models with $\theta_c^- < \theta < \theta_c^+$ are closed. Initially expanding and contracting models are separated by the dashed horizontal line ($\delta_v = -1$). The right panel shows the evolution of δ and δ_v. The solid blue line corresponds to the "Zeldovich" condition i.e no perturbation at $t = 0$. The points $(-1, -1)$, $(-1, 0.5)$ and $(0, 0)$ are unstable, stable and saddle fixed points of the phase space flow. The flow lines (indicated by the blue vectors) converge along the Zeldovich curve either to the stable fixed point at $(-1, 0.5)$ or move parallel to the Zeldovich curve to a future density singularity. Further discussion follows in §3.6.4 and §3.7.2.

expanding model or to the singular, collapsing model. The equations that govern the flow and further relevance of the Zeldovich solution is discussed in §3.7.2 and §3.6.4.

3.3.5 Generating the Lagrangian series solution

The scale factor is formally expanded

$$b(t) = \sum_{n=0}^{\infty} b^{(n)}(t)\Delta^n \tag{3.14}$$

where $b^{(n)}$ denotes an n-th order term. The initial conditions are

$$\begin{aligned} b(t_0) &= a(t_0) && (3.15)\\ \dot{b}(t_0) &= \dot{a}_0(1+\delta_v) = \dot{a}_0(1+\Delta\sin\theta). && (3.16) \end{aligned}$$

Substitute the expansion for $b(t)$ into eq. (3.9), equate orders of Δ to give at *zeroth order*

$$\ddot{b}^{(0)} + \frac{1}{2}\frac{H_0^2 a_0^3}{b^{(0)2}} = 0 \tag{3.17}$$

which is identical in form to eq. (3.10) for the unperturbed background scale factor. The initial conditions at zeroth order:

$$\begin{aligned} b^{(0)}(t_0) &= a_0 && (3.18)\\ \dot{b}^{(0)}(t_0) &= \dot{a}_0. && (3.19) \end{aligned}$$

The equation and initial conditions for $b^{(0)}(t)$ simply reproduce the background scale factor evolution $b^{(0)}(t) = a(t)$. Without loss of generality assume that the background model has big bang time $t = 0$ so that

$$a(t) = a_0\left(\frac{t}{t_0}\right)^{2/3} = a_0\left(\frac{3H_0 t}{2}\right)^{2/3}. \tag{3.20}$$

At *first order*

$$\ddot{b}^{(1)} - \frac{H_0^2 a_0^3 b^{(1)}}{a^3} = -\frac{1}{2}\frac{H_0^2 a_0^3\cos\theta}{a^2} \tag{3.21}$$

and, in general,

$$\ddot{b}^{(n)} - \frac{H_0^2 a_0^3 b^{(n)}}{a^3} = S^{(n)} \tag{3.22}$$

where $S^{(n)}$ depends upon lower order approximations ($b^{(0)}, b^{(1)} \ldots b^{(n-1)}$) as well as θ. The first few are:

$$\begin{aligned}
S^{(2)} &= -\frac{1}{2}\frac{H_0^2 a_0^3}{a^4}\left[b^{(1)}\left\{3b^{(1)} - 2a\cos\theta\right\}\right] && (3.23)\\
S^{(3)} &= -\frac{1}{2}\frac{H_0^2 a_0^3}{a^5}\left[b^{(1)}\left\{-4\left(b^{(1)}\right)^2 + 6ab^{(2)} + 3ab^{(1)}\cos\theta\right\} - 2a^2 b^{(2)}\cos\theta\right] && (3.24)\\
S^{(4)} &= -\frac{1}{2}\frac{H_0^2 a_0^3}{a^6}\left[\left(b^{(1)}\right)^2\left\{5\left(b^{(1)}\right)^2 - 12ab^{(2)} - 4ab^{(1)}\cos\theta\right\} + \right.\\
&\qquad \left. 6a^2 b^{(1)}\left\{b^{(3)} + b^{(2)}\cos\theta\right\} + 3a^2\left(b^{(2)}\right)^2 - 2a^3 b^{(3)}\cos\theta\right]. && (3.25)
\end{aligned}$$

These terms can be easily generated by symbolic manipulation software. The initial conditions are

$$\begin{aligned}
b^{(1)}(t_0) &= 0 && (3.26)\\
\dot{b}^{(1)}(t_0) &= \dot{a}_0 \sin\theta && (3.27)
\end{aligned}$$

and for $n > 1$

$$\begin{aligned}
b^{(n)}(t_0) &= 0 && (3.28)\\
\dot{b}^{(n)}(t_0) &= 0. && (3.29)
\end{aligned}$$

The ordinary differential equations for $b^{(n)}$ may be solved order-by-order.

To summarize, the structure of the hierarchy and the simplicity of the initial conditions allows the evaluation of the solution at any given order in terms of the solutions with lower order. This yields a formal expansion for the scale factor of the sphere

$$b = \sum_{n=0}^{\infty} b^{(n)}(t)\Delta^n \qquad (3.30)$$

which encapsulates the Lagrangian perturbation treatment. The right hand size explicitly depends upon the size of the perturbation and time and implicitly upon a_0, H_0, and θ. This hierarchy of equations is identical to that generated by the full formalism developed by Buchert and collaborators when it is applied to the top-hat problem. The convergence properties in time and in Δ are distinct; a simple illustrative example of this phenomenon is presented in Appendix A.2.

3.4 Convergence properties of the LPT series solution

The series solution outlined in the previous section does not converge at all times. Figure 3.1 is a practical demonstration of this non-convergence for the case of an expanding void. An understanding of the convergence of the LPT series is achieved by extending the domain of the expansion variable Δ from the real positive axis to the complex plane.

3.4.1 Complexification

The differential eq. (3.9) and initial conditions for the physical system are

$$\begin{aligned} \ddot{b}(t) &= -\frac{1}{2}\frac{H_0^2 a_0^3 (1+\Delta\cos\theta)}{b(t)^2} \\ b(t_0) &= a_0 \\ \dot{b}(t_0) &= \dot{a}_0(1+\Delta\sin\theta) \end{aligned} \tag{3.31}$$

where t, $b(t)$, Δ and all zero-subscripted quantities are real. This set may be extended by allowing Δ and b to become complex quantities, denoted hereafter, $\boldsymbol{\Delta}$ and $\mathbf{b}$, while the rest of the variables remain real. The complex set is

$$\begin{aligned} \ddot{\mathbf{b}}(t) &= -\frac{1}{2}\frac{H_0^2 a_0^3 (1+\boldsymbol{\Delta}\cos\theta)}{\mathbf{b}(t)^2} \\ \mathbf{b}(t_0) &= a_0 \end{aligned}$$

$$\dot{\mathbf{b}}(t_0) \quad = \quad \dot{a}_0(1 + \mathbf{\Delta} \sin\theta). \tag{3.32}$$

The theory of differential equations (for example, Chicone [25]) guarantees that the solution to a real initial value problem is unique and smooth in the initial conditions and parameters of the equation and can be extended in time as long as there are no singularities in the differential equation (hereafter, the maximum extension of the solution). First, note that each complex quantity in eq. (3.32) may be represented by a real pair, i.e. $\mathbf{b} = u+iv$ by pair $\{u, v\} = \{\Re\mathbf{b}, \Im\mathbf{b}\}$ and $\mathbf{\Delta} = x + iy$ by pair $\{x, y\} = \{\Re\mathbf{\Delta}, \Im\mathbf{\Delta}\}$. The basic theory implies continuity and smoothness of solution u and v with respect to initial conditions and parameters x and y. Second, observe that the Cauchy-Riemann conditions $u_x = v_y$ and $u_y = -v_x$ are preserved by the form of the ordinary differential equation. Since the initial conditions and parameter dependence are holomorphic functions of $\mathbf{\Delta}$ it follows that $\mathbf{b}(t, \mathbf{\Delta})$ is a holomorphic function of $\mathbf{\Delta}$ at times t within the maximum extension of the solution.

Inspection shows that the differential equation is singular only at $\mathbf{b} = 0$. For a particular value of $\mathbf{\Delta} = \mathbf{\Delta}'$, the solution to the initial value problem can be extended to a maximum time t_{mx} such that $\mathbf{b}(\mathbf{\Delta}', t_{mx}) = 0$ or to infinity. The existence of a finite t_{mx} signals that a pole in the complex analytic function $\mathbf{b}(\mathbf{\Delta}, t)$ forms at $\mathbf{\Delta} = \mathbf{\Delta}'$ and $t = t_{mx}$. For times t such that $t_0 \leq t < t_{mx}$, the solution $b(\mathbf{\Delta}, t)$ is analytic in a small neighborhood around the point $\mathbf{\Delta}'$. Of course, there may be poles elsewhere in the complex $\mathbf{\Delta}$ plane.

The relationship between the original, real-valued physical problem and the complexified system is the following. In the original problem Δ is a real, positive quantity at t_0. LPT is a power series expansion in Δ about the origin (the point $\Delta = 0$). LPT's convergence at any time t can be understood by study of the complexified system. Consider the complex disk $\mathcal{D}$ centered on the origin and defined by $|\mathbf{\Delta}| < \Delta$. At t_0 each point in $\mathcal{D}$ determines a trajectory $\mathbf{b}(\mathbf{\Delta}, t)$ for the complexified system extending to infinity or limited to finite time $t = t_{mx}(\mathbf{\Delta})$ because of the occurrence of a pole. The time of validity is defined as $T(\Delta) = \min_{\mathcal{D}} t_{mx}$, i.e. the minimum t_{mx} over the disk. Since there are no poles in $\mathcal{D}$ at t_0 the time of validity is the span of time when $\mathcal{D}$ remains clear of any singularities. If a function of a complex variable is analytic throughout an open disk centered around a given point in the complex plane then the series expansion of the function around that point is convergent (Brown and Churchill [38]). The LPT expansion for the original problem converges for times less than the time of validity because the complex extension $\mathbf{b}(\mathbf{\Delta}, t)$ is analytic throughout $\mathcal{D}$ for $t < T(\Delta)$. If $\Delta_1 < \Delta_2$ then, in an obvious notation, the disks are nested $\mathcal{D}(\Delta_1) \subset \mathcal{D}(\Delta_2)$ and the times of validity are ordered $T(\Delta_1) \geq T(\Delta_2)$.

This idea is shown in figure 3.3. No singularities are present for the initial conditions at t_0; at t_1 a singularity is present *outside* the disk but it does not prevent the convergence of the LPT expansion with Δ equal to the disk radius shown; at t_2 a singularity is present in the disk or on its boundary and it may interfere with convergence.

A distinct but related concept is the maximum amplitude perturbation for which the LPT expansion converges at the initial time and at all intermediate times up to a given time. The radius of convergence $R_\Delta(t)$ is the maximum disk radius Δ for which $t > T(\Delta)$. Because the disks are nested if $t_1 < t_2$ then $R_\Delta(t_1) \geq R_\Delta(t_2)$.

The time of validity and the radius of convergence are inverse functions of each other. If the initial perturbation is specified, i.e. Δ is fixed, and the

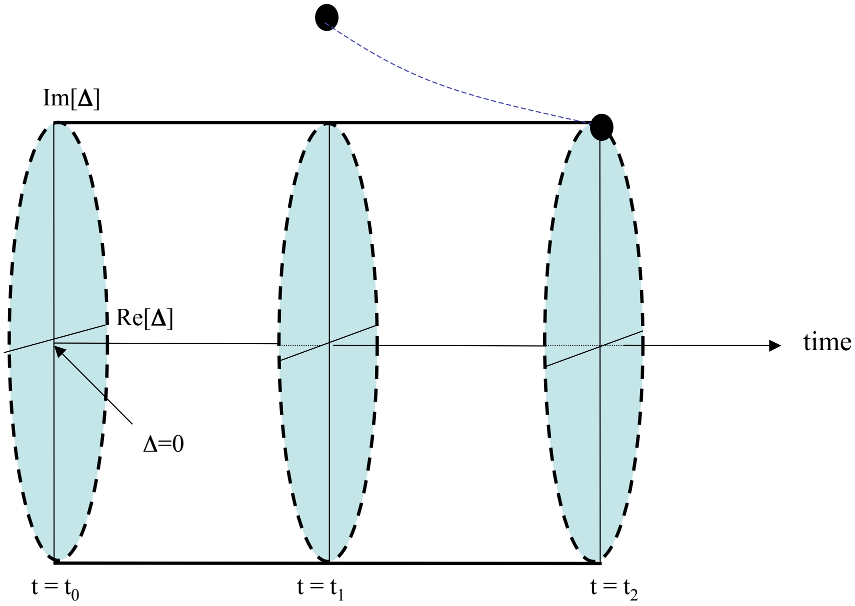

Figure 3.3: This figure is a schematic illustration of how the time of validity is determined. The initial conditions imply a specific, real Δ at time t_0. The LPT series is an expansion about $\Delta = 0$, convergent until a pole appears at some later time within the disk of radius Δ (shown in cyan) in the complex $\boldsymbol{\Delta}$ plane. Typically, the pole's position forms a curve (blue dashed) in the three dimensional space $(\Re[\boldsymbol{\Delta}], \Im[\boldsymbol{\Delta}], t)$. The black dots mark the pole at times t_1 and t_2. At t_1 the pole does not interfere with the convergence of the LPT series; at t_2 it does. The time of validity may be determined by a pole that appears within the disk without moving through the boundary (not illustrated).

question to be answered is "how far into the future does LPT work?" then the time of validity gives the answer. However, if the question is "how big an initial perturbation will be properly approximated by LPT over a given time interval?" then the radius of convergence provides the answer.

Finally, note that one can trivially extend this formalism to deal with time intervals in the past.

3.4.2 Calculating radius of convergence and time of validity

The following recipe shows how to calculate the radius of convergence $R_\Delta(t)$ and the time of validity $T(\Delta)$ efficiently. Fix a_0, H_0, t_0 and θ; these are all real constants set by the initial conditions. Assume that it is possible to find $\mathbf{b}(\mathbf{\Delta}, t)$ for complex $\mathbf{\Delta}$ and real t by solving eq. (3.32). There exist explicit expressions for $\mathbf{b}$ as will be shown later.

Start with $t = t_0$ and $R_\Delta(t) = \infty$. The iteration below maps out $R_\Delta(t)$ by making small increments in time δt.

- Store old time $t_{previous} = t$, choose increment δt and form new time of interest $t = t_{previous} + \delta t$.
- Locate all the $\mathbf{\Delta}$ which solve $\mathbf{b}(\mathbf{\Delta}, t) = 0$. The roots correspond to poles in the complex function. Find the root closest to the origin and denote its distance as $|\mathbf{\Delta}_{near}|$.
- The radius of convergence is $R_\Delta(t) = \min(|\mathbf{\Delta}_{near}|, R_\Delta(t_{previous}))$.
- Continue.

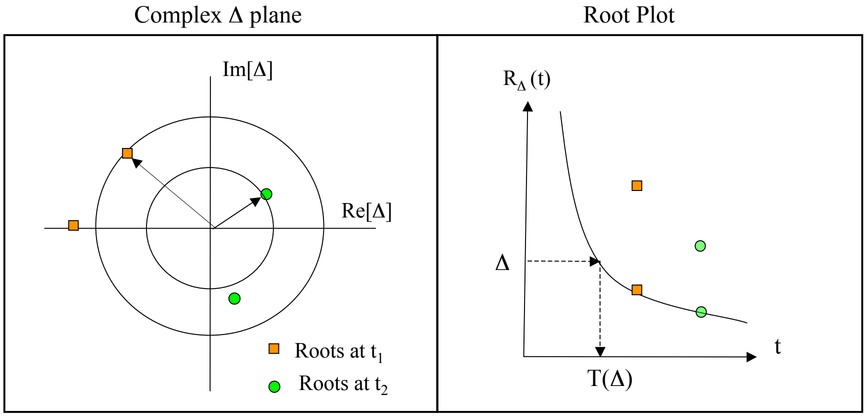

Figure 3.4: A schematic illustration of the radius of convergence and the time of validity. The left panel shows the location of poles in the complex $\mathbf{\Delta}$ plane at times t_1 and t_2, denoted by orange squares and green dots, respectively. At a fixed time, the pole nearest the origin determines the disk (black circle) within which a series expansion about the origin converges. The right panel shows $|\mathbf{\Delta}|$ for t_1 and t_2. The black line is $R_\Delta(t)$, the minimum $|\mathbf{\Delta}|$ calculated for a continuous range of times (where t_0, the initial time, lies far to the left). The arrows show how the time of validity is inferred for a given Δ.

Since R_Δ is decreasing, the inversion to form $T(\Delta)$ is straightforward. Figure 3.4 shows a schematic cartoon of the construction process.

3.5 Explicit solutions

The usual parametric representation provides an efficient method to construct an explicit complex representation for $\mathbf{b}(\mathbf{\Delta}, t)$.

3.5.1 Real (physical) solutions

The original system eq. (3.31) depends upon a_0, H_0, θ and Δ. The assumed Einstein-deSitter background has $a_0 > 0$ and $\dot{a}_0 > 0$; as defined, the perturbation amplitude $\Delta \geq 0$ and the relative density and velocity components are determined by phase angle θ with $-\pi < \theta \leq \pi$. The quantity $(1 + \Delta\cos\theta)$ is proportional to total density and must be non-negative. The sign of $\dot{b}_0$ is the sign of $1 + \Delta\sin\theta$ and encodes expanding and contracting initial conditions.

Briefly reviewing the usual physical solution, the integrated form is

$$\dot{b}^2 = H_0^2 a_0^3 \left[\frac{(1 + \Delta\cos\theta)}{b} + \frac{(1 + \Delta\sin\theta)^2 - (1 + \Delta\cos\theta)}{a_0} \right]. \tag{3.33}$$

The combination

$$E(\Delta, \theta) = (1 + \Delta\sin\theta)^2 - (1 + \Delta\cos\theta) \tag{3.34}$$

is proportional to the total energy of the system. If $E > 0$ the model is open and if $E < 0$ it is closed and will re-collapse eventually. Figure 3.2 shows the parabola $E = 0$ which separates open and closed regions. For infinitesimal Δ the line of division has slope $\tan\theta = 1/2$. Models with $\theta \in [\theta_c^-, \theta_c^+] = [-\pi + \tan^{-1}(1/2), \tan^{-1}(1/2)] = [-2.68, 0.46]$ are closed while those outside this range are open.

There are four types of initial conditions (positive and negative E, positive

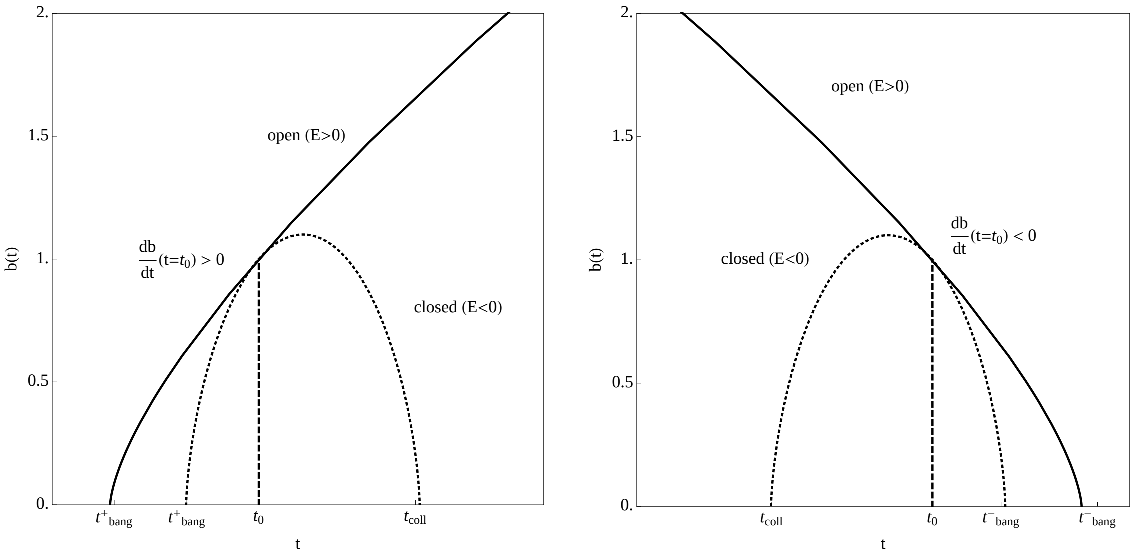

Figure 3.5: Scale factor as a function of time. The initial conditions ($b_0 = a_0 = 1$ and varying $\dot{b}_0$) are given at time t_0 (dashed blue line). The left (right) panel illustrates initially expanding (contracting) models. $t^{\pm}_{bang}$ corresponds to $\eta = 0$; t_{coll} to $\eta = 2\pi$. For expanding solutions $t_{age} = t_0 - t^{+}_{bang}$ is the time interval since the initial singularity and t_{coll} is the future singularity for closed models. For contracting solutions $t_{age} = t^{-}_{bang} - t_0$ is the time until the final singularity and t_{coll} is the past singularity for closed models.

and negative $\dot{b}_0$) and four types of solutions, shown schematically in figure 3.5. The solutions have well-known parametric forms involving trigonometric functions of angle η or $i\eta$ (see Appendix A.3). The convention adopted here is that the singularity nearest the initial time t_0 coincides with $\eta = 0$ and is denoted t^{+}_{bang} (t^{-}_{bang}) for initially expanding (contracting) solutions (see figure 3.5). The time interval between the singularity and t_0 is $t_{age} = |t_0 - t^{\pm}_{bang}| \geq 0$.

The parametric solution for the models can be written as

$$b(\eta, \Delta, \theta) \quad = \quad \frac{a_0}{2} \frac{(1 + \Delta \cos\theta)}{[-E(\Delta, \theta)]} (1 - \cos\eta)$$

$$t(\eta, \Delta, \theta) \quad = \quad t_0 \pm \left(\frac{1}{2H_0} \frac{(1 + \Delta \cos\theta)}{[-E(\Delta, \theta)]^{3/2}} (\eta - \sin\eta) - t_{age}(\Delta, \theta) \right). \tag{3.35}$$

The plus and minus signs give the solution for initially expanding and initially contracting models respectively. Parameter η is purely real for closed solutions and purely imaginary for open solutions. The distance to the nearest singularity is

$$t_{age} = \int_{b=0}^{b=a_0} \frac{db}{[\dot{b}^2]^{1/2}} = \frac{1}{H_0} \int_{y=0}^{y=1} \frac{dy}{[(1 + \Delta\cos\theta)y^{-1} + E(\Delta, \theta)]^{1/2}}. \tag{3.36}$$

The second equality uses eq. (3.33) and the substitution $y = b/a_0$.

3.5.2 Complex extension

To extend the above parametric solution to the complex plane, one might guess the substitution $\Delta \to \Delta e^{i\phi}$ where $-\pi < \phi \leq \pi$ in eq. (3.35) and eq. (3.36). The physical limit is $\phi = 0$. However, this leads to two problems. First, the integral for t_{age} can have multiple extensions that agree for physical $\phi = 0$ but differ elsewhere including the negative real axis. This is tied to the fact that the operations of integration and substitution $\Delta \to \Delta e^{i\phi}$ do not commute because of the presence of the square root in the expression for t_{age}. A second related problem is the presence of multiple square roots in the parametric form for t. These give rise to discontinuities along branch cuts such that one parametric form need not be valid for the entire range of ϕ, but instead the solution may switch between different forms. Directly extending the parametric solution is cumbersome.

However, the original differential eq. (3.32) is manifestly single-valued. The equation can be integrated forward or backward numerically to obtain the correct solution for complex $\mathbf{\Delta}$. One can then match the numerical solution to the above parametric forms to select the correct branch cuts. This procedure was implemented to obtain the form for all $\mathbf{\Delta}$ and θ. The main result is that the solution space for all θ and $\mathbf{\Delta}$ is completely spanned by complex extensions of the two real parametric forms which describe initially expanding and contracting solutions. The expressions for $\mathbf{t}_{age}$ and details are given in Appendix A.3.3.

The traditional textbook treatment relating physical cosmological models with real $\Omega > 1$ and $\Omega < 1$ typically invokes a discrete transformation $\eta \rightarrow i\eta$ in the parametric forms and one verifies that this exchanges closed and open solutions. However, starting from the second order differential equation it is straightforward to use the same type of reasoning as above to construct an explicit analytic continuation from one physical regime to the other.

In addition, note that the differential equation and its solution remain unchanged under the simultaneous transformations $\mathbf{\Delta} \rightarrow -\mathbf{\Delta}$ and $\theta \rightarrow \theta + \pi$. Every complex solution with $-\pi < \theta \leq 0$ can be mapped to a complex solution with $0 < \theta \leq \pi$ and vice-versa. For determining the radius of convergence and the time of validity the whole disk of radius $|\mathbf{\Delta}|$ is searched for poles so it suffices to consider a restricted range of θ to handle all physical initial conditions.

3.5.3 Poles

The condition $\mathbf{b} = 0$ signals the presence of a pole. Inspection of the parametric form shows that this condition can occur only when $\eta = 0$ or $\eta = 2\pi$. The corresponding time

$$\mathbf{t}(\boldsymbol{\Delta},\theta) \quad = \quad \begin{cases} t_0 \pm \left(\frac{\pi}{H_0} \frac{(1+\boldsymbol{\Delta}\cos\theta)}{[-\mathbf{E}(\boldsymbol{\Delta})]^{3/2}} - \mathbf{t}_{\mathbf{age}}(\boldsymbol{\Delta}) \right) & (\eta = 2\pi) \\ t_0 \mp \mathbf{t}_{\mathbf{age}}(\boldsymbol{\Delta}) & (\eta = 0) \end{cases} \tag{3.37}$$

is immediately inferred. Since the independent variable t is real the transcendental equation

$$\Im \mathbf{t}(\boldsymbol{\Delta},\theta) = 0 \tag{3.38}$$

must be solved. It is straightforward to scan the complex $\boldsymbol{\Delta}$ plane and calculate $\mathbf{t}$ to locate solutions. Each solution gives a root of $\mathbf{b} = 0$ and also implies the existence of a pole at the corresponding $\boldsymbol{\Delta}$. Note that relying upon the parametric solutions is a far more efficient method for finding the poles than integrating the complex differential equations numerically. We have verified that both methods produce the same results.

In practice, we fix θ, scan a large area of the complex $\boldsymbol{\Delta}$ plane, locate all purely real $\mathbf{t}$ and save the $\{\boldsymbol{\Delta}, t\}$ pairs. These are used to create a scatter plot of $|\boldsymbol{\Delta}|$ as a function of time (hereafter the "root plot"). Generally, the location of the poles varies smoothly with t and continuous loci of roots are readily apparent. Finding R_Δ and $T(\Delta)$ follows as indicated in figure 3.4.

3.6 Results from the complex analysis

Root plots were calculated for a range of angles $0 \le \theta \le \pi$. Since the root plots depend upon $|\boldsymbol{\Delta}|$ they are invariant under $\theta \to \theta - \pi$ and this coverage suffices for all possible top-hat models. For the results of the full survey in θ see Appendix A.4. The theoretical radius of convergence $R_\Delta(t)$ and time of validity $T(\Delta)$ follow directly.

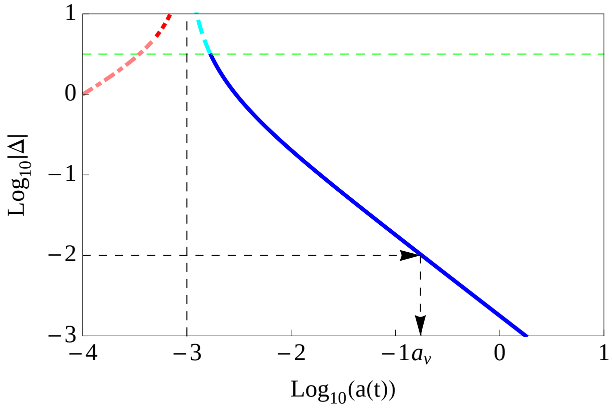

Figure 3.6: R_Δ for $\theta = 2.82$ and $a_0 = 10^{-3}$ (vertical dashed line). To determine the time of validity for LPT expansion with a given Δ, move horizontally to the right of $a = a_0$ following the dashed line with arrow and locate the first colored line with ordinate equal to Δ and then move vertically down to read off the scale factor at the time of validity a_v. The specific case illustrated ($\Delta = 10^{-2}$) matches that of the model with problematic convergence in figure 3.1. The time of validity is correctly predicted. The meaning of the colors is discussed in the text. Coloured version of the figure is available online.

This section analyses the theoretical convergence for specific open and closed models derived from the root plots. These estimates are compared to the time of validity inferred by numerical evaluation of the LPT series. The range of models with limited LPT convergence is characterized. The concept of mirror models is introduced to elucidate a number of interconnections between open and closed convergence. The physical interpretation of roots introduced by the complexification of the equations but lying outside the physical range are discussed. Finally, the special case where the background and the perturbation have the same big bang time is analyzed.

3.6.1 Open models

Figure 3.6 shows $R_\Delta(t)$ for $\theta = 2.82$ and initial scale factor $a_0 = 10^{-3}$. All Δ yield expanding open models for this θ; one choice corresponds to the model whose LPT series appeared in figure 3.1 ($\Delta = 0.01$, $\theta = 2.82$, $a_0 = 10^{-3}$). The x-axis is $\log a$ and is equivalent to a measure of time. The y-axis is $\log|\Delta|$, i.e. the distance from the origin to poles in the complex Δ plane. In principle, future evolution may be limited by real or complex roots. The blue solid line and the red dotted line indicate real and complex roots of $\eta = 2\pi$ respectively. The cyan dashed and pink dot-dashed lines indicate the real and complex roots of $\eta = 0$ respectively. Future evolution is constrained by real roots (blue and cyan) in this example.

The time of validity is the first instance when a singularity appears within the disk of radius Δ in the complex $\boldsymbol{\Delta}$ plane. For the specific case, starting at ordinate $\Delta = 10^{-2}$, one moves horizontally to the right to intersect the blue line and then vertically down to read off the scale factor $a_v = a[T(\Delta)] = 0.179$. The time of validity inferred from the root plot agrees quantitatively with the numerical results in figure 3.1.

Appendix A.4 presents a comprehensive set of results. The time of validity is finite for any open model. As expected, smaller amplitudes imply longer times of validity. The poles do not correspond to collapse singularities reached in the course of normal physical evolution since the open models do not have any real future singularities. A hint of an explanation is already present, however. The green dashed line is $\delta_v = 1$ (or $\Delta = 1/\sin\theta$) at which point the root switches from $\eta = 2\pi$ below to 0 above. Such a switch might occur if varying the initial velocity transposes an expanding closed model into a contracting closed model. But it is expected to occur at $\delta_v = -1$ not 1. The open models are apparently sensitive to past and future singularities in closed models with initial conditions that are transformed in a particular manner. §3.6.3 explores this interpretation in detail.

3.6.2 Closed models

Figure 3.7 presents $R_\Delta(t)$ for models with $\theta = 0.44$ and $a_0 = 10^{-3}$. There are several new features. Over the angular range $\theta_c^- < \theta < \theta_c^+$ the cosmology is closed for small Δ (see shaded region in figure 3.2 near $\Delta = 0$). Conversely, a straight line drawn from $\Delta = 0$ within this angular range must eventually cross the parabola $E = 0$ except for the special case $\theta = 0$. Since the velocity contribution to energy $E \propto \Delta^2$ while the density contribution $\propto -\Delta$ it is clear that eventually $E > 0$ as Δ increases. The critical value, $\Delta_{E=0}$, is a function of θ. Below the brown horizontal dot-dashed line in figure 3.7 the models are closed, above they are open (line labelled $\Delta = \Delta_{E=0}$).

The root plot has, as before, blue solid and red dotted lines denoting the distance to real and complex $\boldsymbol{\Delta}$ poles, respectively, for $\eta = 2\pi$. The cyan dashed line denotes real roots for $\eta = 0$ and does not restrict future evolution.

For small Δ real roots determine the time of validity. These roots correspond exactly to the model's collapse time. In other words, the time of validity is determined by the future singularity. For example, for $\Delta = 0.01$, the root plot predicts that a series expansion should be valid until the collapse at $a = 5.5$ denoted by "$a_v = a_c$" on the x-axis . This prediction is confirmed in the left hand panel of figure 3.8. The root diagram is consistent with the qualitative expectation that small overdensities should have long times of validity because collapse times are long: $\lim_{\Delta \to 0} T(\Delta) \to \infty$.

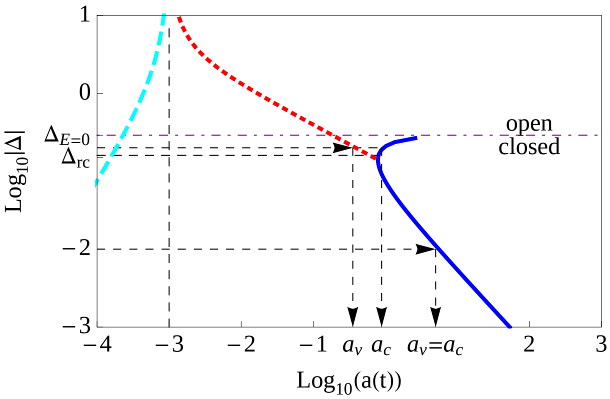

Figure 3.7: R_Δ for $\theta = 0.44$ and $a_0 = 10^{-3}$. The line $\Delta_E = 0$ separates open and closed models. The scale factor at the time of validity is a_v. For closed models the scale factor at time of collapse is a_c. Blue solid line and red small dashed line denote real and complex roots of $\eta = 2\pi$, respectively. The cyan dashed lines denotes the real roots of $\eta = 0$. When the first singularity encountered is real, $a_v = a_c$, the time of validity is the future time of collapse. However, when the singularity is complex the time of validity is less than the actual collapse time. In the range $\Delta_{rc} < \Delta < \Delta_{E=0}$, there are closed models with $a_v < a_c$.

As Δ increases from very small values, i.e. successively larger initial density perturbations, the collapse time decreases. Eventually the velocity perturbation becomes important so that at $\Delta = \Delta_{rc}$ a minimum in the collapse time is reached. For $\Delta_{E=0} > \Delta > \Delta_{rc}$ the collapse time increases while the model remains closed. As $\Delta \to \Delta_{E=0}$ the collapse time becomes infinite and the model becomes critical. All models with $\Delta > \Delta_{E=0}$ are open.

The root diagram shows that for $\Delta > \Delta_{rc}$, the time of validity is determined by complex not real $\boldsymbol{\Delta}$ for $\eta = 2\pi$. Closed models with $\Delta_{rc} < \Delta < \Delta_{E=0}$ have a time of validity less than the model collapse time. For example, for $\Delta = 0.2$, the collapse occurs at $a = 0.94$ but convergence is limited to $a \leq 0.38$. This prediction is verified in the right panel of figure 3.8.

The convergence of LPT expansions for some closed models is limited to

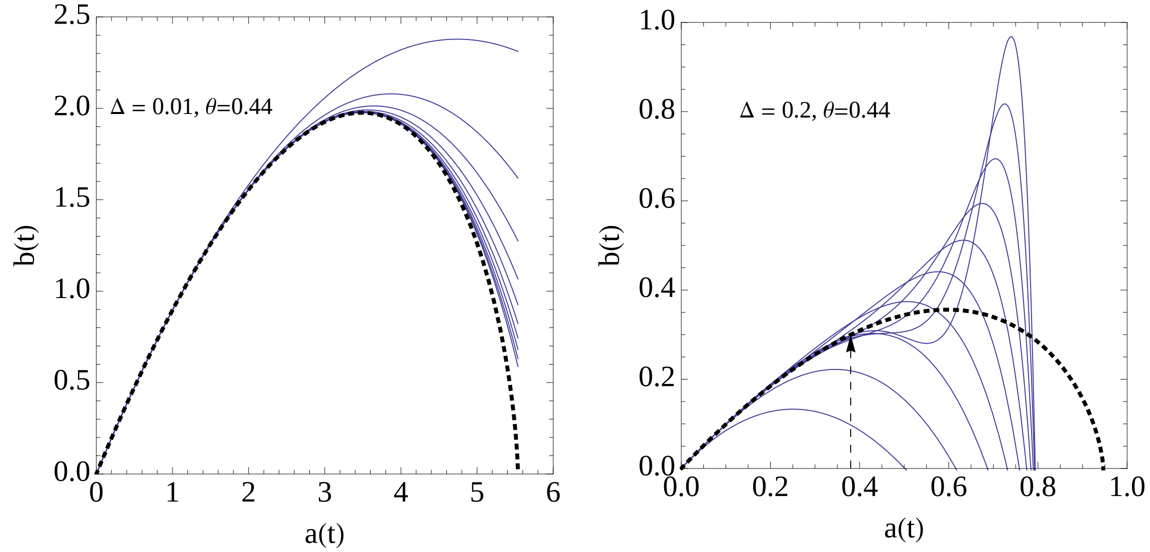

Figure 3.8: The exact solution (black, dashed) and LPT expansions of successively higher order (blue) for two expanding, closed models with $\theta = 0.44$. The left hand panel has $\Delta = 0.01$. LPT converges to the exact solution at all times up to the singularity at $a = 5.5$. The right hand panel has $\Delta = 0.2$. LPT does not converge beyond $a = 0.38$.

times well before the future singularity. This general behavior is observed for $\theta_c^- < \theta < \theta_c^+$ and $\Delta_{rc} < \Delta < \Delta_{E=0}$ where both Δ_{rc} and $\Delta_{E=0}$ are functions of θ. Appendix A.4 provides additional details.

3.6.3 Mirror models, real and complex roots

The parametrization of the perturbation in terms of $\Delta > 0$ and $-\pi < \theta \leq \pi$ and the complexification of $\Delta \to \mathbf{\Delta}$ can give rise to poles anywhere in the complex $\mathbf{\Delta}$ space. When R_Δ is determined by a pole along the real positive axis, a clear interpretation is possible: the future singularity of the real physical model exerts a dominant influence on convergence. LPT expansions for closed models with

$\Delta < \Delta_{rc}$ are limited by the future collapse of the model and are straightforward to interpret.

The meaning of real roots for open models is less clear cut. The roots determining R_Δ at large t are negative real and small in magnitude. Negative Δ lies outside the parameter range for physical perturbations taken to be $\Delta > 0$. Nonetheless the mapping $(\Delta, \theta) \to (-\Delta, \theta \pm \pi)$ preserves (δ, δ_v) and the original equations of motion. The poles of the models with parameters (Δ, θ) and $(\Delta, \theta \pm \pi)$ are negatives of each other. Let us call these "mirror models" of each other.

For infinitesimal Δ if the original model is open then the mirror model is closed. Figure 3.2 shows that the $\Delta_{E=0}$ line has some curvature (in fact, it is a parabola) whereas the mirror mapping is an exact inversion through $\Delta = 0$. Small Δ points are mapped between open and closed; large Δ points may connect open models to other open models.

If the original model is open with limiting pole which is negative real of small magnitude then it corresponds to a future singularity of the closed mirror model. For example, the closed model with parameters $(\Delta = 0.01, \theta = 0.44)$ in the left panel of figure 3.8 and the open model with parameters $(\Delta = 0.01, \theta = 0.44 - \pi)$ shown in the left panel of figure 3.9 are mirrors. The time of the validity of the open model equals the time to collapse of its closed mirror.

The notion of mirror models explains other features of the root diagrams. The time of validity of open models was previously discussed using figure 3.6 $(\theta = 2.82)$. The blue solid line indicated real roots. Such roots are the future singularities of closed mirror models lying in the fourth quadrant along $\theta = 2.82 - \pi = -0.32$. As Δ increases the sequence of mirror models crosses the $\delta_v =$

-1 line (the horizontal dashed line) to become initially contracting cosmologies and, in our labeling, the future singularity switches from $\eta = 2\pi$ to $\eta = 0$. This explains the switch in root label from blue solid to cyan dashed seen in figure 3.6, which occurs at $\delta_v = 1$ in the original model.

The symmetry of the mirroring is not limited to cases when $\mathbf{\Delta}$ is real. It applies for complex $\mathbf{\Delta}$, too. For example, the models in the right panels of figures 3.8 and 3.9 are mirrors of each other. Their time of validity is the same and determined by complex roots which are negatives of each other. These singularities are non-physical and have no interpretation in terms of the collapse of any model yet they limit the LPT convergence in the same way.

Figure 3.10 shows the areas of phase space where complex roots determine the time of validity in light red. The area within the parabola (light blue) contains closed models. Most of the light blue region has a time of validity determined by real roots, i.e. the time to the future singularity. The area with both light blue and red shading encompasses closed models with the unexpected feature that the time of validity is less than the time to collapse.

The area outside the parabola contains open models. The time of validity of the unshaded region is determined by real roots. The original observation of LPT's non-convergence for an underdensity (Sahni & Shandarin [70]) is an example that falls in this region. For small amplitude perturbations the time of validity is simply related by mirror symmetry to the occurrence of future singularities of closed models. The right hand plot in figure 3.9 is an example of an open model with time of validity controlled by complex roots (red shading outside the parabola).

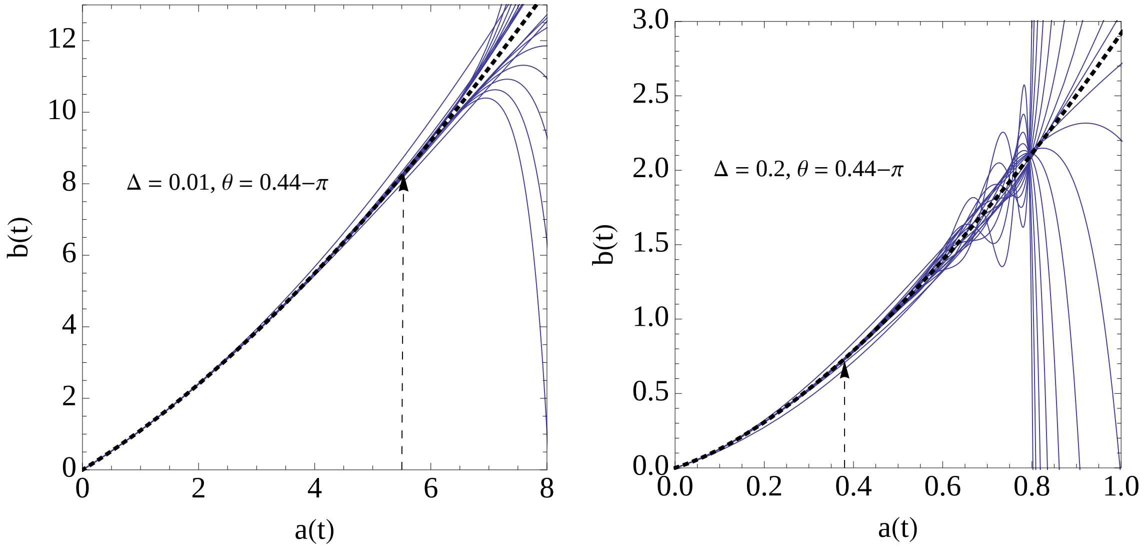

Figure 3.9: Mirror models of the closed models of figure 3.8. Each graph shows the exact solution (black, dashed) and the LPT expansion to successively higher orders (blue) of one mirror model. The original model and the mirror have the same time of validity for the LPT expansion.

Finally, some open models (especially those with large Δ) have mirrors that are open models. Figure 3.11 shows mirror models ($\Delta = 2$, $\theta = 17\pi/36$) and ($\Delta = 2$, $\theta = 17\pi/36 - \pi$). These are initially expanding and contracting solutions respectively. The root plot in figure 3.12 predicts that the series is valid until $a_v = 0.0016$. The real root with $\eta = 0$ (cyan line) sets the time of validity and corresponds to the bang time (the future singularity) of the initially contracting model.

In all cases, the analysis correctly predicts the convergence of the LPT series.

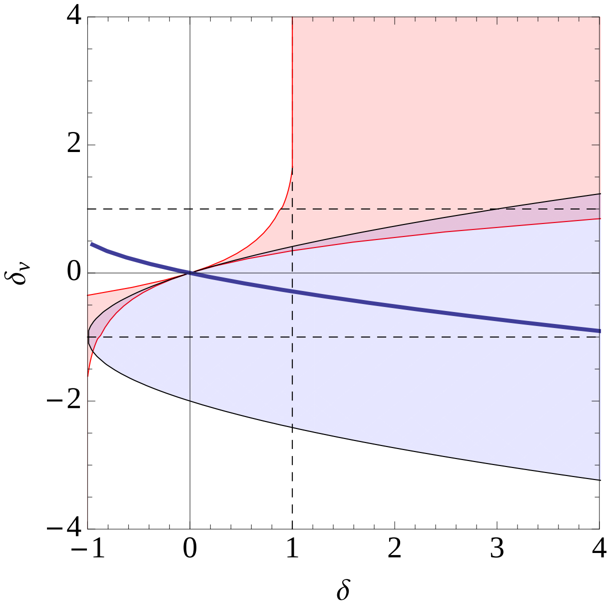

Figure 3.10: The red shaded region denotes part of phase space where complex roots play a role. The solid blue line represents the initial conditions which correspond to the background and perturbation having the same big bang time. The black solid parabola separates the closed and open models. Coloured version online.

3.6.4 Zeldovich and equal bang time models

The large expanse of phase space shaded light red in figure 3.10 suggests that complex roots should play a ubiquitous role in LPT applications but the situation is somewhat more subtle. For good physical reasons purely gravitational cosmological calculations often start with expanding, small amplitude, growing modes at a finite time after the big bang. The absence of decaying modes implies that the linearized perturbations decrease in the past [1]. A non-linear version of this condition is that the perturbation amplitude

---

[1] Our analysis is restricted to the case of initially expanding models, i.e. near $\Delta = 0$. For initially contracting closed models, similar physical arguments motivate a consideration of the behavior near the initial singularity (not the future bang time). For initially contracting open models the epoch of interest is $t \to -\infty$. These models have large Δ and are not described by the linear limit discussed in the text.

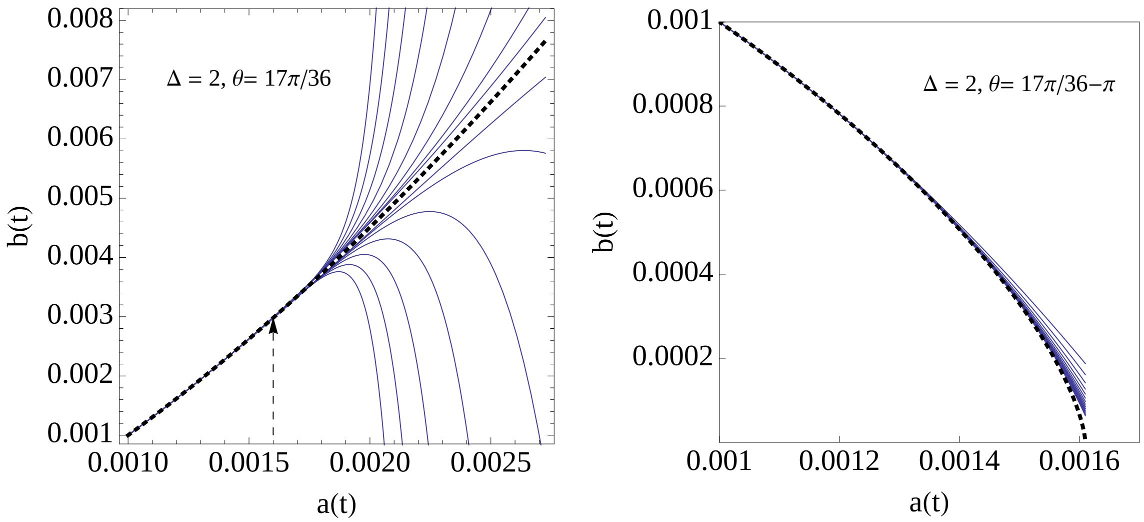

Figure 3.11: Two open models which are mirrors of each other. Each plot shows the exact solution (black, dashed) and the LPT series expansion to successively higher orders (blue). The left panel is an initially expanding, open model whose convergence is limited to scale factors less than $a_v = 0.0016$ (arrow). The right panel shows the initially contracting mirror model whose bang time at $a_v = 0.0016$ is responsible for the limitation.

is exactly zero at $t = 0$. The same condition can be formulated as “the background and the perturbation have the same big bang time” or “the ages of the perturbation and the background are identical.” The condition is

$$\frac{1}{H_0}\int_{y=0}^{y=1} \frac{dy}{\left[(1+\Delta\cos\theta)y^{-1}+E(\Delta,\theta)\right]^{1/2}} = \frac{2}{3H_0}. \tag{3.39}$$

This is a nonlinear relationship between the two initial parameters Δ and θ which is shown by a thick blue line on the phase space diagram in figure 3.10. We have adopted the name “Zeldovich” initial conditions for the top-hat models that satisfy the equal bang time relation. There are a variety of definitions for Zeldovich initial conditions given in the literature. Generally, these agree at linear order. This one has the virtue that it is simple and easy to interpret. Note

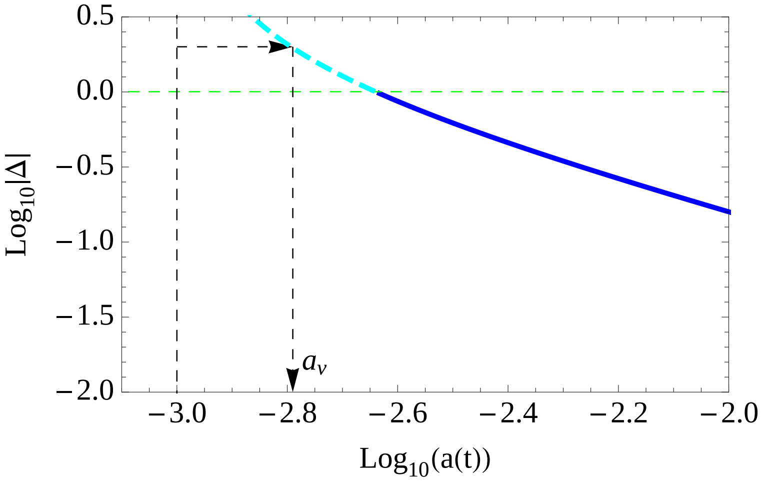

Figure 3.12: R_Δ for $\theta = 17\pi/36$ and $a_0 = 10^{-3}$. The blue solid and cyan dashed lines denoted real roots with $\eta = 2\pi$ and $\eta = 0$ respectively. For $\Delta = 2$, the time of validity is set by the root with $\eta = 0$, which is the bang time of the mirror model with $\theta = 17\pi/36 - \pi$. See figure 3.11 for the evolution of both models.

that the blue curve does not intersect the region of phase space where complex roots occur except, possibly, near $\mathbf{\Delta} = 0$.

In the limit of small Δ eq. (3.39) becomes

$$\Delta(3\sin\theta - \cos\theta) = 0. \tag{3.40}$$

The solutions are $\theta = \theta_{Z\pm}$ where $\theta_{Z+} = 2.82$ and $\theta_{Z-} = \pi - \theta_{Z+} = -0.32$. The second quadrant solution θ_{Z+} corresponds to open models while its mirror in the fourth quadrant θ_{Z-} to closed models. Only when $\Delta \to 0$ can complex roots approach the loci of Zeldovich initial conditions but they intersect only in the degenerate limit.

In the next section, we will show that points starting close to the Zeldovich curve continue to stay near it as they move through phase space. Such models have real, not complex, roots. This implies that closed systems along the curve always have a convergent series solution. Hitherto, LPT convergence has been studied only for initial conditions close to the Zeldovich curve. This is why problems have been noted only in the case of voids. The existence of the complex roots is a new finding. All of the above is based on the spherical top-hat model which has a uniform density.

As emphasized above, there are good physical motivations for adopting Zeldovich-type initial conditions. The fact that cosmological initial conditions must also be inhomogeneous (i.e. Gaussian random fluctuations) is not captured by the top-hat model. One can imagine two extreme limiting cases for how the simple picture of top-hat evolution is modified. If each point in space evolves independently as a spherical perturbation then at any given time one expects to find a distribution of points along the Zeldovich curve. As time progresses this distribution moves such that the underdense points cluster around the attracting point $(-1, 0.5)$ and overdense points move towards collapse. The distribution of initial density and velocity perturbations yields a cloud of points in phase space but complex roots never play a role because nothing displaces individual points from the Zeldovich curve. Each moves at its own pace but stays near the curve. Alternatively, it is well known that tidal forces couple the collapse of nearby points. These interactions amplify the initial inhomogeneities leading to the formation of pancakes and filaments. As time progresses motions transverse to the Zeldovich curve will grow. If these deviations are sufficient they may push some points into areas with complex roots. In a subsequent paper, we will explore these issues for general inhomogenous initial conditions.

3.7 LPT re-expansion

To overcome the constraints above, an iterative stepping scheme that respects the time of validity is developed for LPT. The initial parameters at the first step determine the solution for some finite step size. The output at the end of the first step determines the input parameter values for the next step and so on.

3.7.1 The Algorithm

Choose the background (a_0, H_0, $\Omega_0 = 1$, Y_0) and the perturbation ($b_0 = a_0$, H_{p0}, Ω_{p0}, X_0) at initial time t_0. The perturbed model is fully characterized by H_{p0} and Ω_{p0} or by $\delta_0 = \rho_{p0}/\rho_0 - 1$ and $\delta_{v,0} = H_{p0}/H_0 - 1$ or by Δ_0 and θ_0. Extra subscripts have been added to label steps.

LPT converges for times $t < T(\Delta_0, \theta_0)$. Use LPT to move forward to time t_* satisfying $t_0 < t_* < T(\Delta_0, \theta_0)$. At t_*, the background and perturbed scale factors and time derivatives are a_*, b_*, $\dot{a}_*$, and $\dot{b}_*$. The fractional density and velocity perturbations with respect to the background are

$$\delta_* = (1 + \delta_0)\left(\frac{a_*}{b_*}\right)^3 - 1 \tag{3.41}$$

$$\delta_{v,*} = \frac{\dot{b}_*/b_*}{\dot{a}_*/a_*} - 1. \tag{3.42}$$

Re-expand the perturbation around the background model as follows. First, let the time and Lagrangian coordinate for the background (inner edge of the unperturbed sphere) be continuous: $t_1 = t_*$ and $Y_1 = Y_0$. These imply $a_1 = a_*$ and $\dot{a}_1 = \dot{a}_*$, i.e. the scale factor and Hubble constant for the background are continuous.

At the beginning of the first step we assumed $a_0 = b_0$. This is no longer true at the end of the first step. Define a new Lagrangian coordinate $X_1 = X_0 b_* / a_*$, new scale factor $b_1 = a_*$, and new scale factor derivative $\dot{b}_1 = \dot{b}_* a_* / b_*$. These definitions leave the physical edge of the sphere and its velocity unaltered

$$r_{physical,*} = b_* X_0 = b_1 X_1 \tag{3.43}$$

$$\dot{r}_{physical,*} = \dot{b}_* X_0 = \dot{b}_1 X_1. \tag{3.44}$$

The re-definitions relabel the fluid elements with a new set of Lagrangian coordinates and re-scale the scale factor. The perturbation parameters are unchanged $\delta_1 = \delta_*$ and $\delta_{v,1} = \delta_{v,*}$ because physical quantities are unmodified. Consequently, $\Delta_1 = \Delta_*$ and $\theta_1 = \theta_*$.

3.7.2 Flow dynamics in the phase space

To examine how Lagrangian re-expansion works consider how the Lagrangian parameters Δ and θ would vary if they were evaluated at successive times over the course of a specific cosmological history. Let $\delta(t)$ and $\delta_v(t)$ be defined via eq. (3.3) and apply the second-order equations of motion eqs. (3.9) and (3.10) to derive the coupled first-order system

$$\frac{d\delta}{dt} = -\frac{2}{t}\delta_v(1+\delta) \tag{3.45}$$

$$\frac{d\delta_v}{dt} = \frac{1}{3t}\{(1+\delta_v)(1-2\delta_v) - (1+\delta)\} \tag{3.46}$$

where all occurrences of δ and δ_v are functions of time. From $\delta(t)$ and $\delta_v(t)$ one infers the parameters, $\Delta(t)$ and $\theta(t)$. These have the following simple interpretation: a Lagrangian treatment starting at time t' has $\Delta = \Delta(t')$ and $\theta = \theta(t')$ in the LPT series.

Since the system is autonomous it reduces to a simple flow in phase space. The flow has three fixed points at $(\delta, \delta_v) = (0, 0)$, the unperturbed, background model, $(-1, -1)$, a vacuum static model, and $(-1, 0.5)$, a vacuum expanding model. Linearizing around $(0, 0)$ shows it is a saddle fixed point. The tangent to the $E = 0$ curve at the origin is the attracting direction and the tangent to the equal big bang curve is the repelling direction. The fixed point at $(-1, 0.5)$ is a degenerate attracting node and that at $(-1, -1)$ is an unstable node. The flow vectors are plotted in the left panel of figure 3.13. The blue shaded region indicates closed models and red shaded region indicates models where complex roots limit the time of validity for LPT.

Note that the flow lines smoothly cover the whole phase space. The interpretation is that the continuous relabeling of Lagrangian coordinates and re-scaling of the scale factor has the potential to overcome the convergence limitations discussed thus far. Otherwise one might have seen ill-defined or incomplete flows or flows that were confined to a given region.

Asymptotic limits of open and closed models

The right panel of figure 3.13 zooms in on the area near the origin. Initial points that correspond to open models starting near the origin approach the Zeldovich curve and asymptotically converge to the strong attractor at $(\delta, \delta_v) = (-1, 0.5)$.

Closed models collapse and the density $\delta \to \infty$. In the asymptotic limit, the solution to (3.46) is given by $\delta \sim \delta_v^2 + K$ with integration constant K. From figure 3.13, the flow lines of closed models that start in the vicinity of the origin trace a parabolic path that is parallel and essentially equivalent to the Zeldovich curve.

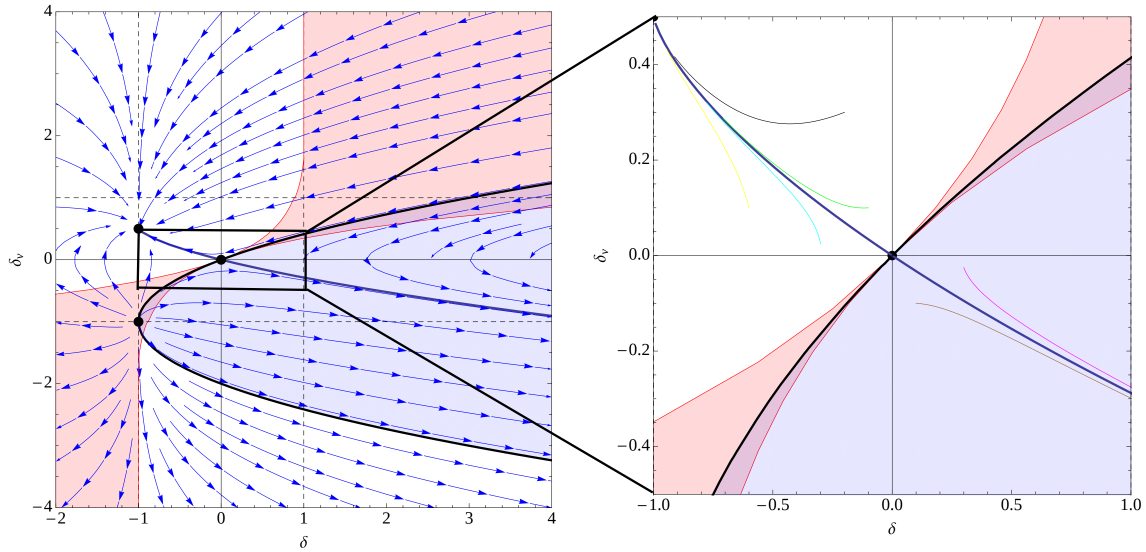

Figure 3.13: The left panel shows streamlines of the flow described by eq. (3.46). The color coding of the plot is same as figure 3.10. The right panel zooms in on the area near the origin which is where all models are located at sufficiently early times. At late times, open models move away from the origin towards the attracting fixed point at $(\delta, \delta_v) = (-1, 0.5)$. The attraction to the Zeldovich solution is shown for a set of initial conditions (yellow, cyan, green and black lines) that begin near but not on the critical trajectory. Closed models move out to infinity along the fixed big bang time curve. Coloured version online.

The flow shows where re-expansion is needed. Closed model flow lines that start near the origin never pass through the red shaded region where complex roots play a role; the time of validity equals the time to collapse and no re-expansion is needed. However, closed models that originate in the red region must be re-expanded. The flow suggests that they eventually move into the blue region. So even though a closed model may initially have an LPT series with limited convergence, re-expansion makes it possible to move into the part of phase space where a single step suffices to reach collapse.

3.7.3 Finite steps and feasibility

This section and the next examine the feasibility of extending a solution from recombination to today. The results will be applied to fully inhomogeneous evolution in future paper.

Let the asymptotic time of validity for an open model be expressed in dimensionless form $\chi = \lim_{t\to\infty} H(t)T(\Delta(t), \theta(t))$. Here, $\Delta \to \sqrt{5/4}$ and $\theta \to \tan^{-1}(-1/2) = 2.677$ and $T(\Delta, \theta)$ is determined by the future time to collapse of the closed mirror model. The result is $\chi = 2.62$ (numerical results in Appendix A.4), the time of validity is proportional to the characteristic age of the background and individual steps grow larger and larger.

An example shows that the basic effect can be seen even before the asymptotic regime is achieved. Figure 3.14 sketches the first two steps where the assumed model parameters at the first step are $(\Delta_0, \theta_0) = (0.01, 2.82)$. The scale factor at the time of validity is $a = 0.179$. A step with half the allowed increment in time is taken and the system is reinitialized. The re-initialization implies $(\Delta_1, \theta_1) = (0.91, 2.68)$ or $(\delta_1, \delta_{v,1}) = (-0.82, 0.4)$. Afterwards the new time of validity is larger in this example.

The feasibility of the re-expansion scheme can be examined by evaluating the ratio of the time of validity before (T) and after (T') a step

$$\alpha = \frac{T'}{T}. \tag{3.47}$$

Figure 3.15 shows α evaluated along the continuous flow as a function of scale factor for three different starting initial conditions. Since $\alpha > 3$ at all times, starting at initial time t_i the time after N steps is roughly $t \sim \alpha^N t_i > 3^N t_i$.

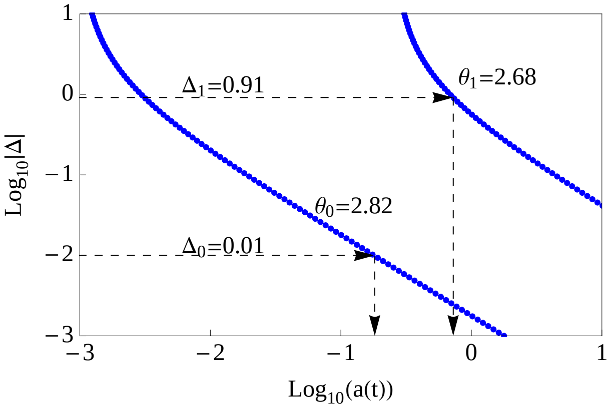

Figure 3.14: Extending the time of validity of LPT. The first step has $\Delta_0 = 10^{-2}$ and $\theta = 2.82$ and implies scale factor at the time of validity $a_v = 0.179$. Incrementing by half the allowed step gives initial conditions for the second step $(\Delta_1, \theta_1) = (0.91, 2.68)$. Note that the new time of validity has increased.

Consider, for example, the number of steps needed to extend an open solution from recombination to today. Let t_f (t_i) be the final (initial) time of interest where $t_f/t_i \sim a_f/a_i \sim 10^{4.5}$. Estimating $\alpha = 3$ implies $N \sim \log_3 10^{4.5} \sim 10$ steps are needed. This numerical result for N is an overestimate and one can do better. It is important to recall that it based on an arbitrarily high order expansion which achieves an exact solution. If one is limited to calculations of finite Lagrangian order and imposes a maximum numerical error at the end of the calculation then more than N steps may be required. At least N steps are needed for series convergence and more than N steps may be needed for error control.

One can extend any open model to an arbitrary future time while respecting the time of validity of the LPT series. The number of steps is governed by a geometric progression.

One can also extend any closed model to the future singularity while

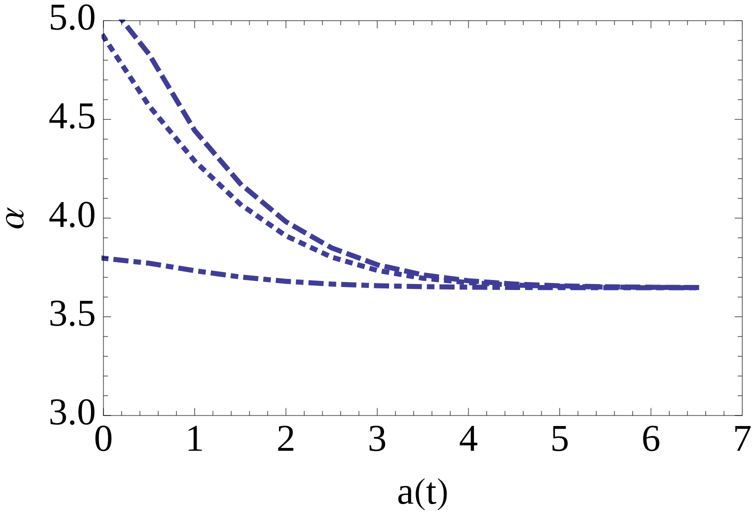

Figure 3.15: The ratio of successive times of validity (α) vs. $a(t)$. The dashed, dot-dashed and dotted lines indicate three initial starting points $(0.5, 0.5), (0, 1), (-0.2, 0.2)$ respectively. The ratio converges to about 3.6 and the time of validity increases geometrically with N.

respecting the time of validity of the LPT series. Only a single step is needed for a closed model when the root is real (blue shaded region of figure 3.13). When it is complex (the region shaded both blue and red) the model flows first toward the node at $(0, 0)$ (Δ decreases) and ultimately reaches the region of real roots. Multiple steps will generally be necessary to escape the region of complex roots. An approximate fit (eq. (A.39)) shows that $\chi \sim T(\Delta, \theta)H(t) \propto \Delta^{\beta}$ for small Δ where $\beta < -2.5$. Both χ and the time of validity increase as the node is approached. Time advances at least as quickly as a geometric progression and this is analogous to the manner in which the open model steps towards its limit point. However, unlike the open case, once the trajectory crosses into the blue region (assuming it does not lie exactly on the unstable attracting trajectory) a single final step is needed. The specific number of steps will depend upon the starting initial conditions but will be small because of the property of geometric progression.

3.7.4 Demonstrative examples

LPT re-expansion can solve the problematic convergence in previously analyzed open and closed models.

Open models have asymptotic values of Δ and θ and simple evolution. The first section below includes numerical results that provide a practical demonstration of the success of LPT re-expansion in this case. Convergence as Lagrangian order increases and/or time step size decreases is observed qualitatively.

Closed models have a somewhat more complex behavior (before and after turnaround). The second section provides both a qualitative and quantitative discussion of convergence. The scaling of the leading order error and the time step control which are derived are of general applicability.

Open model

Figure 3.16 investigates the effect of time step and order on the evolution of the open model introduced in figure 3.1 ($\Delta = 0.01$, $\theta = 2.82$, $a_0 = 10^{-3}$). The series convergence breaks down at $a = 0.179$. The left panel shows an attempt to take a single step to $a = 1$ using successively higher LPT series orders. As expected, higher order terms do not improve the accuracy of the description because the time of validity is violated. The middle panel employs three steps to reach $a = 1$, each respecting the time of validity. Now the LPT series with higher order improves the accuracy just as one desires. The right panel employs six steps to reach $a = 1$, each respecting the time of validity. Again, higher order improves the description. Note that more frequent re-expansion, i.e. smaller

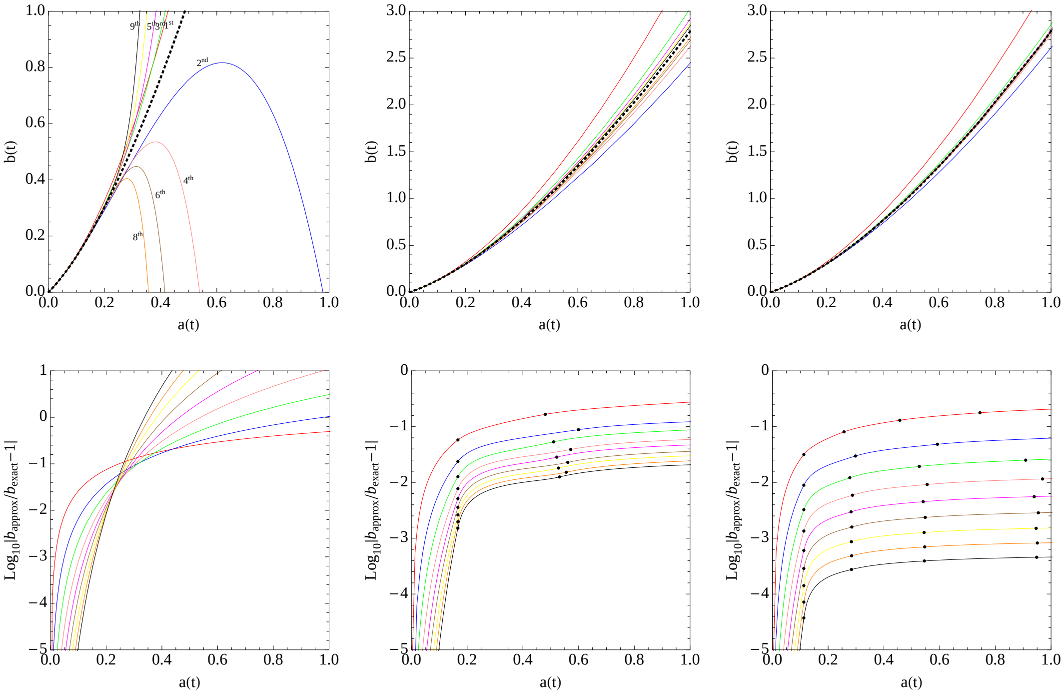

Figure 3.16: LPT re-expansion of an open model with $\Delta_0 = 0.01$ and $\theta_0 = 2.82$. The top three figures show the scale factor for the same initial conditions calculated with one step (left), three steps (middle) and five steps (right). The black dots indicate the position of the time steps. In the middle and right panels, the solution was advanced 9/10 and 1/2 the allowed time of validity, respectively. The bottom figures show the errors for all LPT approximations to $b(t)$ including the unphysical negative ones. The order of the LPT expansion are color-coded according the top left figure. The single step expansion does not respect the time of validity whereas both the three and six step examples do. The original expansion does not converge over the full time range whereas the re-expansions do. Coloured version online.

steps in time, improve the errors at fixed LPT order.

Closed model

Figure 3.17 investigates the closed model introduced in figure 3.8 ($\Delta = 0.2, \theta = 0.44, a_0 = 10^{-3}$). The time of validity is determined by a complex root. The first panel shows that the series begins to diverge at $a = 0.38$ well before the collapse singularity is reached at $a = 0.94$.

A single time step less than the time of validity is guaranteed to converge as the order of the Lagrangian expansion increases. LPT re-expansion utilizes a set of such time steps each of which is likewise guaranteed to converge. However, since a calculation of infinite order is never achieved in practice, it is worth characterizing how convergence depends upon two calculational choices one has at hand, the time step and the order of the Lagrangian expansion.

A single small step beginning at $t = t_0$ and ending at t_f has leading order error for the m-th order Lagrangian approximation [2] $\propto (t_f/t_0 - 1)^{m+2}\Delta^{m+1}$, where Δ is the value at the initial time. If the same small interval is covered in N smaller steps, the error after N steps scales as $N^{-m}(t_f/t_0 - 1)^{m+2}\Delta^{m+1}$ (see Appendix A.5 for details). If the step size increases in a geometric sequence such that $\delta t/t$ is a constant for each intermediate step, then $t_f = t_0(1 + \delta t/t)^N$ and the error after N steps scales as $N(t_f/t_0 - 1)(\delta t/t)^{m+1}\Delta^{m+1}$. This leads to the interpretation that the error per intermediate step scales as $(\delta t/t)^{m+1}\Delta^{m+1}$. Define $\epsilon = (\delta t/t)\Delta$. The leading order error scales as ϵ^{m+1} which is numerically small if $\epsilon < 1$. The sum of all the missing higher order terms is finite if $\delta t < T$, i.e respects the time of validity.

---

[2] Typically, the numerical coefficient is of order unity and varies with m as well as the particular value of θ. For the purposes of a discussion of the scaling of the error term, we assume the numerical coefficients to be constant as m and θ vary.

In a practical application, the initial and final times are not close. A reasonable time step criterion is to choose $\epsilon < 1$ fixed throughout the evolution and to infer δt for a given Δ. Other choices are possible but δt must always be less than the time of validity. If ϵ is held fixed throughout the evolution, then the net error after N steps for the m-th order approximation $\propto \epsilon^{m+1} N$.

The number of steps required to go from the initial to the final time can be estimated. As a special case assume that Δ is constant. The time step criterion implies that the number of steps to move from the initial time $t = t_0$ to the final time t_f for given ϵ is $N = \log(t_f/t_0)/\log(1 + (\epsilon/\Delta))$. For limited total intervals ($t_f - t_0 << t_0$) and small steps ($\epsilon/\Delta << 1$) the exact answer reduces to $N \sim (t_f - t_0)\Delta/\epsilon = (t_f - t_0)/\delta t$. Here $\delta t = \epsilon t \Delta$ does not grow appreciably over the interval so the estimate for N is a maximum. In this limit, the net error $\propto \epsilon^m \Delta$. The leading order error for the m-th order Lagrangian scheme decreases at least as quickly as ϵ^m.

In more general situations the value of Δ varies. Once the closed model turns around Δ increases without bound. For fixed ϵ the step size δt decreases monotonically to zero as $t \rightarrow t_{coll}$ where t_{coll} is the time of the future singularity. At any order it would take infinitely many steps to follow the solution up until collapse. Consider the problem of tracking the solution up to a large, finite value of $\Delta = \Delta_f$. This moment corresponds to a fixed time $t_f \lesssim t_{coll}$ in the exact solution. The number of steps $N < N_{max} \sim t_f/\delta t_f$ where δt_f is the step size for the system near Δ_f; $\delta t_f \propto \epsilon/\Delta_f$. The leading order error after N steps at the m-th Lagrangian order $\propto \epsilon^{m+1} N < \epsilon^{m+1} N_{max} \sim \epsilon^m \Delta_f$. This method of step control forces the leading order error at fixed time $t_f < t_{coll}$ to decrease as the Lagrangian order m increases and/or the control parameter ϵ decreases.

The second and third panels in figure 3.17 show the runs with $\epsilon = 0.5$ and $\epsilon = 0.2$ respectively. The Lagrangian orders are color-coded; dots show time steps determined by the above criterion. At each order the solution was terminated when the numerically determined $\Delta > 100$ so as to avoid the infinite step regime. This required 32 steps for the $\epsilon = 0.5$ run and 77 steps for the $\epsilon = 0.2$ run. As the red solid lines illustrates, the first order solution turns around before all other solutions. This explains why its step size begins to shrink near the midpoint of the graph. By contrast, all the step sizes for higher order solutions are very similar up to that point.

The numerical errors may be analyzed from two points of view.

1. A comparison of different coloured lines (different Lagrangian orders) in a single panel shows that error decreases as m increases. This is true in a quantitative as well as qualitative sense. For example, in the second panel at $a = 0.64$ a plot of the log of the absolute error is approximately linear in m, as expected.
2. A comparison of the same coloured lines in the middle and right panels shows that smaller ϵ implies better accuracy. Again, this is true in a quantitative as well as qualitative sense. For example, the observed ratio of errors at $a = 0.64$ for the 9-th order calculations is 5×10^{-4}. To evolve up to this time with $\epsilon = 0.5$ (middle panel) takes 10 steps; with $\epsilon = 0.2$ (right panel) it takes 22 steps. The expected ratio of errors is $(0.2/0.5)^{9+1}(22/10) \sim 2 \times 10^{-4}$, the same order of magnitude as the observed ratio.

These comparisons lead to the important conclusion that the leading order error for LPT re-expansion varies with Lagrangian order and time step as theoretically expected.

It is clear that considerable benefit accrues not only from implementing higher order Lagrangian schemes but also by limiting time step size (which must always be less than the time of validity). For simple examples like the top-hat it is feasible to work to very high Lagrangian order but this is not likely to be true in the context of more complicated, inhomogeneous problems. On the other hand, marching forward by many small time steps using LPT re-expansion is generally feasible. In the example above the initial perturbation is $\Delta = 0.2$ whereas a practical calculation starting at recombination would start with $\Delta \sim 10^{-5}$. For the same ϵ the practical application requires more steps for the phase before turnaround but the net increase is only a modest logarithmic factor. In fact, most of the steps in the example were taken after turnaround and the total number varies with the depth of the collapse. This will continue to be true for the practical calculation. The choice of step size and order for such applications will be the subject of a forthcoming paper.

3.8 Conclusion

We have investigated the time of validity of Lagrangian perturbation theory for spherical top-hat cosmologies with general initial conditions. Using techniques from complex analysis we showed that the time of validity is always limited for open models. We also discovered a class of closed models whose time of validity is less than their time to collapse. We introduced the concept of the mirror model and derived a symmetry principle for the time of validity of mirror models. For

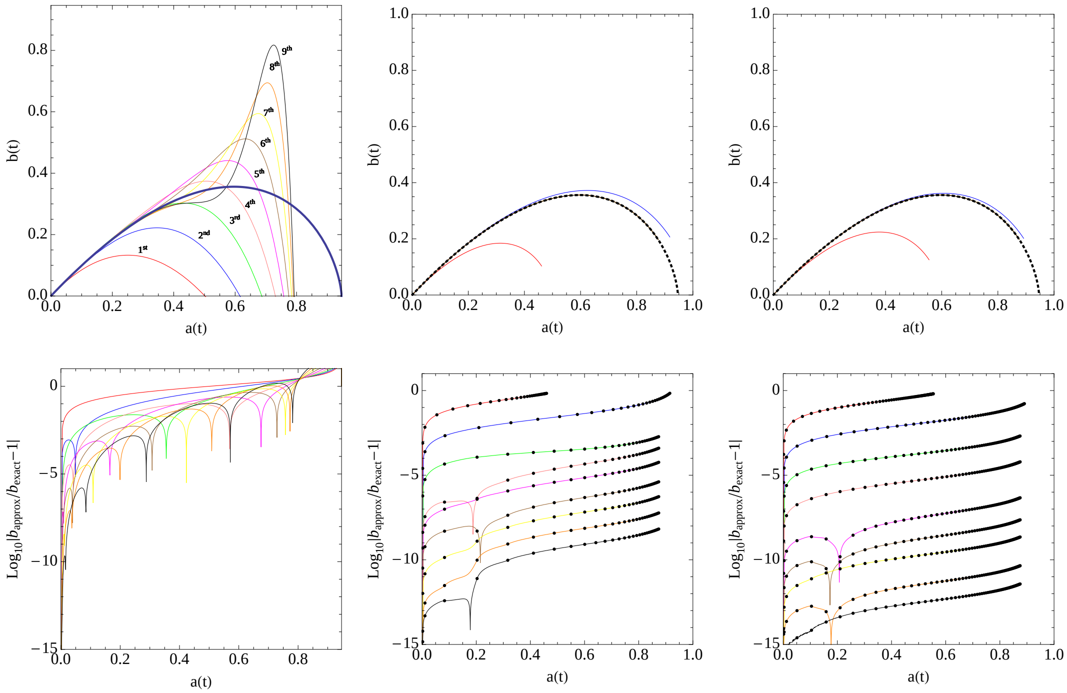

Figure 3.17: LPT re-expansion of a closed solution with $\Delta = 0.2$, $\theta = 0.44$. The top three figure show the scale factor calculated with a single step (left) and multiple steps with $\epsilon = 0.5$ (middle) and $\epsilon = 0.2$ (right) (refer to text for definition of ϵ). The bottom figures show the errors for all LPT approximations to $b(t)$ including the unphysical negative ones. The order of the expansion is color-coded as in the top left figure. The single step expansion does not respect the time of validity whereas both the other cases do. The black dots indicate the position of the time steps. The original expansion does not converge over the full time range whereas the re-expansions do. Coloured version online.

small initial perturbations the time of validity of LPT series expansion of an open model corresponds to the collapse time of a closed mirror model.

A qualitative analogy is useful. A single LPT series expansion is similar to a single step in a finite difference approximation for advancing a hyperbolic partial differential equation like the wave equation. The time of validity of the LPT expansion is analogous to the Courant condition which guarantees stability.

In LPT the constraint is an acceleration-related time-scale; in the wave equation it is a sound-crossing time-scale.

We developed the method of LPT re-expansion which overcomes the limitations intrinsic to a single expansion. We demonstrated how to iteratively re-expand the solution so as to link convergent series expressions that extend from initial to final times. The time of validity of the expansions set the minimum number of re-expansion steps (~ 10) necessary for cosmological simulations starting at recombination and proceeding to the present epoch. Finite as opposed to infinite order Lagrangian expansions required extra steps to achieve given error bounds. We characterized how the leading order numerical error for a solution generated by LPT re-expansion varied with the choice of Lagrangian order and of time step size. We provided a recipe for time step control for LPT re-expansion based on these results.

Our long-term goal and motivation for this study is to develop a numerical implementation of LPT re-expansion for fully inhomogeneous cosmological simulation. Top-hats with Zeldovich initial conditions have special properties with respect to LPT convergence. We found that all underdense models must be treated by re-expansion while none of the overdense ones need be. However, during the course of an inhomogeneous simulation the density and irrotational velocity perturbations (with respect to a homogeneous background cosmology) at an arbitrary point will generally not fall on the top-hat's Zeldovich curve. Hence, the convergence of LPT in inhomogeneous applications must be guided by the analysis of more general models. Top-hats with arbitrary initial conditions are the simplest possibility and constitute the main focus in this paper. The limitations on LPT convergence which we have elucidated in this generic case are considerably more complicated than in the top-hat with Zeldovich initial conditions. Our plan is to use the generic time of validity criterion to determine the time-stepping for inhomogeneous evolution. This should allow us to develop high-precision simulations with well-defined control of errors. The practical impact of a refined treatment of LPT convergence is not yet clear.

The convergence issues we have dealt with should not be confused with the breakdown when orbit crossing takes place and the Jacobian of the transformation from Lagrangian to physical coordinates becomes singular. At that time the flow becomes multi-streamed and much of the simplicity and advantage of the Lagrangian approach vanishes. The aim of the current work is to make sure it is possible to reach the epoch of multi-streamed flow but offers nothing new on how to proceed beyond it. In fact, it may be necessary to include an effective pressure term in the equations to account for the velocity dispersion induced by orbit crossing (Adler & Buchert [1]; Buchert & *et al* [19]) or to adopt alternative approximations for the basic dynamics (such as the adhesion approximation; see Sahni & Coles [69] for a review and references therein) to make progress.

CHAPTER 4

MODELING MILDLY NON-LINEAR EVOLUTION USING LPT RE-EXPANSIONS

The material presented in this chapter will be submitted to MNRAS.

4.1 Abstract

We develop a numerical method of solution of the hierarchy of equations generated by Lagrangian Perturbation Theory for the problem of structure formation in cosmology. The general formalism due to Buchert and Ehlers is coupled to the idea of Lagrangian re-expansion developed in a recent paper by the authors. The algorithm evolves arbitrary inhomogeneous initial conditions in a periodic universe up until the formation of the first caustic. The Lagrangian order n, number of time steps N_t and grid size N_s are the three parameters that control the error. Convergence with respect to each is tested. Time stepping is based on the detailed convergence analysis of the same Lagrangian hierarchy as developed for the top-hat model. The results show that the method faithfully models non-linear evolution of inhomogeneous initial conditions including random Gaussian fields. The general technique will facilitate both numerical and analytic investigations of linear and quasi-linear evolution in cosmology.

4.2 Introduction

In the recent past, the growth history of large scale structure has emerged as a very powerful tool to constrain fundamental constituents and properties of the universe. While linear perturbation theory provides analytic answers on large scales, the treatment breaks down once non-linearities grow large, occurring first on small scales for a typical initial perturbation spectrum like that of cold dark matter. These scales are typically modeled by numerical N-body simulations (Bertschinger [11], Klypin [41]). Such simulations have their own shortcomings. Firstly, they are time consuming; volumes as big as the one used for the Millennium simulation [75] can take months to run. It is common practice to use fits to the power spectrum instead of running large simulations (e.g. Smith et al [74], Peacock and Dodds [62], Ma [49], Ma *et al* [50]). But these fits are usually done over a restricted range of parameter space. Secondly, simulations usually cannot be started at very early times $z >> 50$ since shot noise can contaminate the initial conditions because the perturbations are small. In the current era of precision cosmology and dark energy phenomenology, these drawbacks may prove to be significant. Therefore analytic descriptions in the non-linear regime are necessary not only to explain the physics underlying simulations but also to serve as a bridge between linear theory and N-body codes.

The analytic description of a fluid is mainly carried out in either the Eulerian or Lagrangian frame. In the Eulerian framework, the density and velocity are the two main dependent variables and they are expressed as functions of the grid coordinates $\mathbf{x}$ and time t. In a perturbative treatment the dependent variables are expanded in powers of a small parameter, usually taken to be the magnitude of the initial density and/or velocity field. On the other hand, in the Lagrangian framework, the physical position is the dependent variable and it is expressed as a function of the initial particle labels $\mathbf{X}$ and time t. Once the position is known, the Eulerian density and velocity are then reconstructed using exact non-perturbative definitions. Thus, even at first order in perturbation theory, the Lagrangian framework yields a non-linear density field. Since the density is estimated in a formal sense via the mass conservation equation, a numerical implementation of the Lagrangian scheme does not suffer from N-body like shot noise effects. The scheme efficiently handles small amplitude, smooth initial conditions which may be specified at any post-equipartition redshift and as long as the underlying Newtonian treatment is valid.

It must be mentioned that numerical simulations are essentially Lagrangian calculations because they too track particle positions. However, they differ from the analytic framework because the particle nature implies a discrete representation of a smooth density field. In the analytic framework, the prescription to compute the density breaks down beyond shell crossing unless other approximations (such as the adhesion approximation; see Sahni and Coles [69] for a review and references therein) are invoked or pressure effects are added (Adler and Buchert [1]; Buchert *et al* [19]). Present day LPT is most suited to model structure formation in the quasi-linear regime where the density contrasts are of the order of 1 to 10.

The use of LPT in cosmology was initiated by Zeldovich [84]. His treatment assumed that the initial velocity field was proportional to the initial acceleration field ("Zeldovich approximation") and focussed only on growing modes.

Buchert [20] showed that this solution was a special case of a more general first order solution of LPT. Further theoretical extensions of the Zeldovich ansatz were carried out by many authors (Moutarde *et al.* [57], Buchert [21], [17], [18], Elhers and Buchert [31], Bouchet [15], [14], [13], Catelan [24] and Munshi *et al.* [58]). A general relativistic version of the Zeldovich approximation was developed by [40] and other relativistic descriptions of the fluid in its rest frame were investigated by [53] and [52, 51]. In more recent times, LPT has been used for many applications such as modeling the non-linear halo mass functions (Monaco [55], Scoccimarro and Seth [72]), BAO reconstruction (Eisenstein *et al* [32]) and setting initial conditions for numerical simulations (Scoccimarro [71], Crocce & Scoccimarro [27]).

Despite its widespread use, LPT, like any other perturbation technique has its limitations. While the breakdown of LPT at shell crossing is expected, it turns out that LPT even fails to reproduce the evolution of spherical homogenous voids (Sahni and Shandarin [70]). In a recent paper (Nadkarni-Ghosh and Chernoff [59], hereafter NC) we investigated this issue of convergence of the LPT series by analyzing the model spherical top hat system. We demonstrated that to ensure convergence for voids, it was necessary to re-expand the solution in overlapping time domains, each domain subject to a time of validity criteria. To the best of our knowledge this has never been recognized or tested in cosmological applications of LPT. It forces one to shift from thinking of the analytic formulation as a single-step method of calculation whose accuracy is limited by perturbation expansion order to something akin to a numerical, multi-step method of solution. This new approach resembles a traditional particle method in that the system is updated on a step-by-step basis. Accuracy will now be determined by step size and expansion order just as particle motions in an N-body code are. LPT retains all the virtues of its analytic formulation that begins with smooth functions rather than discrete particles but becomes considerably more complicated in its application.

Convergence for collapsing models is also limited. In some cases the maximum time is finitely less that the future singularity. Evolution to reach the singularity from such initial conditions requires multiple steps. One might wonder why this behavior had not been previously reported in a model as well-studied as the top-hat. To the best of our knowledge, convergence of LPT has not previously been addressed in a systematic fashion. In addition, it turns out that for initial conditions starting near those prescribed by the Zeldovich ansatz the finite interval mentioned above shrinks to zero, i.e. the convergence limitations become identical to the moment of caustic formation. For such examples LPT-based numerical studies of top-hat collapse would see nothing anomalous. A similar explanation (to be investigated) might apply to general, realistic problems of interest which are initialized from the growing mode.

The Zeldovich ansatz for the top-hat problem implies a specific relationship between the density and velocity perturbations. We showed that in an appropriate density-velocity phase space there is a curve giving an exact, non-linear generalization of the ansatz. It effectively describes the growing mode of the system. This curve plays a special role in the dynamics of the system; initial conditions that start along the the curve continue to stay along it and those that start near it evolve parallel to it. We found that most systems need only a few steps to approach the curve closely enough that the convergence limitation in subsequent evolution becomes identical to the formation of the caustic. Nevertheless, the convergence rate can be improved by working to higher Lagrangian order and/or increasing the frequency of re-expansion. We characterized how the leading order error for the series solution varies with the choice of Lagrangian order and step size.

Our results in the previous paper were based on the special condition of spherical symmetry and uniform density of the spherical top-hat and the background cosmology was $\Omega = 1$. This paper develops a systematic procedure to extend LPT to arbitrary initial conditions. We examine how the convergence of the LPT series for the inhomogeneous system depends upon Lagrangian order, step size and size of the numerical grid. Such tests validate the analytical form of the Lagrangian expansion, the re-expansion procedure that occurs between individual time steps and the method for time-step selection which is based on the convergence analysis of the spherical top-hat. We restrict the tests to small grid sizes, expecting the results to scale for larger grids. A need for such error control in perturbation theory techniques has also been emphasized in a recent paper by Carlson, White and Padmanabhan [23], although this paper focussed on Eulerian perturbation theory.

The organization is as follows: §4.3 re-derives the general formalism set down by Buchert and Elhers [31] for a single step. We extend the treatment to include general dark energy terms in the background evolution. We outline the process of taking multiple steps. §4.4 presents the various tests that were performed to test the convergence of the code with Lagrangian order, step size and grid size. §4.5 presents the conclusion.

4.3 Gravitational field equations in the Lagrangian framework

4.3.1 Equations and initial conditions

Consider a cosmological fluid consisting of pressureless dark matter and dark energy with a constant equation of state $w = p/\rho$. Although it has been suggested that quintessence models with $w \neq -1$ should have spatial fluctuations (for example Caldwell *et al* [22]), these fluctuations are estimated to be small (Mota *et. al* [56], Cooray *et al* [26]). In this work we allow to dark matter to cluster but assume dark energy to be spatially uniform.

On very large scales the fluid is homogeneous and isotropic and is described by the scale factor $a(t)$ which obeys the Friedmann equation. The evolution is completely determined by specifying the initial values of the scale factor a_0, Hubble constant H_0 and matter and dark energy densities $\rho_{m,0}$ and $\rho_{d.e,0}$ respectively. The subscript '0' here indicates an arbitrary initial time and should not be confused with the values for today ($z = 0$).

On smaller scales the fluid is inhomogeneous and is described by the position $\mathbf{r}(t)$ and the velocity $\dot{\mathbf{r}}(t)$ of the fluid elements/particles with respect to to some fixed origin. For sub-horizon scales in the absence of pressure, Newton's law of gravity provides a good description of the dynamics for purely matter dominated universes. Even in the presence of dark energy it can be shown from the equation of geodesic deviation [66] that the acceleration of the fluid element obeys

$$\nabla_r \cdot \ddot{\mathbf{r}} = -4\pi G\left[\rho_m(\mathbf{r}, t) + \rho_{d.e}(t)(1 + 3w)\right] \tag{4.1}$$

$$\nabla_r \times \ddot{\mathbf{r}} = 0 \tag{4.2}$$

where $\rho_m(\mathbf{r}, t)$ and $\rho_{d.e}(t)$ are the total matter and dark energy densities respectively at time t and G is Newton's gravitational constant. ∇_r is the Eulerian gradient operator and the 'dot' denotes derivative with respect to time.

In the Lagrangian framework, the evolution of the fluid is tracked as a function of initial particle labels $\mathbf{X}$ and time t i.e. $\mathbf{r} = \mathbf{r}(\mathbf{X}, t)$. Let these value of the position and velocity at the initial time t_0 be $\mathbf{r}(t_0)$ and $\dot{\mathbf{r}}(t_0)$. Define the Lagrangian coordinates as

$$\mathbf{X} = \frac{\mathbf{r}(t_0)}{a(t_0)}. \tag{4.3}$$

Let $\rho_m(\mathbf{X}, t_0)$ be the total density at the initial time. The perturbation is characterized by two quantities; the initial fractional overdensity

$$\delta(\mathbf{X}, t_0) = \frac{\rho_m(\mathbf{X}, t_0)}{\rho_{m,0}} - 1 \tag{4.4}$$

and the initial peculiar velocity

$$\mathbf{v}(\mathbf{X}, t_0) = \dot{\mathbf{r}}(t_0) - \dot{a}_0\mathbf{X}. \tag{4.5}$$

We require $\int_V \delta(\mathbf{X}, t_0) d^3X = 0$ and $\int_V \mathbf{v}(\mathbf{X}, t_0) d^3X = 0$. We assume that V is a fair sample of the universe and that all functions of $\mathbf{X}$ are periodic.

Conservation of mass implies that the density at any time t is given as

$$\rho_m(\mathbf{X}, t) = \frac{\rho_m(\mathbf{X}, t_0) J(\mathbf{X}, t_0)}{J(\mathbf{X}, t)} \tag{4.6}$$

where $J(\mathbf{X}, t) = Det\left(\frac{\partial r_i}{\partial X_j}\right)$ is the Jacobian of the transformation relating the Eulerian and Lagrangian coordinate systems. This transformation is well defined until orbit crossing. From the definitions eq. (4.3) and eq. (4.4), it follows that $J(\mathbf{X}, t_0) = a_0^3$ and $\rho_m(\mathbf{X}, t_0) = \rho_{m,0}(1 + \delta(\mathbf{X}, t_0))$. This gives

$$\rho_m(\mathbf{X}, t) = \frac{\rho_{m,0}(1 + \delta(\mathbf{X}, t_0)) a_0^3}{J(\mathbf{X}, t)}. \tag{4.7}$$

The density evolution of dark energy for a constant equation of state w is

$$\rho_{d.e}(t) = \rho_{d.e,0}\left(\frac{a_0}{a}\right)^{3(1+w)}, \tag{4.8}$$

In eqs. (4.1) and (4.2), ∇_r is the Eulerian gradient operator. However, in the Lagrangian formalism $\mathbf{r}$ is the dependent variable and $\mathbf{X}$ is the independent variable. Transforming all the derivatives with respect to the Eulerian coordinates to derivatives with respect to the Lagrangian coordinates (see Appendix B.1 for details) and substituting eqs. (4.7) and (4.8) into eqs. (4.1) and (4.2) gives

$$\begin{aligned} \hat{L}[\ddot{\mathbf{r}}, \mathbf{r}, \mathbf{r}] &= -3H_0^2\Omega_{m,0}a_0^3(1+\delta(\mathbf{X}, t_0)) \qquad (4.9)\\ &\quad -\frac{H_0^2}{2}(1+3w)\Omega_{d.e,0}\left(\frac{a_0}{a}\right)^{3(1+w)}\hat{L}[\mathbf{r}, \mathbf{r}, \mathbf{r}] \\ \hat{\mathbf{T}}[\ddot{\mathbf{r}}, \mathbf{r}] &= 0 \qquad (4.10) \end{aligned}$$

where

$$\begin{aligned} \Omega_{m,0} &= \frac{8\pi G\rho_{m,0}}{3H_0^2}, \qquad (4.11)\\ \Omega_{d.e,0} &= \frac{8\pi G\rho_{d.e,0}}{3H_0^2}, \qquad (4.12)\\ \hat{L}[\mathbf{A}, \mathbf{B}, \mathbf{C}] &= \epsilon_{lmq}\epsilon_{ijk}\frac{\partial A_i}{\partial X_l}\frac{\partial B_j}{\partial X_m}\frac{\partial C_k}{\partial X_q}, \qquad (4.13)\\ \hat{T}_q[\mathbf{A}, \mathbf{B}] &= \epsilon_{lmq}\frac{\partial A_k}{\partial X_l}\frac{\partial B_k}{\partial X_m}. \qquad (4.14) \end{aligned}$$

ϵ_{ijk} is the usual Levi-Civita symbol and Einstein's summation convention is used. As a convenient notation we have introduced the scalar operator $\hat{L}$ and vector operator $\hat{\mathbf{T}}$. A list of their properties are given in Appendix B.2. The equations are solved using the perturbation scheme outlined in the next section.

4.3.2 Perturbation scheme

The solution for a particle trajectory $\mathbf{r}$ in the inhomogeneous medium is written as a sum of its homogenous and inhomogeneous displacements. The inhomogeneous displacement vector is further written as a series expansion in terms the initial density and velocity fields. In the formalism outlined by Buchert ([20], [21], [17]) and Elhers and Buchert [31], the two fields are both assumed to be first order. We adopt the same assumed ordering. Write

$$\mathbf{r}(\mathbf{X}, t) = a(t)\mathbf{X} + \mathbf{p}(\mathbf{X}, t) = a(t)\mathbf{X} + \sum_n \mathbf{p}^{(n)}(\mathbf{X}, t)\epsilon^n \tag{4.15}$$

where ϵ is used as a bookkeeping device to track the order. Substitute this ansatz into eq. (4.10) and eq. (4.10), and equate the terms of the same order of ϵ.

At *zeroth order* eq. (4.10) reduces to

$$\frac{\ddot{a}}{a} = -\frac{H_0^2}{2}\left(\frac{\Omega_{m,0}a_0^3}{a^3} + (1+3w)\Omega_{d.e,0}\left(\frac{a_0}{a}\right)^{3(1+w)}\right) \tag{4.16}$$

and (4.10) is identically zero. This is simply the equation governing the background scale factor. Given a_0, H_0, $\Omega_{m,0}$, and $\Omega_{d.e,0}$, the background evolution is completely determined.

At *first order* eqs. (4.10) and (4.10) reduce to

$$\begin{aligned} D_t^L\left[\nabla_{\mathrm{x}} \cdot \mathbf{p}^{(1)}\right] &= -\frac{3}{2}H_0^2\Omega_{m,0}a_0^3\delta(\mathbf{X}, t_0) && (4.17)\\ D_t^T\left[\nabla_{\mathrm{x}} \times \mathbf{p}^{(1)}\right] &= 0. && (4.18)\end{aligned}$$

where,

$$\begin{aligned} D_t^L &= \left(2a\ddot{a} + \frac{3}{2}a^2H_0^2(1+3w)\Omega_{d.e,0}\left(\frac{a_0}{a}\right)^{3(1+w)} + a^2\frac{d^2}{dt^2}\right), && (4.19)\\ D_t^T &= \left(-\ddot{a} + a\frac{d^2}{dt^2}\right). && (4.20)\end{aligned}$$

Note that the Lagrangian derivative operator commutes with the time derivative operator because the Lagrangian coordinate system is independent of time.

$$\frac{d}{dt} = \left.\frac{\partial}{\partial t}\right|_r + \mathbf{v} \cdot \nabla_r = \left.\frac{\partial}{\partial t}\right|_X . \tag{4.21}$$

At *higher orders* eqs. (4.10) and (4.10) reduce to

$$\begin{aligned} D_t^L \left[\nabla_{\mathrm{x}} \cdot \mathbf{p}^{(n)}\right] &= S^{(n,L)}, & (4.22)\\ D_t^T \left[\nabla_{\mathrm{x}} \times \mathbf{p}^{(n)}\right] &= \mathbf{S}^{(n,T)}, & (4.23)\end{aligned}$$

where $S^{(n,L)}$ and $\mathbf{S}^{(n,T)}$ are scalar and vector source terms comprised of combinations of solutions whose order is less than n. The general form is

$$\begin{aligned} S^{(n,L)} &= \sum_{\substack{\alpha,\beta \\ \alpha+\beta=n}} \left(-\frac{1}{2}\ddot{a} - \frac{3}{4} a H_0^2 (1+3w)\Omega_{d.e,0} \left(\frac{a_0}{a}\right)^{3(1+w)}\right) \hat{L}[\mathbf{p}^{(\alpha)}, \mathbf{p}^{(\beta)}, \mathbf{X}] \\ &\quad - \sum_{\substack{\alpha,\beta \\ \alpha+\beta=n}} a\hat{L}[\ddot{\mathbf{p}}^{(\alpha)}, \mathbf{p}^{(\beta)}, \mathbf{X}] - \sum_{\substack{\alpha,\beta,\gamma \\ \alpha+\beta+\gamma=n}} \frac{1}{2}\hat{L}[\ddot{\mathbf{p}}^{(\alpha)}, \mathbf{p}^{(\beta)}, \mathbf{p}^{(\gamma)}] \\ &\quad - \sum_{\substack{\alpha,\beta,\gamma \\ \alpha+\beta+\gamma=n}} \frac{1}{4} H_0^2 (1+3w)\Omega_{d.e,0} \left(\frac{a_0}{a}\right)^{3(1+w)} \hat{L}[\mathbf{p}^{(\alpha)}, \mathbf{p}^{(\beta)}, \mathbf{p}^{(\gamma)}] & (4.24)\\ \mathbf{S}^{(n,T)} &= -\sum_{\substack{\alpha,\beta \\ \alpha+\beta=n}} \hat{\mathbf{T}}[\ddot{\mathbf{p}}^{(\alpha)}, \mathbf{p}^{(\beta)}]. & (4.25)\end{aligned}$$

α, β, γ can take any values from 1 to $n-1$.

The displacement at each order $\mathbf{p}^{(n)}$ is split into its longitudinal (curl-free) and transverse (divergence-less) parts. We write

$$\mathbf{p}^{(n)} = \mathbf{p}^{(n,L)} + \mathbf{p}^{(n,T)} \tag{4.26}$$

where $\nabla_{\mathrm{x}} \times \mathbf{p}^{(n,L)} = 0$ and $\nabla_{\mathrm{x}} \cdot \mathbf{p}^{(n,T)} = 0$. The periodicity of the system guarantees that this decomposition is unique (see Appendix C of Buchert and Elhers [31]). Using this decomposition it is obvious that the longitudinal and transverse parts of the solution at the n-th order obey a different set of equations and can be solved independently. However, note that each of the source terms $S^{(n,L)}$ and $\mathbf{S}^{(n,T)}$ include both the longitudinal and transverse parts of the lower order solutions. So the entire solution at all lower orders is needed to compute either the longitudinal or transverse part of a given order.

Using the definition of the Lagrangian labels and the initial peculiar velocity (eq. (4.3) and eq. (4.5)), the initial conditions are

$$\mathbf{p}^{(1,L/T)}(\mathbf{X}, t_0) = 0, \tag{4.27}$$

$$\dot{\mathbf{p}}^{(1,L/T)}(\mathbf{X}, t_0) = \mathbf{v}^{L/T}(\mathbf{X}, t_0) \tag{4.28}$$

and for $n > 1$ are

$$\mathbf{p}^{(n,L/T)}(\mathbf{X}, t_0) = 0 \tag{4.29}$$

$$\dot{\mathbf{p}}^{(n,L/T)}(\mathbf{X}, t_0) = 0 \tag{4.30}$$

where$\mathbf{v}^{L/T}(\mathbf{X}, t_0)$ are the curl-free and divergence-less parts of the initial velocity respectively.

The eqns. (4.17), (4.18), (4.22) and (4.23) can be further simplified by noting that the spatial and temporal operators commute. The temporal and spatial parts decouple and at each order the problem reduces to solving a set of Poisson equations subject to periodic boundary conditions for the spatial part and a set of second order ordinary differential equations with two initial conditions for the temporal part. The details are outlined in Appendix B.3. The Poisson equations are solved using Fourier transforms on a $N \times N \times N$ grid with equally spaced grid points which represent the Lagrangian coordinates. The temporal solutions are solved numerically using a standard differential equation solver.

4.3.3 LPT re-expansions

The LPT scheme does not converge at all times when applied to expanding spherical top-hat voids [70]. In the previous paper (NC) the authors showed that problem is not restricted to voids but can affect closed overdense models as well. This work showed how to overcome the problem by re-expanding the series in overlapping time domains each domain subject to the time of validity criteria. The analysis was based on spherically symmetric perturbations evolving in a $\Omega = 1$ background cosmology. We assume that the time step for the inhomogeneous evolution can be estimated by treating each point in the box as if it were an isolated top-hat. That is, we use the local density perturbation and the divergence of the local velocity perturbation to calculate the time step that would be allowed for a top hat with those parameters. We adopt the minimum of all the individual time steps.

The fractional overdensity δ and the fractional Hubble parameter δ_v are the two important parameters that govern the time of validity of the series for the spherical perturbation. For generic inhomogeneous initial conditions field the natural generalization of these definitions is

$$\begin{aligned} \delta \equiv \delta(\mathbf{r}, t_0) &= \delta(\mathbf{X}, t_0) && (4.31) \\ \delta_v \equiv \frac{1}{3H_0}\nabla_r \cdot \dot{\mathbf{r}} - 1 &= \frac{1}{3\dot{a}_0}\nabla_X \cdot \dot{\mathbf{p}}(\mathbf{X}, t_0). && (4.32) \end{aligned}$$

The above definitions reduce to the fractional overdensity and peculiar velocity scaled by the Hubble parameter used to estimate the time of validity $T(\delta, \delta_v)$ in NC. We take the minimum of $T(\delta, \delta_v)$ over the Lagrangian grid. Note that the spherical top-hat system has no transverse component and its effect on the time of validity is unknown. As a working hypothesis, we assume that a presence of a transverse component poses no extra limitations on the time of validity.

In existing literature it is common to relate δ and the divergence of the peculiar velocity scaled by the Hubble parameter ($\nabla_r \cdot \mathbf{v}$). In our notation, $\delta_v = \nabla_r \cdot \mathbf{v}/3$. A positive δ at a point implies a overdense region and a positive δ_v implies an expanding region. The time of validity is estimated by evaluating $T(\delta, \delta_v)$ for each point on the grid assuming it evolves as an independent sphere and taking the minimum value over the grid. If the minimum is set by an expanding region then the LPT re-expansion scheme can extend the time of validity. However, if the minimum is set by a collapsing region then the time of validity corresponds to caustic formation. The re-expansion scheme does not include any physics of multi-streaming and to extend beyond this regime other techniques to model this regime must be introduced (for example Adler and Buchert [1]).

Let $\mathbf{X}_0$ be vector labeling particles at time t_0. Use the single step series solution to move forward to time t_1 less than the time of validity. The scale factor of the background at the new time t_1 is denoted as a_1 and $\dot{a}_1$. At t_1, the particles are relabeled with coordinates $\mathbf{X_1}$. The physical position and velocity of the particles is not altered by the labeling. This sets the relationship between the coordinate labels $\mathbf{X}_0$ and $\mathbf{X}_1$ and sets the initial velocity field for the next step:

$$\begin{aligned} \mathbf{r}(t_1) &= a_1\mathbf{X}_1 = a_1\mathbf{X}_0 + \mathbf{p}(\mathbf{X}_0, t_1), && (4.33) \\ \dot{\mathbf{r}}(t_1) &= \dot{a}_1\mathbf{X}_1 + \dot{\mathbf{p}}(\mathbf{X}_1, t_1). && (4.34) \end{aligned}$$

Substituting for $\mathbf{X}_1$ from eq. (4.33),

$$\dot{\mathbf{p}}(\mathbf{X}_1, t_1) = \dot{\mathbf{p}}(\mathbf{X}_0, t_1) - \frac{\dot{a}_1}{a_1}\mathbf{p}(\mathbf{X}_0, t_1). \tag{4.35}$$

In the Lagrangian scheme, the density and velocity are explicit functions of the coordinate label $\mathbf{X}$ and implicit functions of the Eulerian variable $\mathbf{r}$. Therefore at the intermediate time t_1, the physical density associated with a fluid element is independent of the label of the element. This gives

$$\frac{\rho_{m,0}(1+\delta(\mathbf{X}_0,t_0))a_0^3}{J(\mathbf{X}_0,t_1)} = \rho_{m,1}(1+\delta(\mathbf{X}_1,t_1)). \tag{4.36}$$

where $\rho_{m,1}$ is the background density at time t_1 which can be written as $\rho_{m,1} = \rho_{m,0}a_0^3/a_1^3$. This gives the fractional density at time t_1

$$\delta(\mathbf{X}_1,t_1) = \frac{(1+\delta(\mathbf{X}_0,t_0))a_1^3}{J(\mathbf{X}_0,t_1)} - 1. \tag{4.37}$$

It is important to note that the initial conditions are specified on a equispaced three dimensional grid in the space corresponding to the Lagrangian coordinate at that initial time. After the first step, the initial conditions are known on a non-uniform grid in $\mathbf{X}_1$ space. Interpolation must be used to obtain the initial values on a uniform grid in the $\mathbf{X}_1$ space (see Appendix B.4 for details). In the sections that follow we will refer to the $\mathbf{X}_0$ grid as the initial Lagrangian grid and the $\mathbf{X}_1$ grid as the final comoving Eulerian grid. Equations (4.35) and (4.37) set the initial conditions for the next time step beginning at t_1. The longitudinal and transverse parts of $\mathbf{p}(\mathbf{X},t_1)$ are computed as

$$\nabla_{X_1}\cdot\dot{\mathbf{p}}^L(\mathbf{X}_1,t_1) = \nabla_{X_1}\cdot\dot{\mathbf{p}}(\mathbf{X}_1,t_1), \tag{4.38}$$

$$\dot{\mathbf{p}}^T(\mathbf{X}_1,t_1) = \dot{\mathbf{p}}(\mathbf{X}_1,t_1) - \dot{\mathbf{p}}^L(\mathbf{X}_1,t_1). \tag{4.39}$$

The physical position at the end of the second step is

$$\mathbf{r}(\mathbf{X_1},t_2) = a_2\mathbf{X}_1 + \mathbf{p}(\mathbf{X}_1,t_2) \tag{4.40}$$

and at the end of N steps is

$$\mathbf{r}_{physical} = \mathbf{r}(\mathbf{X}_{N-1},t_N) = a_N\mathbf{X}_{N-1} + \mathbf{p}(\mathbf{X}_{N-1},t_N). \tag{4.41}$$

4.3.4 'Zeldovich' initial conditions

At the initial time t_0 the system is completely specified by the initial density field $\delta(\mathbf{X}, t_0)$ and the transverse and longitudinal vector fields $\mathbf{v}^{L,T}(\mathbf{X}, t_0)$. Cosmological numerical simulations are usually started at early times with no vortical modes in the velocity field, so $\mathbf{v}^{T}(\mathbf{X}, t_0) = 0$ and the velocity field is parallel to the acceleration field $\mathbf{F}_\delta$ which is determined by the initial density field via Poisson's equation $\nabla \cdot \mathbf{F}_\delta = \delta(\mathbf{X}, t_0)$. It is usually assumed that only the growing modes are present at the initial time. In NC we showed that this condition established a non-linear relationship between the density and velocity tracing out a curve in the density-velocity phase space. In this paper we impose this condition at linear order, which sets the constant of proportionality between the initial velocity and acceleration fields (see Appendix B.9),

$$\mathbf{v}^{L}(\mathbf{X}, t_0) = -\dot{a}(t_0)\mathbf{F}_\delta(\mathbf{X}, t_0). \tag{4.42}$$

This method of initialization is the usual practice is most other applications of LPT in the literature.

At the initial time the Lagrangian coordinate is related to the Eulerian coordinate by simply a scale factor and requiring irrotationality in the Eulerian space and Lagrangian space are equivalent. In the Eulerian coordinates, the Kelvin circulation theorem guarantees that under the influence for purely conservative forces, a flow that starts out irrotational continues to be irrotational. However, in the Lagrangian coordinate system, this is not true. Even if the initial conditions are irrotational, transverse components can be generated at third order (Buchert [17]) after a single step. The re-initialization at an intermediate step relates the quantities in the initial Lagrangian grid to the current comoving Eulerian grid. In principle, this procedure will guarantee that irrotationality is preserved, but because of a finite numerical grid this procedure may not be exact and this component should not be neglected. It is necessary to allow for a transverse initial mode to keep track of this component for intermediate steps.

4.4 Numerical tests of the code

This section presents tests performed to check the convergence properties of the numerical scheme outlined in §4.3. The Lagrangian order (n), the number of time steps (N_t), and the size of the grid used for the numerical FFTs (N_s) are the three parameters that control the error of the re-expansion scheme and in general convergence to the exact answer requires that all three control parameters are increased simultaneously. We did not attempt to test the convergence in a rigorous manner by simultaneously refining all three parameters according to a given prescription. Instead we assumed that it was sufficient to study various limits in which the dominant error scaling was thought to be due to the variation of a single parameter. To operate correctly the code must necessarily ”pass” such tests (i.e. converge at the expected rate) for each individual parameter. But success for all parameters considered one at a time does not guarantee that any particular prescription for simultaneous refinement of all three parameters will actually converge to the correct answer. We regard our strategy as a reasonable but not rigorous approach to validating the method.

Generally, the exact analytic answer is unknown and convergence is established using the Cauchy convergence criterion i.e difference between successive approximations should decrease. Root mean square errors are usually evaluated in the various dependent quantities such as comoving displacement, comoving peculiar velocity and fractional overdensity. The general Cauchy error in a function f is defined as

$$\mathcal{E}(\alpha) = \langle |f^{(\alpha+\beta)}(\mathbf{X}, t) - f^{(\alpha)}(\mathbf{X}, t)| \rangle \tag{4.43}$$

where α is n, N_t or N_s for Lagrangian order, number of time steps and spatial resolution respectively, f is $\mathbf{p}/a(t), \dot{\mathbf{p}}/a(t)$ or δ for comoving displacement, comoving peculiar velocity and comoving density respectively and t refers to the time at which the error is evaluated. $f^{(\alpha+\beta)}$ is a better approximation than $f^{(\alpha)}$. Convergence tests with n, N_t have $\beta = 1$ (§4.4.3, §4.4.4) and with respect to N_s, $\beta = 8$ (§4.4.2). $\mathbf{X}$ refers to either the initial Lagrangian grid or the final comoving Eulerian grid. The average $\langle\rangle$ denotes the root mean square error over the grid used. In the plots presented, $\mathcal{E}$ is subscripted by p, v or δ referring to comoving position, comoving peculiar velocity and density respectively.

Although it is standard practice to monitor Cauchy differences to assess numerical convergence, the method does not guarantee that the converged solution is the desired solution. For example, it is possible to obtain convergence in the Cauchy sense, but to the wrong answer if there is an error in the equations. To minimize this possibility we begin by testing the numerical code on a problem with a known exact analytic answer, the spherical top-hat. There are two drawbacks however. First, the spatial discontinuities in the top-hat solution ruin the expected rate of convergence (with grid size) for smooth solutions. Second, the top-hat dynamics exercises only the subset of the equations describing longitudinal flows. Nevertheless, it serves as an excellent test in view of the geometric difference between the solution (spherical) and calculation domain (rectangular). Subsequent Cauchy convergence tests for each of the three parameters are carried out on generic smooth problems. All tests are done in a $\Omega = 1$ background cosmology and the time intervals of evolution always respect the time of validity criterion.

4.4.1 Evolution of a spherical top-hat overdensity

The physical configuration is an overdense sphere surrounded by a vacuum compensating region. The initial velocity perturbation is set to zero. For this special case, the solutions for the displacement and density can be computed analytically for every order. Convergence can be analyzed by comparing the numerical n-th order solution to the analytic n-th order solution. This makes the system a good test case to debug various spatial routines of the numerical code. The main numerical complication is that the exact top-hat profile is discontinuous along the transition boundaries between the overdense sphere and the vacuum compensating region. Consequently, its Fourier transform is not bandwidth limited and the Gibbs' phenomenon masks any differences between the expected and observed behavior. To suppress this numerical artifact, the discontinuous profile is smoothed by a gaussian in a manner described below. The resulting distribution is evolved using third order LPT from the initial time to the final time, ensuring that the latter is within the range of validity of the series. Details of the functional form of the initial profile and the smoothing procedure can be found in the Appendix B.10. At the final time t_f, the numerical values of the density ρ_n with respect to the initial Lagrangian grid are compared to the analytical values ρ_a. The relative r.m.s. error between the expected and true density is defined as

$$\Delta_{r.m.s.} = \frac{1}{\rho_{max,a}} \langle |\rho_n(\mathbf{X}, t_f) - \rho_a(\mathbf{X}, t_f)| \rangle \tag{4.44}$$

The average is over the initial Lagrangian grid and $\rho_{max,a}$ represents the height of the top-hat density peak. The width of the gaussian, σ, was chosen to scale as $4/N_s$. The numerical and analytic initial density profiles differ due to finite grid size N_s and finite σ. By design the numerical representation of the initial profile approaches the exact initial profile in the limit $N_s \to \infty$; the r.m.s. error $\propto 1/\sqrt{N_s}$. We study the convergence of the final profile to the exact analytic final profile. Roughly speaking, for the optimum convergence rate the r.m.s. errors are anticipated to scale as $1/\sqrt{N_s}$. Figure 4.1 shows the log of the error as a function of the grid size N_s for four different final times. The points represent the numerical values and the solid lines are the best fit curves. Appendix B.10 shows that the convergence rate should scale as $1/\sqrt{N_s}$ and the numerical fits to the data shown in table (4.1) agree with the expected behavior. It must be emphasized that this is a particularly bad convergence rate. However, it arises from the errors made in the representation of the discontinuous function on a finite grid and it does not reflect the convergence rate of the Lagrangian series for smooth initial conditions. The purpose of this test was to show that the LPT scheme approached the known analytic solution; later we assess the rate of convergence for smooth initial conditions.

4.4.2 Convergence with grid size N_s

In this test smooth periodic initial conditions are evolved for a fixed time interval at a fixed Lagrangian order and compared as grid size N_s increases. Our implementation of the LPT scheme relies on FFT methods to solve all spatial

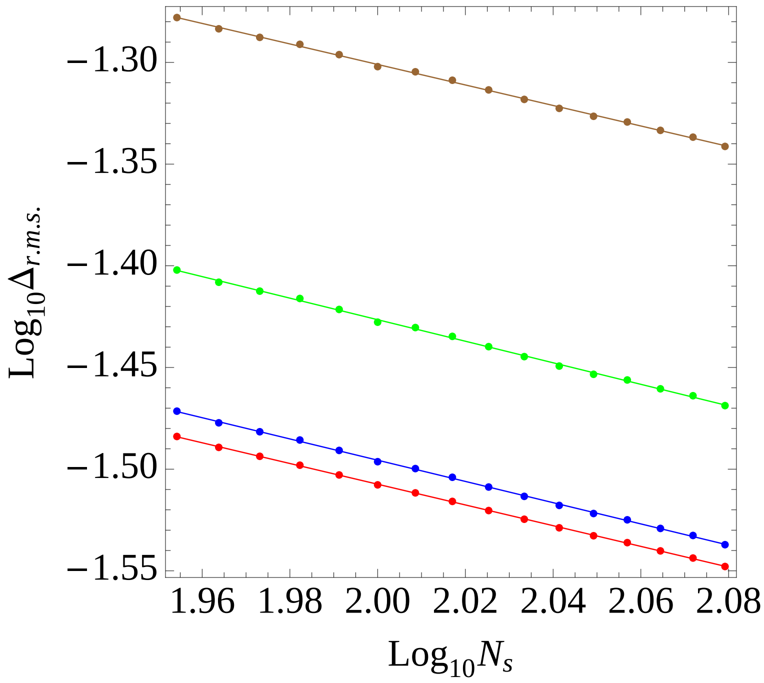

Figure 4.1: Testing the code with spherical top-hat evolution. Log of the relative r.m.s. errors between the third order numerical and the third order analytic solution vs. grid size N_s. The dots are the data and lines provide empirical fits at four different times (bottom to top indicates increasing final times). times). See Table 4.1 for the numerical fits. The key point is that the relative r.m.s. error scales as $1/\sqrt{N_s}$ agreeing with the expected behavior for discontinuous functions.

equations in a periodic universe. We check that the convergence with with grid parameter N_s (for fixed final time and fixed Lagrangian order) matches that anticipated for the spectral techniques that are employed. Such techniques are expected to display exponential convergence (Boyd [61]). The density field is generated by smoothing a compensated discontinuous top-hat function with a gaussian of a fixed width. To ensure periodicity of the initial data, contribution of the 26 nearest neighbors cells is added. The contribution of cells beyond the nearest neighbors was zero to machine precision. A smooth velocity field is created by taking each component of the field to be proportional to the

Table 4.1: Numerical fits indicating scaling of the relative r.m.s. error between the exact and the numerical densities on the grid calculated with single step third order LPT. The time at which the error is evaluated is denoted as a fraction of the collapse time t_c.

t/t_c	$\Delta_{r.m.s}$
0.47	$0.32N_s^{-0.51}$
0.61	$0.35N_s^{-0.52}$
0.75	$0.43N_s^{-0.53}$
0.89	$0.51N_s^{-0.50}$

density field with an arbitrary proportionality constant. The resulting velocity profile has both longitudinal and transverse velocities. The initial values of the acceleration and velocity fields are given in table 4.5. Five runs ranging from $N_s = 24$ to $N_s = 56$ were performed the on same initial data for first, second and third Lagrangian order and the comoving displacement, comoving peculiar velocity and density were evaluated as functions of the initial Lagrangian grid.

Figure 4.2 shows the Cauchy errors as defined in eq. (4.43) for evolution using the second order scheme. The errors for the first and third order schemes show a similar behavior. The circles, squares and diamonds denote the numerical values and dotted, dashed and dot-dashed lines are fits for the errors in comoving displacement, comoving velocity and density respectively. The log of the error vs. the grid size is a straight line well-fit by an exponential form. The results for this test demonstrate that spectral accuracy of the spatial solution is indeed achieved. The fits are given in table 4.2.

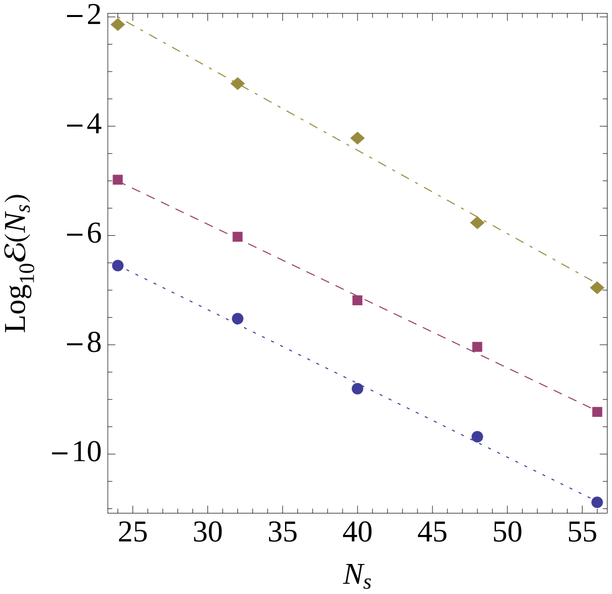

Figure 4.2: Convergence with the grid size. Errors $\mathcal{E}_p(N_s)$, $\mathcal{E}_v(N_s)$, $\mathcal{E}_\delta(N_s)$ are denoted by the dots, squares and diamonds respectively. The fits (table 4.2) show that the errors decrease exponentially with the grid size as expected.

Table 4.2: Scaling of the r.m.s. error for increasing the size of the grid.

$\mathcal{E}_p(N_s)$	$10^{-3.3}0.74^{N_s}$
$\mathcal{E}_v(N_s)$	$10^{-1.85}0.74^{N_s}$
$\mathcal{E}_\delta(N_s)$	$10^{1.65}0.70^{N_s}$

4.4.3 Convergence with Lagrangian order n

In this test, a single realization of the density field arising from Gaussian initial conditions is specified on the grid (see Appendix B.11 for details regarding the set up). The initial velocity vector field is taken to be irrotational and its longitudinal component is set by requiring "Zeldovich initial conditions" discussed in 4.3.4. The choice of irrotationality means that there are only two terms at first order. This simplifies the LPT hierarchy and allows for calculations to be performed up to fourth order in the Lagrangian expansion parameter for the small grid size of $N_s = 16$. The simplification does not imply that there are no transverse terms at higher order; it only means that higher order terms that depend on the first order transverse piece are zero. Transverse terms at third order still arise from combinations of first and second order longitudinal terms.

The tests in the previous section demonstrated that the spatial errors decreased exponentially with grid size for fixed Lagrangian order and fixed step. In this section we aim to isolate and test the impact of Lagrangian order. We will fix the step size and choose initial conditions for which we anticipate grid-related errors at fixed N_s to be so small that they should not interfere with the Cauchy differences for varying Lagrangian order. We proceed as follows. The power in the initial data is truncated at half the Nyquist frequency. Since gravitational dynamics is intrinsically non-linear we anticipate that the power in the initially zeroed modes will grow. Because N_s is fixed, ultimately, any power that reaches or exceeds the Nyquist frequency will manifest as error. We limit the interval of evolution in time and monitor the power that builds up in initially zeroed modes to make sure that the spatial errors remain negligible.

In the figures to follow, the power in the Nyquist mode, which provides a measure of the finite grid effects is plotted along with the Cauchy errors. Given a numerical representation of any function f, we define the power in the Nyquist mode as

$$\mathcal{P}_{Nyq.} = \sqrt{\frac{1}{N_s^3} \sum_{\substack{k_x,k_y,k_z \\ k_x||k_y||k_z=k_{Nyq.}}} |\tilde{f}^{n+1}(k_x,k_y,k_z) - \tilde{f}^{n}(k_x,k_y,k_z)|^2} \sim \sqrt{\frac{1}{N_s^3} \sum_{\substack{k_x,k_y,k_z \\ k_x||k_y||k_z=k_{Nyq.}}} |\tilde{f}(k_x,k_y,k_z)|^2} \tag{4.45}$$

The last approximation can be made because for all Lagrangian orders, the Nyquist components are of the same order of magnitude and their differences are approximately equal to the individual values. Note that this definition allows one to compare the Nyquist errors to the Cauchy errors. The latter are are r.m.s. differences of f between successive Lagrangian orders and Parseval's theorem (Press *et al* [67]) equates the r.m.s. of these differences in real space to differences in Fourier space. The definition above picks out only the Nyquist contribution to the r.m.s. of the differences in Fourier space. At the end of a single step and before reinitializing, the displacement and velocity always have zero Nyquist power because they are solutions to Poisson's equations (see appendix for algorithm). So, the power in the next-to-Nyquist mode is taken to be the measure of error.

The initial conditions are specified at $t = t_0$ and the system is evolved forward for a small time interval Δt using a single step. The details of the initial conditions can be found in table 4.5. The final displacement and velocity are evaluated at five different final times, each time less than the time of validity of the series. The n-th term in the LPT series is of the form ϵ^n, where ϵ is the magnitude of the initial perturbation. Therefore, the log of the Cauchy error on the initial Lagrangian grid is expected to scale linearly with n. It is also necessary to check that the interpolation step relating the quantities on the initial Lagrangain grid to the final comoving Eulerian grid also preserves the behavior of the error terms. In this test errors were evaluated with respect to both grids.

Figure 4.3 shows the log of the Cauchy error vs. Lagrangian order, on the initial Lagrangian grid. The first, second and third panels display the errors in the comoving displacement, comoving peculiar velocity and fractional overdensity respectively. The points are the log errors and the lines are empirical fits. The five solid lines are the errors at five different snapshots. The five dashed lines, color coded like the solid lines, indicate the amount of power in the next-to-Nyquist frequency for the first and second panel and the power in the Nyquist frequency for the third panel. The interpretation of the figure is clear: the size of the spatial error inferred from the high frequency power is always small compared to the Cauchy difference with respect to Lagrangian order. This shows that the effort to isolate and test the effect of Lagrangian order has been successful. Note that the log errors decrease linearly with Lagrangian order, agreeing with the expected behavior.

Figure 4.4 compares the errors calculated on the Lagrangian grid (established at the initial time) and the comoving Eulerian grid (at the final time). The left and right panels show the errors in the total velocity and density as a function of Lagrangian order. The points and the solid lines are the data and fit for the errors on the Lagrangian grid while the dashed lines are errors calculated on the Eulerian grid. We infer that the reinitialization calculation that connects the initial Lagrangian grid to the final comoving Eulerian grid does not introduce any order dependent errors.

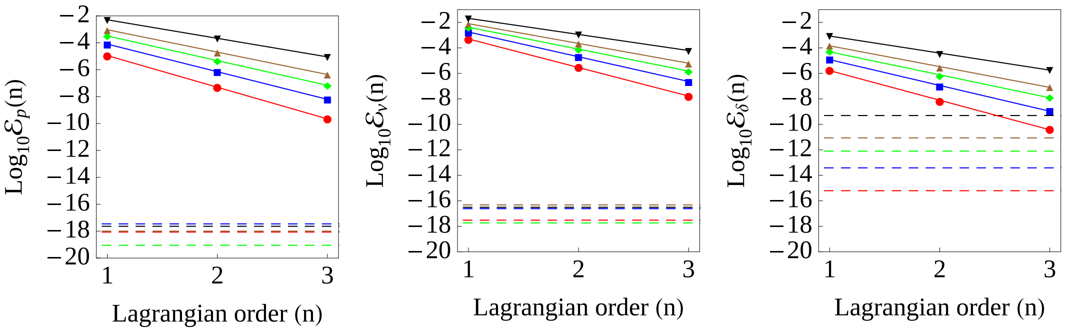

Figure 4.3: Cauchy errors $\mathcal{E}_p(n)$, $\mathcal{E}_v(n)$ and $\mathcal{E}_\delta(n)$ evaluated over the initial Lagrangian grid. The points are the data and the solid lines are the fits given in table 4.3. A single step is used to propagate the series up to a given time. Lines from bottom to top indicate increasing final times. The dashed lines show the power in next-to-Nyquist mode (first and second panel) and Nyquist mode (third panel) indicating that the results are not limited by errors due to lack of representation of power beyond the Nyquist frequency.

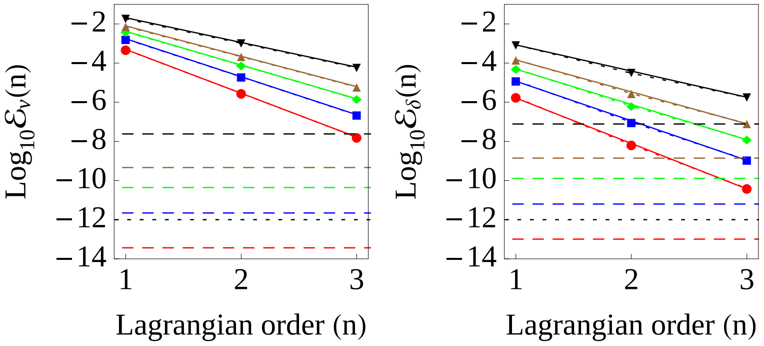

Figure 4.4: Comparing errors with respect to the initial Lagrangian grid and the final comoving Eulerian grid. The left and right panels show the comoving peculiar velocity and density terms respectively. The solid lines and dashed lines indicate the errors with respect to the initial Lagrangian final Eulerian grid respectively. At all times the interpolation procedure preserves the expected convergence rate. Dashed lines indicate the power in the Nyquist frequency and have the same color coding as figure 4.3. The dotted line shows the interpolation error that relates the Lagrangian grid to the final Eulerian grid.

Table 4.3: Convergence of the error with Lagrangian order n. Fits to the lines shown in figure 4.3 for the scaling of the r.m.s. error for displacement, peculiar velocity and fractional overdensity

	Time				
	$\Delta t/t_0 = 0.1$	$\Delta t//t_0 = 0.2$	$\Delta t/t_0 = 0.33$	$\Delta t/t_0 = 0.5$	$\Delta t/t_0 = 1$
$\log_{10} \mathcal{E}_p(n)$	$-2.4n - 2.6$	$-2.0n - 2.0$	$-1.8n - 1.7$	$-1.7n - 1.4$	$-1.4n - 0.9$
$\log_{10} \mathcal{E}_v(n)$	$-2.2n - 1.1$	$-1.9n - 0.8$	$-1.7n - 0.7$	$-1.6n - 0.5$	$-1.3n - 0.4$
$\log_{10} \mathcal{E}_\delta(n)$	$-2.3n - 3.5$	$-2.0n - 2.9$	$-1.8n - 2.5$	$-1.6n - 2.2$	$-1.3n - 1.7$

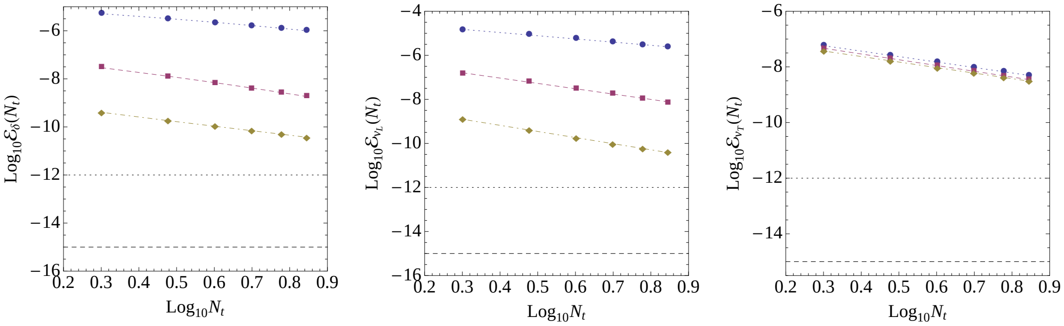

Figure 4.5: Convergence with respect to frequency of re-expansion. Errors $\mathcal{E}_\delta(N_t)$, $\mathcal{E}_{v_L}(N_t)$, $\mathcal{E}_{v_T}(N_t)$ plotted as functions of number of steps N_t. The points indicate data and lines indicate fits. Dots, squares and diamonds indicate first, second and third order respectively. The errors decrease as more steps are taken; the higher the order the smaller the error. The spacing with Lagrangian order for the transverse velocity term does not agree with the spacing for the density and longitudinal velocity. This behavior may be because of the finitely many Lagrangian orders explored. This issue is explored further in figure 4.6. Dashed line indicates the Nyquist errors and dotted line indicates the error in the interpolation step that relates the Lagrangian grid to the Eulerian grid. These errors do not interfere with the errors for the convergence test.

4.4.4 Convergence with number of steps N_t

In this test, the fixed initial data is evolved from a fixed initial time t_0 to a fixed final time t_f using increasing number of time steps N_t. For each run the grid size was taken to be $N_s = 16$ and final densities and velocities were computed using first, second and third Lagrangian order. The initial density and velocity fields are generated from random Gaussian fields with their power truncated at half the Nyquist frequency. The velocity field was taken to have both rotational and irrotational components of nearly equal magnitudes. This was one tenth of the magnitude of the acceleration field at the initial time. This run presents a qualitatively new case because it also enables us to study the n dependence of the convergence in the presence of transverse velocities.

The initial time $t_0 = 2/3$ and the final time $t_f = 6$. The r.m.s strengths at the initial time are given in table 4.5. At the final time, the density field grew by a factor of 2.5 and the longitudinal velocity grew by a factor of 300. The transverse field decayed by a factor of 4. Seven runs with N_t ranging from 2 to 8 were performed. The Cauchy errors for the comoving displacement, comoving peculiar velocity and density were evaluated on the final comoving Eulerian grid.

Figure 4.5 shows these errors with the first, second and third panel showing the fractional overdensity, the comoving longitudinal and comoving transverse velocity fields respectively. In each panel the dots, squares and diamonds represent calculations with first, second and third Lagrangian order respectively. The dotted, dashed and dot-dashed lines are fits to the data (table 4.4). The dotted line indicates the accuracy to which the interpolation to the Eulerian grid was performed and the dashed line indicates the power in the

Nyquist mode. It is clear that they do not interfere with the Cauchy errors. As expected, the errors converge as the frequency of re-expansion is increased. This is qualitatively in agreement with the results for the spherical case examined in NC.

It is clear from the figure that the convergence in the transverse velocity term is quite different from the convergence in the longitudinal velocity and density terms. In particular, no significant improvement is seen with Lagrangian order. This may be because of the limited range of Lagrangian orders explored. A justification is given below. At any time, let the strengths of the acceleration, longitudinal and transverse velocity fields be denoted by ϵ_δ, ϵ_{v_L} and ϵ_{v_T} respectively. Although, formally these are assumed to have the same magnitude in the Lagrangian expansion, they can have different values. For example, in the Zeldovich approximation, $\epsilon_\delta = \epsilon_{v_L}$, but $\epsilon_{v_T} = 0$. The second order fields depend on product of first order fields. The longitudinal fields at second order can have six possible strengths - three terms that arise due to self interactions $\epsilon_\delta^2, \epsilon_{v_L}^2, \epsilon_{v_T}^2$ and and three cross terms $\epsilon_\delta\epsilon_{v_L}, \epsilon_\delta\epsilon_{v_T}, \epsilon_{v_L}\epsilon_{v_T}$. The transverse terms however, have no self interaction terms and have only the three cross term strengths. Furthermore, if the first order acceleration and longitudinal velocity are parallel, then only the $\epsilon_\delta\epsilon_{v_T}, \epsilon_{v_L}\epsilon_{v_T}$ terms remain.

Suppose the leading strength at first order is ϵ_δ, then the leading strength at second order for the longitudinal piece is ϵ_δ^2, and at third order is ϵ_δ^3 etc. and the magnitudes of the longitudinal pieces scale systematically with the Lagrangian order n. If ϵ_δ, ϵ_{v_L} and ϵ_{v_T} have the same strengths at the beginning of the evolution and maintain their relative magnitudes throughout the evolution then the leading order errors for the transverse terms can also be expected to have the same scaling behavior as the transverse term. However, it is well known that the in a conservative force field such as gravity transverse peculiar velocity decays as $1/a$, where as the magnitude of the density and velocity increase. Therefore, the magnitude of the second order transverse velocity $\epsilon_\delta \epsilon_{v_L}$ can in some cases be higher than the magnitude of the first order transverse velocity and the errors for the transverse velocity will not scale as ϵ_δ^n for the first few orders. For this particular example, the values were $\epsilon_\delta = 7.2 \times 10^{-2}$, $\epsilon_{v_L} = 3.4 \times 10^{-4}$ and $\epsilon_{v_T} = 4.4 \times 10^{-4}$. Therefore, the strength of the transverse second order term after one step is 1/10 that of the longitudinal term at second order. With multiple steps, this problem becomes more extreme since the values of ϵ_δ and ϵ_{v_L} grow at each intermediate time while the strength of v_T decays. This explains the bunching of the lines for the transverse velocity errors in figure 4.5. However, in the limit that the Lagrangian order tends to infinity, one expects to observe the expected asymptotic behavior. Due to limited memory, it is difficult to test this case with higher order Lagrangian schemes. Instead, we simply check that the kinematic behavior of the transverse velocity is as expected.

As a test of the kinematics, we examine the behavior of the transverse peculiar velocity. In an expanding cosmology with no gravity, the peculiar velocity always decays as $1/a(t)$. In the presence of gravity, the longitudinal peculiar velocity can grow but the transverse part continues to decay. This behavior was verified. Figure 4.6 shows the decay of the transverse velocity. The first panel plots of the log of the r.m.s. value of the transverse velocity vs. the scale factor evaluated at intermediate time steps for the $N_t = 8$ run. The root mean square velocity at the end of each intermediate time step is shown by the dots. A numerical fit to the dots gives a slope of -0.99 which is very close to the expected slope of -1. This behavior was the same for all Lagrangian orders. The second panel shows the decay rate $\mathcal{D} = d \log v_T / d \log a$ compared to the expected value of -1. The difference $\mathcal{D} - (-1)$ decreases with the number of steps N_t. Most cosmological codes, start with Zeldovich initial conditions which imply a zero transverse peculiar velocity. Although for such initial conditions, non-zero transverse terms in Lagrangian space are generated at third order (Buchert [17]), the process of interpolation which relates the quantities back onto the Eulerian grid, will ensure that the irrotationality in Eulerian space is preserved.

For the homogenous spherical case, it was observed that the rate of convergence was higher for higher orders. Here, we observe from the density and longitudinal velocity that the rates of convergence for a second order scheme are slightly better than the first order scheme, however, the rates for the second and third order scheme seem to be comparable. Our working assumption is that this weak dependence on order might arise due to the effect of inhomogeneities. The intuition based on the spherical system does not include the effect of interactions between modes. This effect of interactions is worst when the interactions are so strong that the Nyquist errors interfere with the convergence due to time steps. When this limit is reached, one does not expect to see any convergence with Lagrangian order or time steps unless the grid size in increased. But even before the limit is reached, the effect of interactions, may weaken the order dependence of the scheme. Furthermore, the spherical case has no transverse velocity terms, and the effect of such terms on the convergence of the system cannot be predicted analytically.

The results in this section are subject to further investigation. Although, we expect results similar to the top-hat, we observe two main differences. First, the scaling is not as expected for a top-hat. Higher order errors do not converge

Table 4.4: Scaling of the r.m.s. error between the calculations with N_t and $N_t + 1$ steps for different Lagrangian orders

	Lagrangian Order		
	$n = 1$	$n = 2$	$n = 3$
$\mathcal{E}_\delta(N_t)$	$10^{-4.87}N_t^{-1.3}$	$10^{-6.84}N_t^{-2.2}$	$10^{-8.8}N_t^{-1.9}$
$\mathcal{E}_{v_L}(N_t)$	$10^{-4.38}N_t^{-1.44}$	$10^{-6.06}N_t^{-2.42}$	$10^{-8.07}N_t^{-2.77}$
$\mathcal{E}_{v_T}(N_t)$	$10^{-6.6}N_t^{-1.96}$	$10^{-6.7}N_t^{-2.07}$	$10^{-6.8}N_t^{-1.98}$

faster with N_t. Secondly, spacing of the errors for the transverse velocities is not the same as that for the longitudinal. There are two possibilities that might explain this scenario:

1. The test was not done in the asymptotic limit of a small time step, which was the limit for the error predicted based on the top-hat. A smaller time step for the case presented here gave errors that were indistinguishable from numerical precision. To ensure that the errors are not contaminated by machine precision, one has to test a case which starts with a higher initial amplitude and preferably equal magnitudes of density, longitudinal and transverse velocity. However, for this case, the error in the Nyquist component grows rather rapidly and it is difficult to complete the test on the 16^3 grid. Thus one has to resort to higher grid sizes.
2. The effect of inhomogeneities is responsible for the change in behavior between the spherical top-hat and generic initial conditions.

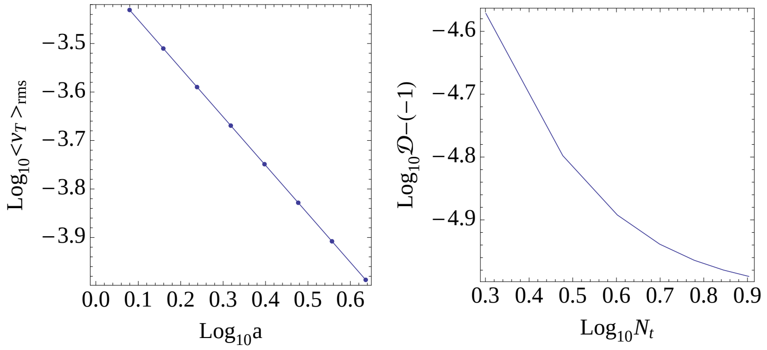

Figure 4.6: Decay of the transverse velocity $v_T \sim 1/a(t)$. The first panel shows the run with $N_t = 8$. The points represent the numerical data and line represents the fit. The observed behavior was very close to the expected behavior. The second panel shows the error in the rate of decay vs. time steps N_t. The expected value of $\mathcal{D} = d\log v_T/d\log a$ is -1. As expected the decay rate decreases with the number of time steps N_t.

4.5 Conclusion

The numerical code for generic initial conditions with third order LPT was implemented and tested. Convergence was demonstrated with respect to the three control parameters Lagrangian order n, number of steps N_t and size of the grid N_s. The scaling of the error with n and N_s was exponential and with N_t was algebraic. In general, convergence to the exact answer can only be obtained when the grid size and time steps (or Lagrangian order) are increased simultaneously. However, if the functions are bandwidth limited, then the finite grid size effects do not play a role in determining convergence. Such cases were examined here. The convergence rates observed for inhomogeneous initial

Table 4.5: Table of initial conditions for runs that examine convergence with N_s, n and N_t. The starting time was always $t_0 = 2/3$. The ϵ_δ, ϵ_{v_L} and ϵ_{v_T} denote the r.m.s. magnitudes of the initial acceleration, initial longitudinal and initial transverse velocities respectively. The table below gives the r.m.s. values of the initial and final δ and δ_v.

Convergence parameter	$\Delta t/t_0$	ϵ_δ	ϵ_{v_L}	ϵ_{v_T}
N_s (§4.4.2)	0.1	4.8×10^{-2}	2.9×10^{-2}	4.2×10^{-2}
n (§4.4.3)	0.5	1.4	1.4	0
N_t (§4.4.4)	8	7.2×10^{-2}	3.4×10^{-4}	4.4×10^{-4}

Convergence parameter	δ_i	δ_f	$\delta_{v,i}$	$\delta_{v,f}$
N_s (§4.4.2)	0.72	0.81	0.53	0.55
n (§4.4.3)	0.15	0.25	0.15	0.25
N_t (§4.4.4)	7.9×10^{-3}	2×10^{-2}	3.7×10^{-5}	1.9×10^{-2}

conditions are not comparable to those observed for the spherical top-hat. The convergence rate with number of steps did not show as strong dependence on order as it did for the spherical top-hat system. This issue is under investigation.

The aim of this paper was to outline the algorithm to take multiple time steps and to implement and check that it converges. This aim has been achieved. Although for most tests the convergence rates are as expected, the rates for convergence with N_t in §4.4.4 differ from expectations based on the top-hat and this issue is still under investigation. The exact number of time steps, Lagrangian order and grid size will ultimately depend on the application at hand and this issue is not addressed in this paper. Usually for a real application, one is limited to a finite grid size. Non-linearities always grow and eventually, the power in the Nyquist modes increases enough that the results cannot be trusted and the simulation has to be stopped. Given a fixed error requirement, the error control parameters will vary according to the redshift range and mass scales that need to be resolved. Furthermore, this scheme does not address the main drawback of LPT which is its inability to go beyond shell crossing. Any approximation to model this regime will further introduce errors and they will have to be balanced against the error parameters discussed in this paper.

CHAPTER 5

PHASE SPACE DYNAMICS AS PROBE TO CONSTRAIN THE DARK ENERGY EQUATION OF STATE

Preliminary results of an application of the code are presented here.

5.1 Introduction

This chapter aims to extend our previous work by investigating the phase space evolution for inhomogenous initial conditions evolving in cosmologies with non-zero dark energy.[1] In particular, we focus on the behavior of the Zeldovich curve and examine how the evolution is influenced by the effect of interactions and a change in the background cosmology. Early studies of the density-velocity relationship were mainly restricted to the linear or quasi-linear regime in matter dominated cosmologies (see Peebles [63], Nusser *et al* [60]), Bernardeau [10], review articles by Willick and Strauss [76] and Dekel [29]) and was further examined in the non-linear regime by Bernardeau *et al*, [8], Bilicki and Chodorowski [12]). The main goal of these studies was to use the density-velocity relationship to get bias independent measures of mass from peculiar velocity measurements or to constrain the matter density parameter today Ω_m (subject to a bias factor) from observations of the local universe.

In this work we adopt a different approach and assume that the values of the matter density parameter Ω_m and dark energy density parameter $\Omega_{d.e}$ today

---

[1] We assume in this paper that the observed acceleration of the universe is caused by a some form of dark energy characterized by an equation of state w. Other explanations for this acceleration based on modifying gravity or back reaction of inhomogeneities are not considered here.

are well constrained by recent cosmological observations (for e.g WMAP, BAO, SNe), but allow the equation of state w to be a free parameter and investigate the w-dependence of the Zeldovich curve. Using the growth history of structure is a commonly used technique to unravel the nature of dark energy. However, most of the work in the recent past has focussed on the growth of densities via the power spectrum or mass function (see for e.g. McDonald *et al* [54], Linder and Jenkins[46], Linder and White [48], Percival [64]), which is only one of the parameters that describes perturbations. This paper aims to demonstrate that the joint density-velocity evolution can serve as another useful probe to distinguish between various dark energy scenarios.

5.2 Dynamics in phase space

Most applications of LPT start with the 'Zeldovich' ansatz which requires that the background cosmology and the perturbations have the same big bang time. Imposing the equal bang time condition sets a relationship between the quantities δ and δ_v which maps out a curve in phase space referred to as the "Zeldovich curve". In NC we examined the implications of this condition for a spherical top hat perturbation and showed that this solution had the special property that top-hat initial conditions that started along this curve stayed on the curve as they evolved and those that started near it stayed near it or moved parallel to it.

Our investigation in the previous paper was based on a homogenous density spherical top-hat evolving in a $\Omega_m = 1$ universe. However, cosmologically interesting initial conditions arise from Gaussian random fluctuations and

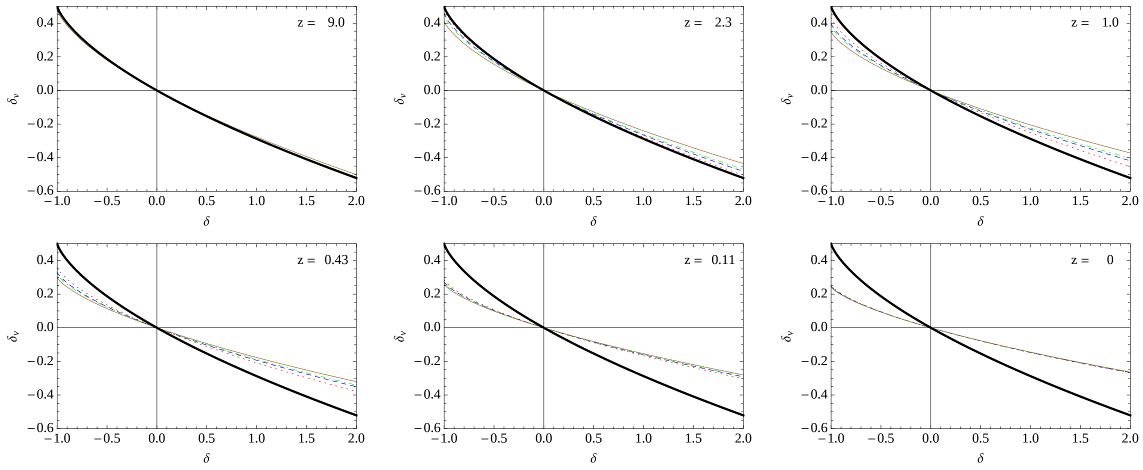

Figure 5.1: Zeldovich curve for different cosmologies. The red (dotted), blue (dashed), green (dotdashed) and brown (plain) curves correspond to $w = -1, -3/4, -2/3, -1/2$ respectively. All four cosmologies are flat have the same value of Ω_m and Ω_{de} today. The thick black curve corresponds to $\Omega_m = 1$ and does not change with z. The smaller the Ω_m, the smaller is the instantaneous growth rate of the model and shallower the curve.

evolve in a universe that has a non-zero dark energy component. This leads to two differences. Firstly, the Zeldovich curve based on the spherical top-hat differs from its $\Omega_m = 1$ version because of the change in the background cosmology and secondly tidal interactions cause the evolution of inhomogenous perturbations to deviate from the curve. In this section, we examine the effect of background cosmology.

5.2.1 Zeldovich curve for arbitrary cosmologies based on the spherical top-hat

The evolution of the background in the presence of dark energy is

$$\frac{\ddot{a}}{a} = -\frac{H_i^2}{2}\left(\frac{\Omega_{m,i}a_i^3}{a^3} + (1+3w)\Omega_{d.e,i}\left(\frac{a_i}{a}\right)^{3(1+w)}\right) \tag{5.1}$$

where, $H_i, \Omega_{m,i}, \Omega_{d.e,i}$ are the Hubble parameter and density parameters at the initial time t_i. The initial conditions are $a(t_i) = a_i$ and $\dot{a}(t_i) = \dot{a}_i$. Consider a compensated spherical top-hat perturbation with scale factor $b(t)$ evolving in this background. If δ_i and $\delta_{v,i}$ are the parameters describing the initial perturbation, then the evolution of $b(t)$ is given by

$$\frac{\ddot{b}}{b} = -\frac{H_i^2}{2}\left(\frac{\Omega_{m,i}a_i^3(1+\delta_i)}{b^3} + (1+3w)\Omega_{d.e,i}\left(\frac{a_i}{a}\right)^{3(1+w)}\right), \tag{5.2}$$

with initial conditions $b(t_i) = a_i$ and $\dot{b}(t_i) = \dot{a}_i(1+\delta_{v,i})$. Note here that the dark energy is assumed to be homogenous throughout space and hence its evolution in the region of matter perturbation depends on the background scale factor and not the perturbed scale factor. The matter and dark energy density parameters at any scale factor a_i are related to the corresponding parameters today ($a_0 = 1$) as

$$\Omega_{m,i} = \left(1 + \frac{\Omega_{d.e,0}a_i^{-3w}}{\Omega_{m,0}}\right)^{-1} \tag{5.3}$$

$$\Omega_{de,i} = \left(1 + \frac{\Omega_{m,0}}{\Omega_{d.e,0}a_i^{-3w}}\right)^{-1}. \tag{5.4}$$

$\Omega_{m,0} = 0.3$, $\Omega_{d.e,0} = 0.7$ are chosen in rough accordance with WMAP (Komatsu [42]). It is shown in the appendix C.1 that the Hubble parameter can be scaled out of the system of equations and its actual value is not needed for the calculations. The universe is taken to be flat so that $\Omega_{m,i} + \Omega_{d.e,i} = 1$ at all times. If $\Omega_{m,0} = 1$, $\Omega_{m,i} = 1$ for all i. This is referred to as the $\Omega_m = 1$ cosmology.

Given the initial conditions it is easy to compute the bang time of the background and the perturbed sphere and one can solve for the pair $(\delta_i, \delta_{v,i})$ for which the bang times are equal. It turns out that for a $\Omega_m = 1$ cosmology, the pair $(\delta_i, \delta_{v,i})$ is independent of the initial starting time t_i and the Zeldovich curve is same for all epochs. However, for universes with non-zero dark energy, the values of $\Omega_{m,i}$ and $\Omega_{d.e,i}$ change and the Zeldovich curve depends on the starting epoch (see Appendix C.1).

Figure 5.1 shows the Zeldovich curves for different cosmologies for different starting redshifts. The red (dotted), blue (dashed), green (dotdashed) and brown (plain) represent four cosmologies with equation of state parameters $w = -1, -3/4, -2/3, -1/2$ respectively. They all have the same values of Ω_m and $\Omega_{d.e}$ today. The thick black line is the curve for $\Omega_m = 1$ cosmology. The differences between the evolution of the Zeldovich curve for change in the equation of states is due to the differences in the variation of Ω_m. As expected, for high redshift, the curves coincide since $\Omega_{m,i}$ term in eq. (5.2) dominates and is close to 1 for all cosmologies. Similarly, at $z = 0$ $(a_0 = 1)$, the density parameters for all dark energy cosmologies are the same and the curves match but deviate from the EdS value since $\Omega_{m,0} < 1$. As a measure of the deviation between two curves, we compute the differences between the value of δ_v at a fixed value of δ. For a fixed redshift, it is clear that higher the δ larger is the deviation. To estimate the deviation across redshifts, we measure the differences at $\delta = 2$ and find that the deviations between the $w = -1$ case and $w = -1/2$ case are maximum around a redshift of $z \sim 1$. This corresponds to the redshift where the differences in Ω_m between the two cosmologies are maximum.

Usually the density velocity relationship in linear Eulerian perturbation theory is characterized as $\nabla \cdot \mathbf{v} = -f(\Omega_m)\delta$, which in our notation reduces to $\delta_v = -f(\Omega_m)\delta/3$, where $f(\Omega_m)$ is the linear growth rate. The slope of the curve in phase space thus gives the *instantaneous* growth rate of the perturbations; a shallower curve implying a smaller Ω_m and slower growth rate. The overall rate at which perturbations grow is related to the speed at which they move along the curve and the net growth of perturbations in various cosmologies cannot be estimated by a phase space plot for a single redshift, but by comparison between two redshifts. This is why although the various dark energy curves are degenerate at $z = 0$, the net growth in these cosmologies can only be inferred by where perturbations that started at an earlier redshift lie along the curve. Figure 5.2 shows the evolution of a spherical compensated smooth overdensity for two of the cosmologies ($w = -1, w = -1/2$). The initial conditions were set at $z = 0.001$ and evolved until $z = 1$. It is apparent that the growth in the $w = -1$ cosmology is faster than that in the $w = -1/2$ cosmology. In the absence of any interactions, the evolution of a sphere is expected to follow the Zeldovich curve and this is seen qualitatively in the figure. A more quantitative assessment is yet to be done.

The study of the density-velocity relationship has been an area of active research for more than four decades. Early work by Peebles [63] estimated the linear growth rate in pure matter universes to be $f(\Omega_m) = \Omega_m^{0.6}$. This was later extended by Lahav *et al* [44] to cosmologies with a cosmological constant. Further extensions to quasi-linear/non-linear regimes were performed by Bernardeau [10] (B92) using second order Eulerian perturbation theory and more recently using the spherical-top hat model by Bilicki and Chodorowski [12] (BC08), although their analysis was restricted to a pure matter universe. Figure 5.3 compares these various approximations with the exact curve based on

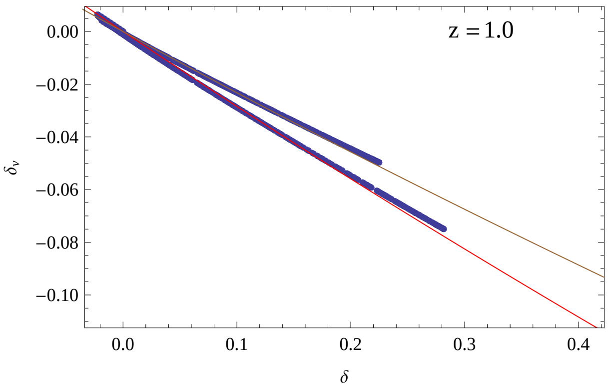

Figure 5.2: Evolution of the same compensated spherical overdensity in two different cosmologies. The initial conditions are the same for both cosmologies at $z = 0.001$ and are compared at $z = 1$. Evolution was carried out using first order LPT. The red curve corresponds to $w = -1$ and brown corresponds to $w = -1/2$. The growth in $w = -1/2$ cosmology is less than that in the $w = -1$ cosmology as seen by the dots on each curve. This is because dark energy starts to dominate earlier in the $w = -1/2$ case.

the spherical top-hat at the present epoch ($\Omega_m = 0.3, \Omega_{de} = 0.7$). The left and right panels focus on overdensities and underdensities respectively. The non-linear approximations by B92 and BC08 are within a few percent of the exact value for overdensities, however, the approximation by BC08 deviates significantly near $\delta \sim -1$.

5.3 Conclusion

This chapter presents preliminary results that indicate that phase space dynamics in the density-velocity plane can be a useful probe to constrain the dark energy equation of state. The Zeldovich curve based on the spherical top-hat system has been characterized for various dark energy equation of state parameters. Future work will indicate if there is a range of scales and

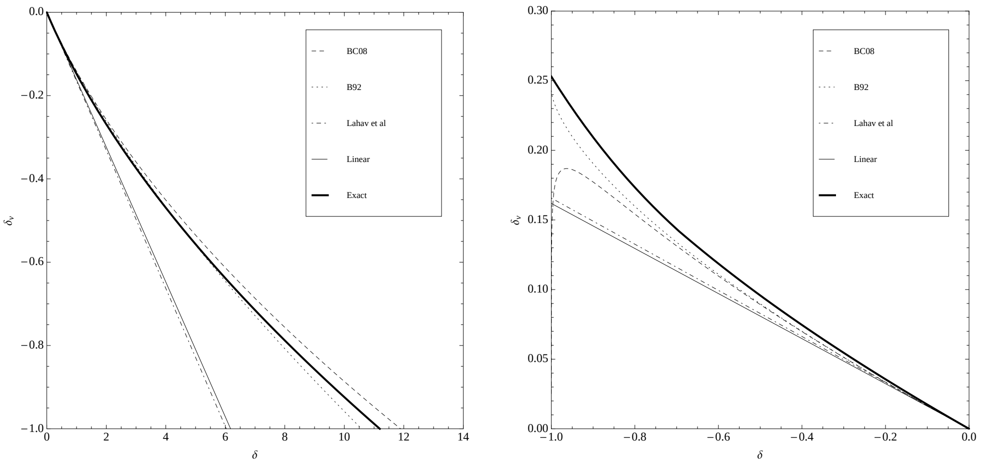

Figure 5.3: Comparison of the various approximations of the density-velocity relationship in literature. The left and right panels show the relationship for overdensities and voids respectively. The method presented in the paper provides an exact computation of the relationship based on the spherical top hat for any cosmology and any density. The non-linear approximations by B92 and BC08 agree for overdensities, but BC08 does not agree for $\delta \sim -1$.

redshifts where the effect of tidal forces can be disentangled from the effect of a background cosmology. If such a range exists and is not too sensitive to the underlying phenomenological model, then it can help design future surveys which aim to constrain the dark energy equation of state.

CHAPTER 6

CONCLUSION

This thesis has investigated the convergence properties of Lagrangian Perturbation Theory and developed the method of Lagrangian re-expansions to improve convergence. The method is capable of non-linear evolution of general initial conditions, including those arising from a random Gaussian field and I have numerically implemented the scheme and tested it. A scheme based on LPT has the advantage that it can efficiently evolve smooth initial conditions from as early as recombination because it is not limited by N-body like shot noise. By specifying the number of steps and order of the scheme, one can fine tune it to achieve any desired accuracy. However, like a numerical simulation, the box size and the grid size set the upper and lower limits on the scales that can be modeled by this scheme and any errors due to effect of scales outside the box will remain present.

The generality of this tool makes it very useful for a variety of applications which were listed in the introduction. Currently, the code has been developed and tested using *Mathematica* [83]. The algorithm that re-initializes the system is the most memory intensive step that prevents bigger grids from being implemented in the *Mathematica* version. A C-based version of the code is under development. This will enable simulations of bigger boxes with larger grids that would be most useful to a cosmological application. In the near future I plan to use this scheme to solve some of the problems that I have outlined in the introduction.

APPENDIX A

APPENDIX FOR CHAPTER 3

A.1 Formal set-up of the spherical top-hat

We intend to study an inhomogeneous universe. It contains a single, compensated spherical perturbation evolving in a background cosmology. To describe two spatially distinct pieces of the inhomogeneous universe (the background and the central perturbation) we invoke the language of homogeneous cosmology.

A.1.1 Description of the background

The origin of the coordinate system is the centre of the sphere. The background system at the initial time t_0 is set by the physical size of the inner edge $r_{b,0}$, the velocity $\dot{r}_{b,0}$ and density parameter Ω_0. The Lagrangian coordinate system is extended linearly throughout space once the Lagrangian coordinate of the inner edge is fixed. Let the Lagrangian coordinate of the inner edge be

$$Y = \frac{r_{b,0}}{a_0}. \tag{A.1}$$

Either choose the initial background scale factor a_0 and determine the coordinate system or, alternatively, fix Y and infer the background scale factor. In either case, the scale factor embodies the gauge freedom associated with the radial coordinate system.

The future evolution of the inner edge of the background is given by $r_b(t) = a(t)Y$. The velocity at the initial time satisfies $\dot{r}_{b,0} = \dot{a}_0 Y$. The density at any later time is

$$\rho_b(t) = \frac{\rho_{b0} a_0^3}{a^3}, \tag{A.2}$$

and the Hubble parameter for the background is

$$H_0 = \frac{\dot{r}_{b,0}}{r_{b,0}} = \frac{\dot{a}_0}{a_0}. \tag{A.3}$$

The evolution of the scale factor is

$$\frac{\ddot{a}}{a} = -\frac{4\pi G \rho_{b0} a_0^3}{a^3} = -\frac{1}{2} \frac{H_0^2 a_0^3 \Omega_0}{a^3}. \tag{A.4}$$

The quantities, $r_{b,0}$, $\dot{r}_{b,0}$, Ω_0 and t_0 along with the choice of the coordinate system, completely specify the background universe.

A.1.2 Description of the innermost perturbation

The perturbation can be described by four physical quantities: the physical position $r_{p,0}$ and velocity $\dot{r}_{p,0}$ of the edge (or the ratio $H_{0p} = \dot{r}_{p,0}/r_{p,0}$), the density parameter Ω_{p0} at the initial time t_0. The Lagrangian coordinate system for the perturbation is

$$X = \frac{r_{p,0}}{b(t_0)}. \tag{A.5}$$

It can be linearly extended throughout space.

Like a_0, $b(t_0)$ embodies the gauge freedom associated with the choice of the coordinate system. Without loss of generality, one can pick this gauge to satisfy

$$b(t_0) = a_0. \tag{A.6}$$

Note that the Lagrangian coordinate systems for the background and perturbation are different.

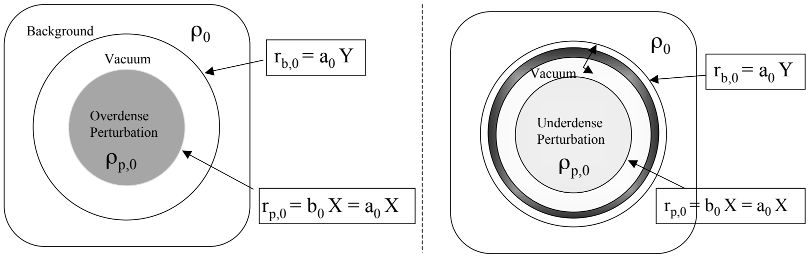

Figure A.1: A cartoon showing the physical set-up of the problem.

Let ρ_0 and $\rho_{p,0}$ denote the densities of the background and perturbation respectively. Define the perturbation parameters

$$\delta = \frac{\rho_{p0}}{\rho_{b0}} - 1 \tag{A.7}$$

$$\delta_v = \frac{H_{0p}}{H_0} - 1 \tag{A.8}$$

giving

$$\Omega_{0p} = \frac{(1+\delta)}{(1+\delta_v)^2}. \tag{A.9}$$

A.1.3 Inhomogeneous model

Figure A.1 shows how an overdense and underdense innermost sphere may be embedded with compensation in a homogeneous background universe. The assumption that the background cosmology evolves like a homogeneous model, fully described in terms of its Hubble constant and density, imposes consistency conditions. At the initial instant the "inner edge" of the unperturbed background distribution is at physical distance $r_{b,0}$ from the centre of the sphere. The region with $r > r_{b,0}$ will evolve like an unperturbed homogeneous cosmology as long as

1. the mass within equals the mass that an unperturbed sphere would contain;
2. matter motions within the perturbed region do not overtake the inner edge of the homogeneous region.

These conditions which are obvious in the Newtonian context have general relativistic analogues (Landau & Lifschitz [45]).

Next, consider the innermost perturbed spherical region. At the initial time let $r_{p,0}$ be the "outer edge" of this region. The physical properties and evolution of the innermost region are fully described in terms of its Hubble constant and density as long as its outer edge does not overtake matter in surrounding shells. While this is obvious in a Newtonian context there exists a relativistic analogue (Tolman [78]; Landau & Lifschitz [45]).

The inhomogeneous model is incomplete without specification of the transition region between the innermost sphere and the background. For the background to evolve in an unperturbed fashion the mass within $r_{b,0}$ must be exactly $4\pi\rho_0 r_{b,0}^3/3$. There are many ways to satisfy this requirement. For example, when $\delta > 0$ a simple choice is to place an empty (vacuum) shell for $r_{p,0} < r < r_{b,0}$ so that $(\rho_{p0}/\rho_0) = (r_{b,0}/r_{p,0})^3 = (Y/X)^3$. The evolution of each matter-filled region proceeds independently as long as the trajectories of the inner and outer edges do not cross. When $\delta < 0$, a more complicated transition is required. For example, one choice is to nest sphere, empty shell and dense shell (see figure A.1) so that the mass within $r_{b,0}$ matches that of the unperturbed background. In this case $\rho_{p0} r_{p,0}^3 = f \rho_0 r_{b,0}^3$ for some $f < 1$ (the remaining fraction $1 - f$ is placed in the dense shell). Varying the specifics of the compensation region while keeping the properties of the sphere fixed leaves δ and δ_v, as defined above, invariant.

For fixed δ and δ_v the solution $b(t)$ is independent of the details of the transition. Nonetheless, variation in f, $r_{b,0}/r_{p,0}$ and Y/X all go hand-in-hand. Hence, the extent of time that the sphere's evolution may be treated as independent of the matter-filled outer regions also varies. A basic premise of this paper is that it is meaningful to determine the limitations arising from the convergence of the LPT series independently of limitations associated with crossing of separate matter-filled regions. For a given a δ and δ_v this separation can be achieved for specific constructions by choosing the radius and (hence velocity) of the inner sphere and the energy of the compensating region appropriately.

A.1.4 Number of degrees of freedom for the innermost sphere

If the innermost sphere corresponds to an overdensity then the compensating region can be a vacuum as shown in figure A.1. Having picked the co-ordinate system, having selected equal initial times for the background and perturbation (not equal bang times but equal times at which we give the background and perturbation values), and required the correct amount of mass, only two degrees of freedom remain: δ and δ_v.

To reiterate, the background and the perturbation can have different big bang times. Setting them equal would imply a relationship between δ and δ_v and leave a single free parameter.

If the innermost sphere corresponds to an underdensity then the compensating region is not vacuum but a spherical shell. In this case, in addition to δ and δ_v, one must specify f or, equivalently, $r_{p,0}$. But the solution for $b(t)$ is independent of the size of the innermost sphere so, again, only two degrees of freedom remain.

A.1.5 Preventing shell crossing

There are two sorts of limitations for the solution of $b(t)$. One is the calculation-dependent limitation arising from the convergence properties of the Lagrangian series expansion. It involves the scale factors only. The other is a physical limitation arising from collisions of the innermost region with surrounding non-vacuum regions (either the background or a compensating shell). We show that it is possible to delay the epoch of collisions indefinitely without altering the evolution of the innermost region.

Fix H_0, $H_{p,0}$, ρ_0 and $\rho_{p,0}$. This implies that the expansion parameters in LPT, δ and δ_v, and the time of validity of the LPT solution are all fixed. Consider the case of an overdensity surrounded by vacuum. To stave off the collision of the outer edge of the innermost region with inner edge of the homogeneous background hold $r_{b,0}$ fixed and reduce $r_{p,0}$. The velocity $\dot{r}_{p,0} = H_{0p} r_{p,0}$ becomes arbitrarily small. The time for the edge to reach any fixed physical distance increases without bound. Shell crossings may be put off indefinitely. However, we have altered the mass within the innermost edge of the background so we add back a thin, dense shell just inside $r_{b,0}$ and set it on a critical trajectory outward. This accomplishes our goal.

The case of the underdensity surrounded by a compensating shell is identical. First, we must make sure that the compensating shell does not overrun the homogeneous model. Choose the shell to be thin, fix its initial physical distance from the centre and adjust is velocity (based on how the interior mass changes) to give a critical solution. The two power laws, one for the compensating shell and one for the innermost boundary of the homogeneous model, cannot cross in the future. Second, as above, note that reducing $r_{p,0}$ reduces the outward velocity of the edge so that it takes more time to reach the initial position of the compensating shell. The time can be made arbitrarily long.

The limitations in LPT convergence are completely distinct from those associated with physical collisions in inhomogeneous model.

A.2 Series expansions for a function of two variables

In this section we elucidate by example some qualitative features of the expansion of $b(t, \Delta)$, the central quantity in the Lagrangian treatment of the top-hat. We assume a very simple form denoted $f(t, \Delta)$ and look at convergence with respect to expansions in t and Δ. Let

$$f(t, \Delta) = t^{2/3} \left(\frac{1}{t} + \Delta \right)^{1/3} . \tag{A.10}$$

The series expansion of this function around $\Delta = 0$ at fixed t is

$$f \sim t^{1/3} + t^{4/3}\Delta - \frac{1}{9}t^{7/3}\Delta^2 + \frac{5}{81}t^{10/3}\Delta^3 - \frac{10}{243}t^{13/3}\Delta^4 + \frac{22}{729}t^{16/3}\Delta^5 + O(\Delta^6) \tag{A.11}$$

which is supposed to mimic the Lagrangian expansion in Δ. One can also expand the function as a series in t around $t = t_i$

$$\begin{aligned} f \quad &\sim \quad \sqrt[3]{\Delta + \frac{1}{t_i}}\,t_i^{2/3} + \frac{(2\Delta t_i + 1)(t - t_i)}{3\left(\Delta + \frac{1}{t_i}\right)^{2/3} t_i^{4/3}} + \frac{\left(-\Delta^2 t_i^2 - \Delta t_i - 1\right)(t - t_i)^2}{9\left(\Delta + \frac{1}{t_i}\right)^{2/3} t_i^{7/3}(\Delta t_i + 1)} \\ &\quad + \frac{\left(4\Delta^3 t_i^3 + 6\Delta^2 t_i^2 + 12\Delta t_i + 5\right)(t - t_i)^3}{81\left(\Delta + \frac{1}{t_i}\right)^{2/3} t_i^{10/3}(\Delta t_i + 1)^2} + O\left((t - t_i)^4\right). \end{aligned} \tag{A.12}$$

Both expansions involve the complex power $z^{1/3}$. There are two branch cuts which extend to $z = 0$ so at $\Delta = -1/t$ the function is not analytic. Additionally, the expansion in t is not analytic at $t = 0$.

The efficacy of various expansions are illustrated in figure A.2. In all the plots the black dotted line indicates the exact function. The top left panel shows successively higher order series approximations in Δ as a function of t for the specific case $\Delta = 1/10$. The question here is whether the pole at a given time lies with a disk of radius $1/10$? The location of the pole is $\Delta = -1/t$ so the answer is "yes" when $t > 10$. This pole interferes with the convergence of the series expansion for $\Delta = 1/10$. The figure demonstrates the (future) time of validity is $t < 10$.

The top right panel shows the series in Δ at a fixed $t = 1/10$. The question here is how big a perturbation will converge at $t = 1/10$? Since the location of the pole is $\Delta = -1/t$ the radius of convergence at the indicated time is 10. Perturbations with $|\Delta| > 10$ are not expected to converge and the figure shows that this is indeed the case.

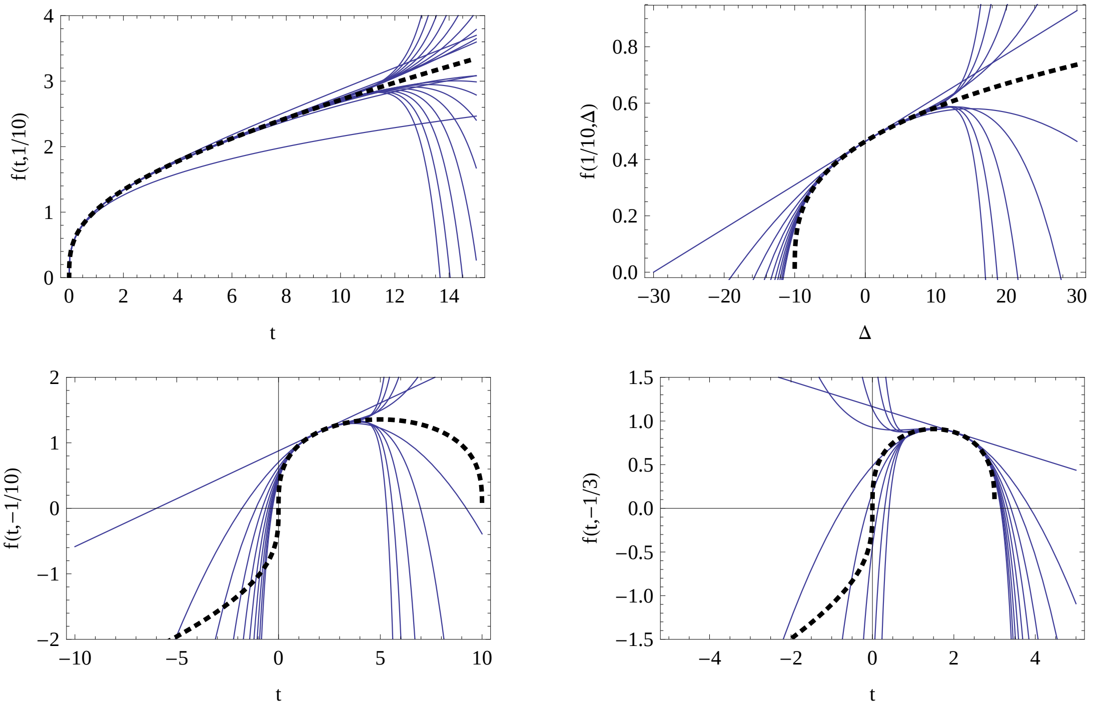

Figure A.2: Series expansions in t and Δ for an illustrative function $f(t, \Delta)$ (see text). The black dotted line indicates the exact function f and the blue solid lines indicate successive approximations. The top left and right panels are series expansions in Δ around $\Delta = 0$ plotted as a function of t (for $\Delta = 1/10$) and function of Δ (for $t = 1/10$) respectively. The bottom left and right panels are series expansions in the t around $t = 2$ plotted as functions of t for $\Delta = -1/10$ and $\Delta = -1/3$ respectively.

The bottom left panel shows the series in t expanded around $t_i = 2$ for fixed $\Delta = 1/10$. The poles are at $t = -10$ and $t = 0$ in the complex t plane. The expected radius of convergence is $\min(|2 - 0|, |2 - (-10)|) = 2$ or $t_i - 2 < t < t_i + 2$. As seen in the plot, the series converges only in the expected range $(0, 4)$

The bottom right panel shows the series in t expanded around $t_i = 2$ for $\Delta = -1/3$. The poles are at $t = 3$ and $t = 0$ in the complex t plane. The expected radius of convergence is $\min(|2 - 0|, |2 - 3|) = 1$ or $t_i - 1 < t < t_i + 1$. As seen in the plot, the series converges only in the expected range $(1, 3)$.

A.3 Parametric Solution

The background model has scale factor a_0 and Hubble constant $H_0 = \dot{a}_0/a_0$. The model, perturbed in density and velocity, is parameterized by Δ and θ and has scale factor $b(t)$. For the choice of coordinate system given in the text the second order equation for b is

$$\frac{\ddot{b}}{b} = -\frac{1}{2}\frac{H_0^2 a_0^3(1 + \Delta\cos\theta)}{b^3} \tag{A.13}$$

with the initial conditions that at $t = t_0$, $b(t_0) = a_0$, $\dot{b}(t_0) = \dot{a}_0(1 + \Delta\sin\theta)$. The scale factor a_0 and the velocity of the background $\dot{a}_0$ at the initial time t_0 are positive. The parametrization of $\dot{b}(t_0)$ allows either positive or negative values where Δ is non-negative and $-\pi < \theta \leq \pi$. The quantity $(1 + \Delta\cos\theta)$, proportional to total density, is non negative.

This equation once integrated is

$$\dot{b}^2 = H_0^2 a_0^3\left[\frac{(1 + \Delta\cos\theta)}{b} + \frac{(1 + \Delta\sin\theta)^2 - (1 + \Delta\cos\theta)}{a_0}\right]. \tag{A.14}$$

The combination

$$E(\Delta, \theta) = (1 + \Delta\sin\theta)^2 - (1 + \Delta\cos\theta) \tag{A.15}$$

is proportional to the total energy and determines the fate of the system. If $E(\Delta, \theta) > 0$, the model is open and if $E(\Delta, \theta) < 0$, the model is closed and will recollapse eventually. Four cases (positive and negative E, positive and negative $\dot{b}_0$) are shown in figure 3.5.

A.3.1 Initially Expanding Solutions

The expanding case with $\dot{b}_0 > 0$ for open models ($E > 0$) has solution

$$\begin{aligned} b(\eta, \Delta, \theta) &= \frac{a_0}{2} \frac{(1 + \Delta \cos\theta)}{E(\Delta, \theta)} (\cosh\eta - 1) && \text{(A.16)} \\ t(\eta, \Delta, \theta) &= \frac{1}{2H_0} \frac{(1 + \Delta \cos\theta)}{E(\Delta, \theta)^{3/2}} (\sinh\eta - \eta) + t^{+}_{bang}(\Delta, \theta) && \text{(A.17)} \end{aligned}$$

and the singularity $b = 0$ occurs at $\eta = 0$. For closed models ($E < 0$) the solution is

$$\begin{aligned} b(\eta, \Delta, \theta) &= \frac{a_0}{2} \frac{(1 + \Delta \cos\theta)}{|E(\Delta, \theta)|} (1 - \cos\eta) && \text{(A.18)} \\ t(\eta, \Delta, \theta) &= \frac{1}{2H_0} \frac{(1 + \Delta \cos\theta)}{|E(\Delta, \theta)|^{3/2}} (\eta - \sin\eta) + t^{+}_{bang}(\Delta, \theta). && \text{(A.19)} \end{aligned}$$

For closed models, the convention adopted sets $\eta = 0$ at the singularity nearest in time to t_0. For both models, the time at $\eta = 0$ is denoted t^{+}_{bang}. For closed models the time at $\eta = 2\pi$ is denoted t^{+}_{coll}.

At the initial time the solutions (both open and closed) satisfy $b(t_0) = a_0$, $\dot{b}(t_0) = \dot{a}_0(1 + \Delta \sin\theta)$ and $t = t_0$. The condition $b(t_0) = a_0$ sets the value of the parameter at the initial time η_0. The velocity condition is then manifestly satisfied from the form of eq. (A.14). The condition $t = t_0$ at $\eta = \eta_0$ sets the value of the bang time

$$t^{+}_{bang} = t_0 - \begin{cases} \frac{1}{2H_0} \frac{(1+\Delta\cos\theta)}{|E(\Delta,\theta)|^{3/2}} (\eta_0 - \sin\eta_0) & E < 0 \\ \frac{1}{2H_0} \frac{(1+\Delta\cos\theta)}{E(\Delta,\theta)^{3/2}} (\sinh\eta_0 - \eta_0) & E > 0. \end{cases} \tag{A.20}$$

The bang time for the model can also be written as

$$t^{+}_{bang} = t_0 - \int_{b=0}^{b=a_0} \frac{db}{(\dot{b}^2)^{(1/2)}}, \tag{A.21}$$

where $\dot{b}^2$ is given by eq. (A.14) with the sign for the square root positive. The age of the model since its birth is

$$t_{age}(\Delta, \theta) = \int_{b=0}^{b=a_0} \frac{db}{(\dot{b}^2)^{(1/2)}} = \int_{\eta=0}^{\eta=\eta_0} \frac{db/d\eta \cdot d\eta}{(\dot{b}^2(\eta))^{(1/2)}}. \tag{A.22}$$

Inserting the appropriate parametric solution, one can verify that the bang times obtained from (A.20) and (A.21) are identical. Generally $t^{+}_{bang} \neq 0$.

The velocity at the initial time is

$$\dot{b}_0 = \dot{a}_0 |E|^{1/2} \begin{cases} \frac{\sin \eta_0}{1-\cos \eta_0} & E < 0 \\ \frac{\sinh \eta_0}{\cosh \eta_0 - 1} & E > 0. \end{cases} \tag{A.23}$$

First, $\dot{b}_0 > 0$ implies $\eta_0 > 0$. Second, if the age of the model increases, η increases. For the open solution if η varies from 0 to ∞ time increases from t^{+}_{bang} to ∞. For a single cycle of the closed solutions, η increases from 0 to 2π and time increases from t^{+}_{bang} to t^{+}_{coll}.

In summary, the parametric solutions solve eq. (A.13) and eq. (A.14) for the specified initial conditions. As a final useful step, rewrite eq. (A.21) by defining $y = b/a_0$

$$t^{+}_{bang} = t_0 - \frac{1}{H_0} \int_{y=0}^{y=1} \frac{dy}{\left[(1 + \Delta \cos \theta) y^{-1} + E(\Delta, \theta)\right]^{1/2}} \tag{A.24}$$

which follows from eq. (A.14) and uses the same positive square root convention.

A.3.2 Initially Contracting Solutions

Next, consider the case $\dot{b}_0 < 0$. The parametric solution for $E > 0$ is

$$b(\eta, \Delta, \theta) = \frac{a_0}{2} \frac{(1 + \Delta \cos \theta)}{E(\Delta, \theta)} (\cosh \eta - 1) \tag{A.25}$$

$$t(\eta, \Delta, \theta) = \frac{1}{2H_0} \frac{(1 + \Delta \cos \theta)}{E(\Delta, \theta)^{3/2}} (-\sinh \eta + \eta) + t^{-}_{bang}(\Delta, \theta) \tag{A.26}$$

and for $E < 0$ is

$$b(\eta, \Delta, \theta) = \frac{a_0}{2} \frac{(1 + \Delta \cos \theta)}{|E(\Delta, \theta)|} (1 - \cos \eta) \tag{A.27}$$

$$t(\eta,\Delta,\theta) \;=\; \frac{1}{2H_0}\frac{(1+\Delta\cos\theta)}{|E(\Delta,\theta)|^{3/2}}(-\eta+\sin\eta)+t^{-}_{bang}(\Delta,\theta). \tag{A.28}$$

Again, for closed models, the convention adopted is that the singularity nearest to t_0 corresponds to $\eta = 0$. The time at $\eta = 0$ is t^{-}_{bang} and the collapse time for closed models is t^{-}_{coll}.

The parametric form of the solutions satisfies eq. (A.13) and eq. (A.14). Just as in the previous case, the initial conditions set η_0 and t^{-}_{bang}. Since the singularity at $\eta = 0$ lies to the future of t_0,

$$t^{-}_{bang} = t_0 + \int_{b=0}^{b=a_0} \frac{db}{(\dot{b}^2)^{(1/2)}}. \tag{A.29}$$

where $\dot{b}^2$ is given by eq. (A.14). The sign of the square root is chosen to be positive and the integral is a positive quantity which is added to t_0. For closed models the singularity at $\eta = 2\pi$ lies to the past of t_0 at t^{-}_{coll}. In this case (see figure 3.5) the labeling implies $t^{-}_{coll} < t_0 < t^{-}_{bang}$. Although this might seem backwards, it facilitates combining the open and closed models into one complex function as was done in the positive $\dot{b}_0$ case. The initial velocity is

$$\dot{b}_0 = \dot{a}_0|E|^{1/2}\begin{cases} \frac{\sinh\eta_0}{1-\cosh\eta_0} & E > 0 \\ \frac{\sin\eta_0}{\cos\eta_0-1} & E < 0 \end{cases} \tag{A.30}$$

The initial velocity $\dot{b}_0 < 0$ implies $\eta_0 > 0$. For the age of the model to increase, η must decrease. Conversely, if η increases, the time in the open model decreases from t_0 to $-\infty$ and the time in the closed model decreases from t_0 to t^{-}_{coll}.

A table summarizing the properties of the physical solutions with $\eta = |\eta|\zeta = \eta\zeta$ follows.

	Closed	Open	If η increases	If t increases	$t_{bang} - t_0$
$\dot{b}_0 > 0$	$\zeta = 1$	$\zeta = i$	t increases from t^+_{bang}	η increases to ∞ or 2π	< 0
$\dot{b}_0 < 0$	$\zeta = 1$	$\zeta = i$	t decreases from t^-_{bang}	η decreases to 0	> 0

A.3.3 Analytic Extension of the exact solution in parametric form

The differential eq. (3.32) was solved numerically over the range $0 \leq \theta \leq \pi$, $0 < \delta < 100$ and $-\pi < \phi \leq \pi$ where $\mathbf{\Delta} = \Delta e^{i\phi}$. For each value of (Δ, ϕ, θ), the numerical solution matched one of the two possible parametric forms.

Omitting the explicit functional dependence on $\mathbf{\Delta}$ and θ the following abbreviations are useful

$$\begin{aligned} \mathbf{j} &= (1 + \mathbf{\Delta} \cos\theta) && \text{(A.31)} \\ \mathbf{h} &= \frac{(1 + \mathbf{\Delta} \sin\theta)^2}{\mathbf{j}} && \text{(A.32)} \\ \mathbf{E} &= (\mathbf{h} - 1)\mathbf{j}. && \text{(A.33)} \end{aligned}$$

The two possible parametric forms that agree with the numerical solution are

$$\begin{aligned} \mathbf{b}(\eta) &= \frac{a_0}{2} \frac{\mathbf{j}}{[-\mathbf{E}]}(1 - \cos\eta) && \text{(A.34)} \\ \mathbf{t}(\eta) &= t_0 \pm \left(\frac{1}{2H_0} \frac{\mathbf{j}}{[-\mathbf{E}]^{3/2}}(\eta - \sin\eta) - \mathbf{t_{age}} \right) && \text{(A.35)} \end{aligned}$$

where

$$\mathbf{t_{age}} = \frac{1}{H_0} \left(\sqrt{\mathbf{j}}\sqrt{\mathbf{h}} - \frac{\mathbf{j}}{[\mathbf{E}]^{3/2}} \sinh^{-1} \sqrt{\frac{\mathbf{E}}{\mathbf{j}}} \right). \qquad \text{(A.36)}$$

The branch cut lies along the negative real axis for all fractional powers and from $-i\infty$ to $-i$ and $+i$ to $i\infty$ for the inverse sinh function.

The prescription for the correct form is for the choice of the ± sign in $\mathbf{t}$ eq. (A.35) and denoted $\mathbf{t}_+$ and $\mathbf{t}_-$. The correct form depends upon θ, ϕ, $\arg[\mathbf{h}]$ (the arg is defined to be between $-\pi$ and π) and the (real) value $j = \mathbf{j}$ when $\phi = 0$ or π. The figure A.3 shows the upper half plane for the perturbation partitioned into areas where the complex extension of the solution has one of two forms. The lower half plane has the same structure inverted through the origin. The horizontal red dashed line denotes $\Delta \sin\theta = 1$ and the vertical red dashed lines denote $\Delta \cos\theta = \pm 1$. In some areas a single form applies as marked but in the central area both occur. The detailed prescription is

$$\mathbf{t} = \begin{cases} 0 \le \theta \le \pi/4 & \begin{cases} \phi = \pi, |\Delta| \sin\theta < 1 \text{ and } j < 0 & \mathbf{t}_- \\ \text{otherwise} & \mathbf{t}_+ \end{cases} \\ \pi/4 < \theta \le \pi & \begin{cases} 0 < \phi < \pi \text{ and } \arg \mathbf{h} > 0 & \mathbf{t}_+ \\ -\pi < \phi < 0 \text{ and } \arg \mathbf{h} < 0 & \mathbf{t}_+ \\ \phi = 0 \text{ and } \begin{cases} \cos\theta > 0 \\ \text{or} \\ \cos\theta < 0 \text{ and } j > 0 \end{cases} & \mathbf{t}_+ \\ \phi = \pi \text{ and } \begin{cases} \cos\theta < 0 \\ \text{or} \\ \cos\theta > 0 \text{ and } j < 0 \end{cases} & \mathbf{t}_- \\ \text{otherwise} & \mathbf{t}_- \end{cases} \end{cases} \tag{A.37}$$

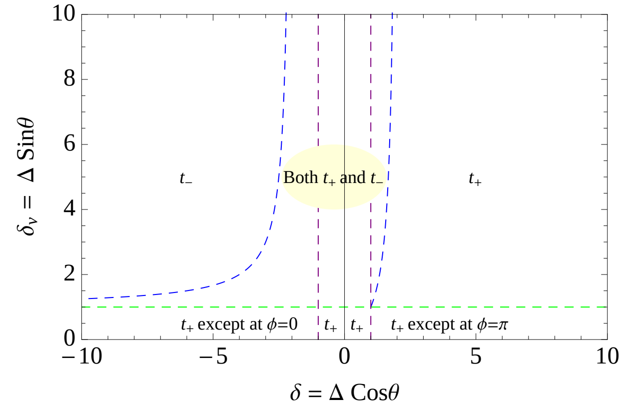

Figure A.3: This figure describes one aspect of the analytic extension of the exact solution. For a given real Δ, the complex extension $\Delta \to \Delta e^{i\phi}$ obeys eq. (A.37) with two possible forms $\mathbf{t}_+$ and $\mathbf{t}_-$. The choice depends on ϕ, Δ, θ. For some (Δ, θ) a single form is sufficient for all ϕ; for other values both forms are needed. This figure illustrates how the upper half plane is partitioned based on this property.

A.4 Numerical solutions

A.4.1 Algorithm

The initial conditions are parameterized by $\Delta > 0$ and $-\pi < \theta \leq \pi$. The transformation $\theta \to \pi \pm \theta$ and $\Delta \to -\Delta$ leaves the solution unchanged. At any time the roots for θ and $\pi \pm \theta$ are negatives of each other. The root plot only depends upon the absolute value of the root so the plots for θ and $\pi \pm \theta$ are identical. It is sufficient to consider the upper half plane.

For a given θ the algorithm to map out $R_\Delta(t)$ is the following: Vary Δ from 0 to an arbitrarily large value (~ 100) in small increments. For each Δ select $\mathbf{\Delta} = \Delta e^{i\phi}$ by varying the phase angles ϕ over the range 0 to 2π. For each $\mathbf{\Delta}$ evaluate $\mathbf{t}(\eta)$ at $\eta = 0$ and $\eta = 2\pi$ calculated according to eq. (A.37). Finally, hunt for solutions that set the imaginary part of $\mathbf{t}$ to 0. This last step involves one-dimensional root-finding in ϕ at fixed Δ. A solution leads to a specific pair $(t, \mathbf{\Delta})$ that is a pole in the function $\mathbf{b}(\mathbf{\Delta}, t)$.

Roots with $t > t_0$ limit future evolution; those with $t < t_0$ limit backwards evolution. Both sets are shown in the results. Roots are classified based on whether they are real or complex. For closed models the real roots can represent a singularity that is nearby ($\eta = 0$) or far away ($\eta = 2\pi$) from t_0. This classification at the initial time is independent of whether the singularity is in the past or future and is independent of whether the model is expanding or contracting. For open models the real roots are always considered nearby ($\eta = 0$).

In what follows the numerical answers are first described in qualitative terms. In the next section simple analytic estimates for the time of validity are developed.

Figure A.4 shows the root plots on a log-log scale. Sixteen panels, each with a particular value of θ listed at the top, are displayed. The x-axis is $\log_{10} H_0 t$ and the y-axis is the log of the distance of the singularity from the origin in the complex $\mathbf{\Delta}$ plane. The initial time, $H_0 t_0 = 2/3$, is marked by the vertical black dashed line.

For each θ, the shaded region indicates the range of Δ that gives rise to closed models. Figure 3.2 shows that closed models occur only for $\theta < \theta_c^+ = 0.463$ in the upper half plane so only some of the root plots have shading and then only at smaller Δ.

The color coding of the dots indicates four types of roots: real and complex roots where $\eta = 2\pi$ are in blue and red, respectively; real and complex roots with $\eta = 0$ are in cyan and pink, respectively. The radius of convergence at the initial time t_0 is infinite, i.e. the Lagrangian series is exact at the initial time by construction. At times very close to the initial time the root loci lie off the plot. Only the roots to the right of $H_0 t_0$ are relevant for forward evolution and, conversely, only those to the left are relevant for backwards evolution. The discussion is focused on the case of forward evolution but it is straightforward to consider the restrictions on marching backwards in time.

The phase of the root (of smallest magnitude) appears in figure A.6. When closed models have real roots they are positive; when open models have real roots they are negative. However, some open and closed models also possess complex roots. The set of models with complex roots (of smallest magnitude) is evident from the shading in figure 3.10. The phase of each root of smallest magnitude in figure A.4 is indicated by the color shading in figure A.6.

There are horizontal dashed lines with colors green, blue and purple in figures A.4 and A.6 indicating $|\delta_v| = 1$, $|\delta| = 1$ and the transition between one and two complex forms, respectively. For each θ the lines mark the implied, special value of Δ. These dashed lines also appear with the same color coding in figure A.5.

The roots in figure A.4 will be analyzed in the range $0 < \theta \leq \pi/4$, $\pi/4 < \theta \leq \pi/2$, $\pi/2 < \theta \leq \pi$.

$0 \leq \theta \leq \pi/4$

The top left panel in figure A.4 has $\theta = 0$; the blue dots indicate real roots with $\eta = 2\pi$; the blue shading indicates a closed model; the phase is positive (top left

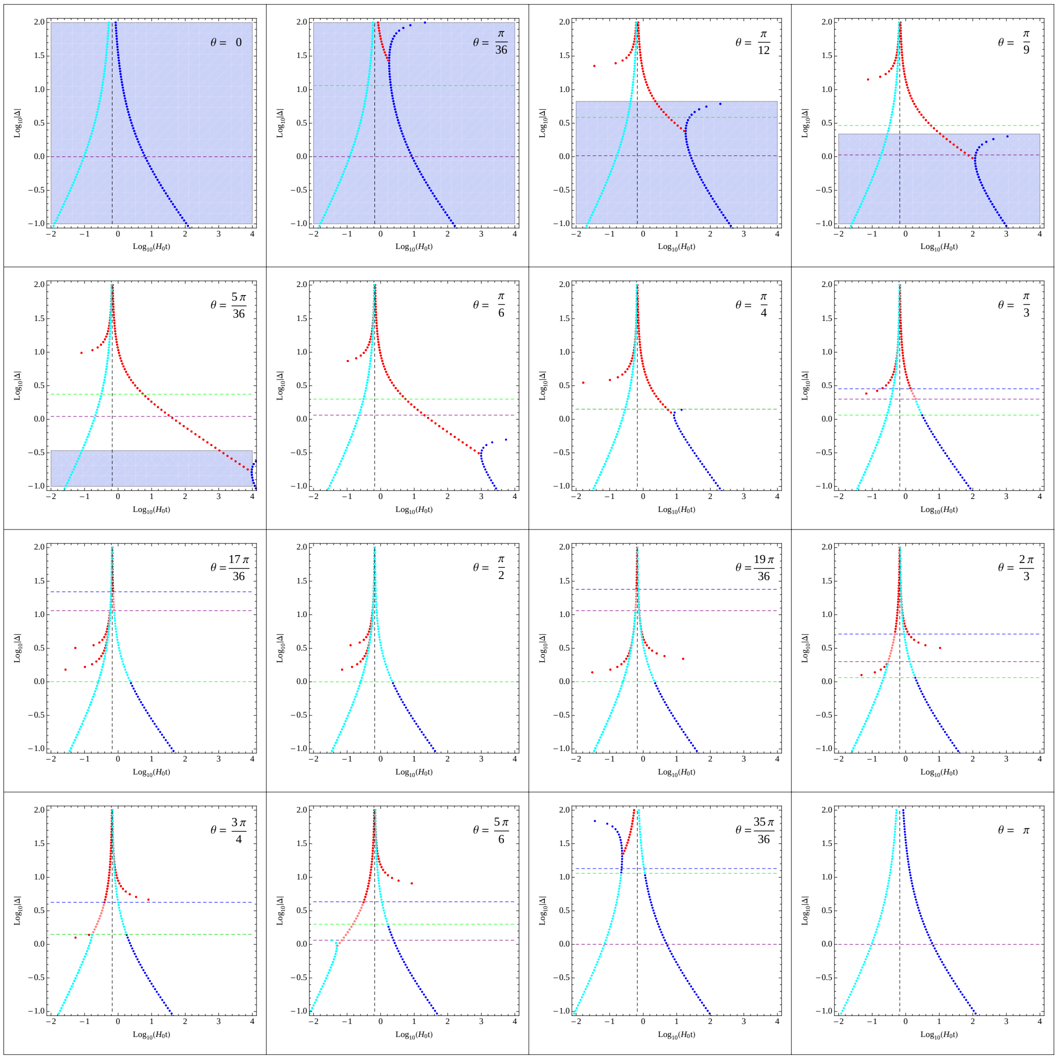

Figure A.4: Root plots for θ in the range $0 \leq \theta \leq \pi$. In each plot the abscissa is $\log_{10} H_0 t$ and the ordinate is the logarithm of the magnitude of the root. The vertical black dashed line marks the initial time. The shaded area corresponds to closed models. The blue and red points show real and complex roots with $\eta = 2\pi$, respectively. The cyan and pink show real and complex roots with $\eta = 0$, respectively. The green and purple dashed lines are $|\delta_v| = 1$ ($\Delta = |\sin\theta|^{-1}$) and $|\delta| = 1$ ($\Delta = |\cos\theta|^{-1}$), respectively. The blue dashed line indicates the switch between two forms and a single form of the parametric solution at $\Delta = |2\sec\theta - \csc\theta|$.

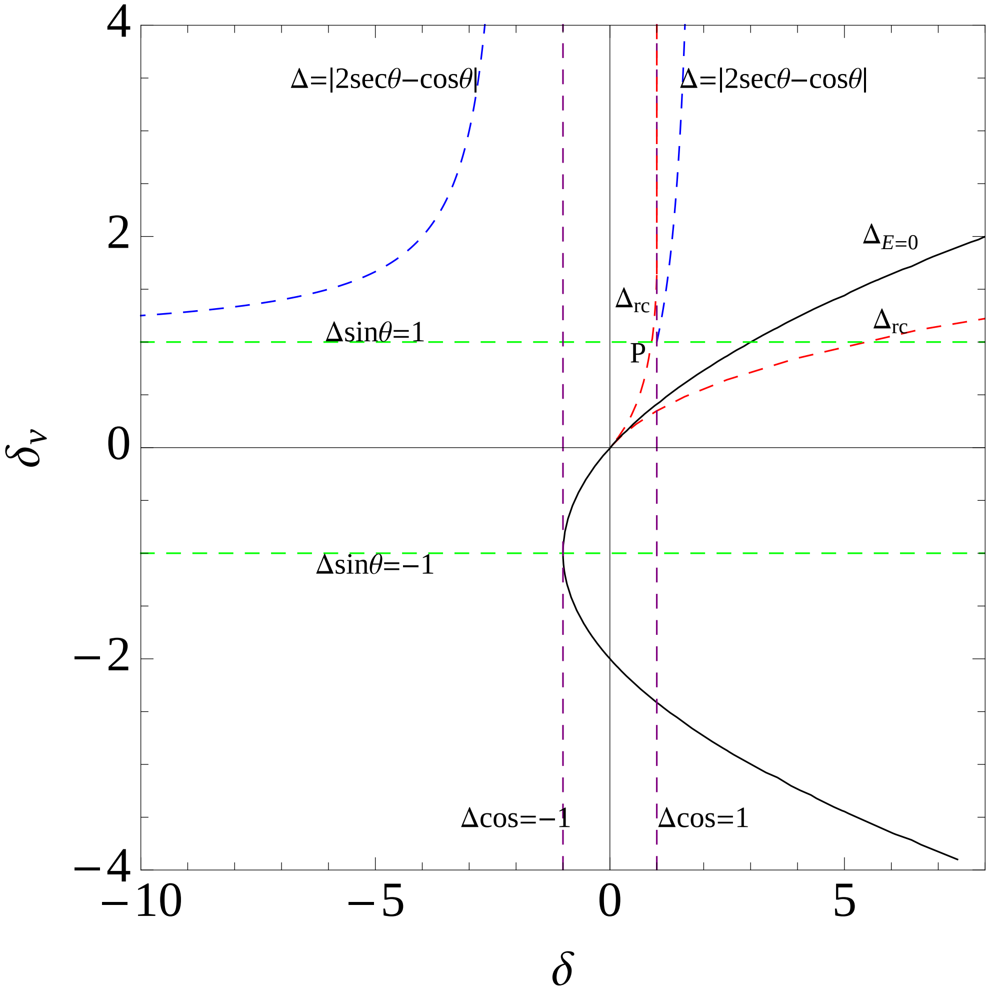

Figure A.5: Several conditions determine the nature of the roots in phase space. The most significant are schematically illustrated here. The green horizontal lines are $|\delta_v| = \Delta|\sin\theta| = 1$; purple vertical lines are $|\delta| = \Delta|\cos\theta| = 1$; the black curved line is the $E = 0$ critical solution. The red lines Δ_{rc} mark where real roots associated with closed models (or closed mirror models) transform to complex roots. The blue dashed lines mark the division between one and two complex forms (see also figure A.3). Physical models lie to the right of $\delta = -1$. Expanding models lie above $\delta_v = -1$. The intersection $\delta = \delta_v = 1$ occurs at $\theta = \pi/4$. The point P near $\theta = 0.84$ is the meeting of $\delta_v = 1$ and Δ_{rc}.

panel in figure A.6). Only a single branch is evident. In sum, each root is the collapse time of a closed, pure density perturbation. For an expanding model, $\eta = 2\pi$ implies that the root is the future singularity. That $\theta = 0$ is a special case can be seen by consulting figure A.5: a ray starting at $\Delta = 0$ with $\theta = 0$ never intersects any of the other lines of the diagram. In general, each time a ray crosses one of the lines there is qualitative change in the properties of the roots.

For $0 < \theta \leq \pi/4$ a great deal more complexity is evident in figure A.4. First, consider a ray emanating with small angle $0 < \theta < \theta_c^+$ in figure A.5 ($\tan\theta_c^+ = 1/2$ is the slope of the $E = 0$ line at the origin). Eventually such a line will cross the black line which is the $E = 0$ critical solution labelled $\Delta_{E=0}$. For small Δ the models are closed; for larger Δ they are open. In figure A.4 this distinction corresponds to the the blue shading (closed models) at small Δ versus the unshaded (open) models at large Δ.

Within the shaded region note that two branches of real roots are present beyond a given time; at large t (asymptotically) the lower branch is $\Delta \rightarrow 0$ and the upper branch is $\Delta \rightarrow \Delta_{E=0}$. The lower branch sets the time of validity for small Δ. Each root is the collapse time of a closed model which has both density and velocity perturbations at the initial time.

As Δ increases the time of validity inferred from the lower branch decreases. At the critical point $\Delta = \Delta_{rc}$, the two real branches merge and connect to a branch of complex roots (intersection of red and blue points). For $\Delta > \Delta_{rc}$, the complex roots determine the time of validity even though the upper branch provides a real root. The complex roots do not have a direct physical interpretation in terms of future singularities of physical models. On figure A.5 the ray emanating from the origin at shallow angle crosses the red dashed line labelled Δ_{rc} at this critical point.

Physically, when Δ exceeds Δ_{rc}, the velocity perturbation dominates the density perturbation in the sense that the collapse time begins to increase. The real root corresponds to the future singularity of the model. As Δ increases further, the solution eventually becomes critical (infinite collapse time). The particular value where this occurs is $\Delta_{E=0}$ and it corresponds on figure A.5 to the ray crossing the labelled black line. Within the entire range $\Delta_{rc} < \Delta < \Delta_{E=0}$ the complex root determines the time of validity. So, even though any model in this range is closed and possesses a real future singularity, the time of validity is determined by the complex root. This gives the sliver on figure 3.10 which is the overlap of light red and blue shadings.

Both Δ_{rc} and $\Delta_{E=0}$ decrease as $\theta \to \theta_c^+$ as is evident from figure A.5 and both vanish at θ_c^+. On figure A.4 the real roots completely disappear and only the complex roots are present, i.e. the two real branches have been pushed out to infinite times. The panel with $\theta = 5\pi/36 = 0.436$ is numerically closest to the critical case $\theta_c^+ = 0.464$ and the real branches are just barely visible at the right hand edge.

For the rest of the upper half plane $\theta_c^+ < \theta \leq \pi$ the ray no longer intersects any closed models.

For $\theta_c^+ < \theta < \pi/4$ the real roots reappear and move back to the left in figure A.4 (see panel with $\theta = \pi/6$). Now, however, the roots are negative (see figure A.6). This is a manifestation of mirror symmetry which relates the negative real roots of an open model to the positive real roots of a closed model. At large t

the two branches have $\Delta \to 0$ and $\Delta \to \Delta_{E=0}$ and are completely analogous to the real branches just discussed for closed models. The separation between the two real branches increases as θ increases and the solution loci shifts upwards in Δ. And just as before the two branches join and meet a complex branch. The second red dashed line Δ_{rc} in figure A.5 shows the real to complex transition for the roots for the open models.

This behavior might be expect to continue for $\pi/4 < \theta < \pi$ but there is an additional complication: the analytic extension involves two forms. As the ray sweeps counterclockwise in figure A.3 it crosses $\delta_v = 1$ (horizontal dashed line and the curved blue line. These are also schematically illustrated in figure A.5.

$\pi/4 < \theta < \pi/2$

All physical models are in this range are open. Real roots have a straightforward interpretation in terms of the mirror models. Although some of the analysis described for $\theta < \pi/4$ continues to apply several additional complications ensue. To understand them it is useful refer to the phase space picture shown in figure A.5. As θ increases, the point where Δ_{rc} meets $\delta_v = 1$ is labelled P.

For a fixed θ consider increasing Δ from small values near the origin to ∞. The order in which this ray intersects the green ($\delta_v = 1$), purple ($\delta = 1$), red (Δ_{rc}) and blue (one or two complex forms) curves will correlate with the change in roots.

The roots are negative real for small Δ. They correspond to the collapse time of a closed mirror model. Increase Δ and ignore Δ_{rc}. When the $\delta_v = 1$ line is crossed, the sign of the closed mirror model's velocity switches from expanding to contracting. This just means that the labeling of the future singularity switches from further away ($\eta = 2\pi$) to nearer ($\eta = 0$). Now recall $\Delta < \Delta_{rc}$ implies real roots and, by definition, $\delta_v = \Delta \sin\theta$. Hence, $\Delta_{rc}(\theta) > 1/\sin\theta$ implies that the label switch occurs just as outlined. On figure A.5 rays counterclockwise of point P belong to this case. This is responsible for the switch from blue (real $\eta = 2\pi$) to cyan (real $\eta = 0$) roots at the green line in figure A.4 for $\theta = \pi/3$ and $17\pi/36$.

Conversely, if $\Delta_{rc}(\theta) < 1/\sin\theta$ the roots are already complex and the label switch occurs between the corresponding complex roots. There are no pictured examples in figure A.4.

In the previous section with the $0 < \theta \leq \pi/4$, the physical interpretation of Δ_{rc} (as Δ increases) was that the velocity contribution to the perturbation became dominant in the original model if the model was closed or in the mirror closed model if the original model was open. In latter case the mirror models were initially expanding. Now, the same idea continues to apply in the regime $\pi/4 < \theta < 0.84$. Here the transition from real to complex roots occurs before the $\delta_v = 1$ line is crossed. The significance of Δ_{rc} is that it marks the increasing importance of velocity perturbations in the closed expanding mirror models.

However, for $0.84 < \theta < \pi/2$ as Δ increases the open model crosses $\delta_v = 1$, the mirror model swaps from $\eta = 2\pi$ to 0 and the roots (real) corresponds to the real future singularity of a closed, contracting model. As Δ increases further, first the mirror model becomes critical and then an open model contracting to a future singularity. While the magnitude of Δ grows larger than a critical value the velocity perturbation dominates the mirror model dynamics. When $\Delta > \Delta_{rc}$ the roots switch from real to complex. At this point the contracting mirror model can be open, closed or critical.

Note in figure A.5 that Δ_{rc} asymptotes to the vertical purple line $\delta = 1$. The corresponding mirror model hits the line $\delta = -1$ in the third quadrant. This is the limiting vacuum solution. Although there are no physical models beyond the analytic extension continues and the roots change from real to complex. All open models with $\theta \lesssim \pi/2$ see a transition to complex roots as the mirror approaches the vacuum solution.

Finally figure A.5 shows as a blue curve the point at which there is a switch in complex form of the analytic extension. Here, the complex roots switch from $\eta = 0$ to $\eta = 2\pi$. The roots remain complex and since there is no physical interpretation and it is irrelevant whether they belong to $\eta = 0$ or $\eta = 2\pi$.

In figure A.4 the panel with $\theta = \pi/3$ and $17\pi/36$ show these transitions: the blue to cyan transition at the green dashed line is the mirror model switch from expanding to contracting; the cyan to pink transition at the purple dashed line is the mirror model moving through $\delta = -1$; the pink to red transition is the switch from two to one complex roots and $\eta = 0$ to $\eta = 2\pi$.

$\theta = \pi/2$

At $\theta = \pi/2$, only real roots of $\eta = 0$ are present for large Δ. This is a special case in that a ray only intersects one special line $\delta_v = 1$ in the upper half plane.

$\pi/2 < \theta \leq \pi$

All models in this range also correspond to open models. Like the previous cases, small Δ have real, negative roots with $\eta = 2\pi$. The mirror models in this case lie in the fourth quadrant. The crossover of real roots from $\eta = 0$ to $\eta = 2\pi$ occurs at $\delta_v = 1$, however, unlike in the earlier case, the line $\delta = -1$ is never approached by the mirror models in the fourth quadrant. As a result, there is no switch from real to complex roots and all models have real negative roots. The $\eta = 2\pi$ roots for small Δ are collapse times of initially expanding closed mirror models and the $\eta = 0$ are future singularities of initially contracting closed and open mirror models for intermediate and large values of Δ respectively.

A.4.2 Numerical Results

Here we present numerical formulas that give the time of validity for any initial Δ and θ. Real roots occur for small Δ when $0 < \theta < \pi/2$; and they occur for all Δ when $\pi/2 \leq \theta \leq \pi$ or $\theta = 0$. Real roots correspond to past or future singularities of physical models and are known exactly.

Figure A.4 shows that complex roots occur $0 < \theta < \pi/2$. In the range $\pi/4 < \theta < \pi/2$ figure A.6 shows that the phase of the complex roots is very close to π. We can approximate these roots as real, negative roots. Conversely, figure A.6 also shows that in the range $0 < \theta \leq \pi/4$ the phase is not close to 0 or π. These roots are complex only when $\Delta > \Delta_{rc}$. First, we fit Δ_{rc} by

$$\Delta_{rc,app}(\theta) = \left|0.41 \csc^2\theta(\cos\theta - 2\sin\theta) + 3.57(\cos\theta - 2\sin\theta)(\sin\theta)^{4.39}\right|. \qquad \text{(A.38)}$$

We cannot approximate the time of validity with the results for physical cases

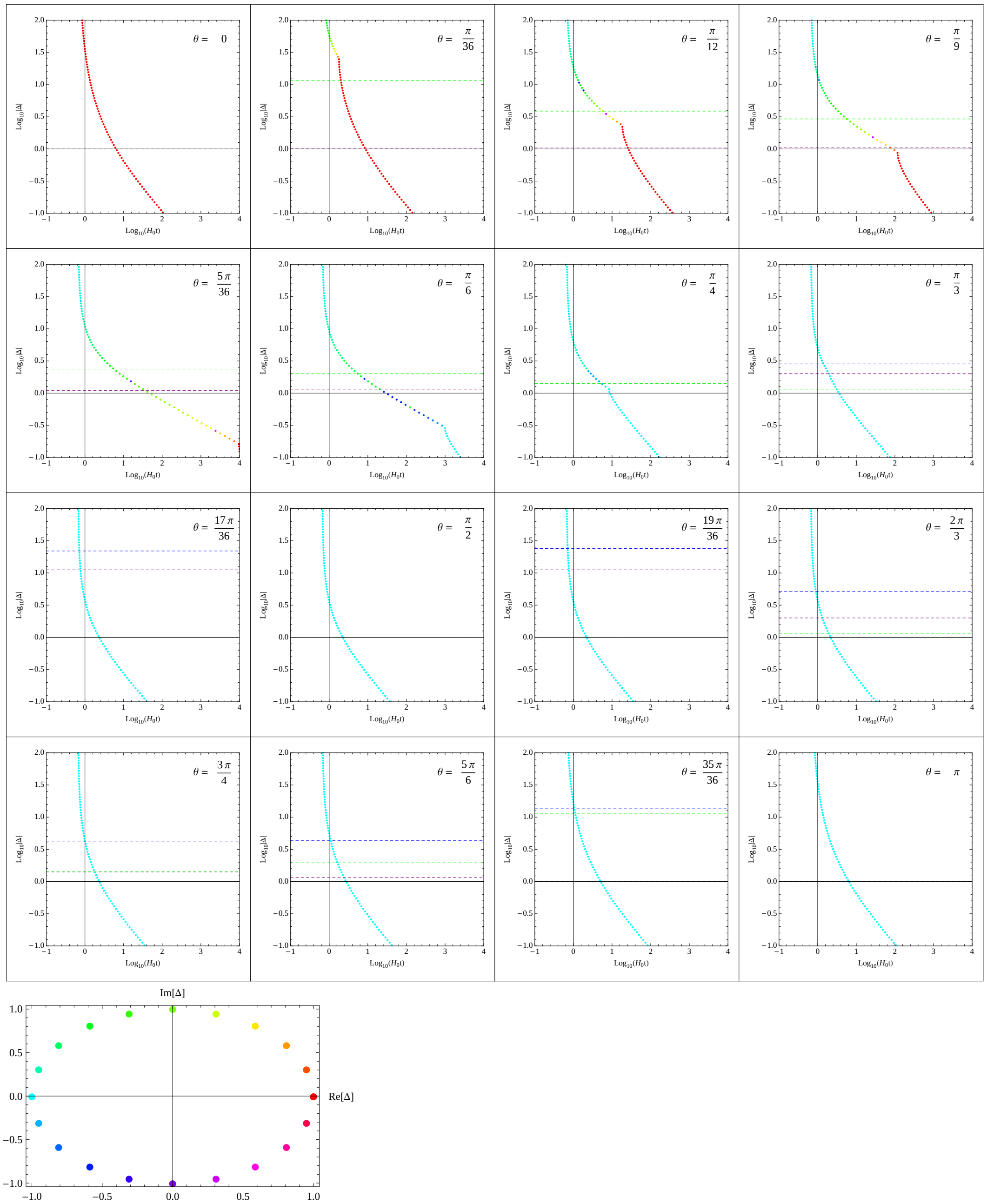

Figure A.6: Roots with $\eta = 2\pi$ plotted in the complex Δ plane for $0 < \theta \leq \pi$. These values of θ correspond to those in figure A.4. The color codes the complex phase of the roots ($\mathbf{\Delta} = \Delta e^{i\phi}$). The real positive ($\phi = 0$) and negative ($\phi = \pi$) roots are shown in red and cyan respectively. The complex roots can have any color other than these two and the bottom figure provides the coding. By comparison with figure A.4 one sees that all open models with real roots are cyan (negative); likewise all closed models with real roots are red (positive). Note, however, that there exist complex roots for both open and closed models.

but it turns out that the numerically derived time of validity is insensitive to θ in the range $0 < \theta < \pi/4$ and may be fit

$$H_0 t_{app}(\Delta) = \frac{2}{3} + \begin{cases} \frac{14.125}{\Delta^{2.5}} & 0 < \Delta \leq 1 \\ \frac{1.514}{\Delta^{2.82}} & 1 < \Delta \leq 2 \\ \frac{1.778}{\Delta^{3.13}} & 2 < \Delta \leq 5 \\ \frac{63095}{\Delta^{9.6}} & 5 < \Delta \leq 10 \\ \frac{2\times 10^{6}}{\Delta^{8.5}} & \Delta > 10. \end{cases} \tag{A.39}$$

Using these quantities, the table below gives an approximation to the time of validity, T_{app}, for all values of θ and Δ. The times for collapse and the bang times are equivalent to eq. (A.35) and reproduced here for convenience:

$$t_{coll}(\Delta,\theta) = t_0 + \frac{1}{2H_0}\frac{(1+\Delta\cos\theta)}{[-E(\Delta,\theta)]^{3/2}}(2\pi) - t_{age}(\Delta,\theta) \tag{A.40}$$

$$t^{-}_{bang}(\Delta,\theta) = t_0 + t_{age}(\Delta,\theta) \tag{A.41}$$

where

$$\begin{aligned} t_{age}(\Delta,\theta) &= \frac{1}{H_0}\sqrt{(1+\Delta\cos\theta)}\sqrt{\frac{(1+\Delta\sin\theta)^2}{(1+\Delta\cos\theta)}} \\ &\quad -\frac{1}{H_0}\frac{(1+\Delta\cos\theta)}{[E(\Delta,\theta)]^{3/2}}\sinh^{-1}\sqrt{\frac{E(\Delta,\theta)}{(1+\Delta\cos\theta)}}, \end{aligned} \tag{A.42}$$

$$E(\Delta,\phi,\theta) = (1+\Delta\sin\theta)^2 - (1+\Delta\cos\theta) \tag{A.43}$$

The error in the fit is estimated as

$$\mathcal{E} = \frac{T - T_{app}}{T}. \tag{A.44}$$

If $\mathcal{E} > 0$ then the approximation is conservative in this sense: the approximate time of validity is less than the true value. Conversely, if $\mathcal{E} < 0$, then the

Table A.1: Approximation to time of validity, $T_{app}(\Delta, \theta)$, for $0 \leq \theta \leq \pi$. Note that $\Delta_{rc,app}$ is an approximation to Δ_{rc} in eq. (A.38).

Parameter range			T_{app}
$0 < \theta < \pi/4$	$0 < \Delta < \Delta_{rc,app}$	$E(\Delta, \theta) < 0$	$t_{coll}(\Delta, \theta)$
	$0 < \Delta < \Delta_{rc,app}$	$E(\Delta, \theta) > 0$	$t_{coll}(-\Delta, \theta)$
	$\Delta > \Delta_{rc,app}$		$t_{app}(\Delta, \theta)$
$\pi/4 < \theta \leq \pi/2$	$0 < \Delta < \frac{1}{\lvert \sin\theta \rvert}$		$t_{coll}(-\Delta, \theta)$
	$\frac{1}{\lvert \sin\theta \rvert} \leq \Delta \leq \left\lvert \frac{2\sin\theta - \cos\theta}{\sin\theta \cos\theta} \right\rvert$		$\Re\left[t^{-}_{bang}(-\Delta, \theta)\right]$
	$\Delta > \left\lvert \frac{2\sin\theta - \cos\theta}{\sin\theta \cos\theta} \right\rvert$		$\Re\left[t_{coll}(-\Delta, \theta)\right]$
$\pi/2 \leq \theta \leq \pi$	$0 < \Delta \leq \frac{1}{\lvert \sin\theta \rvert}$		$t_{coll}(-\Delta, \theta)$
	$\Delta > \frac{1}{\lvert \sin\theta \rvert}$		$t^{-}_{bang}(-\Delta, \theta)$

approximation overestimates the time of validity. Using the above fits the worst case is $\mathcal{E} \simeq -0.02$. We always use a time step δt which satisfies $\delta t < 0.98 T_{app}$ so that the inaccuracy in the approximation is irrelevant.

A.5 Error characterization of the Lagrangian series

We want to characterize the errors associated with calculating the solution at time t_f given some fixed initial conditions at time t_0. Errors arise because any real calculation involves truncating the Lagrangian expansion. We want to compare the errors that result from different choices of truncation order and of the number of re-expansion steps assuming all series expansions are convergent (i.e. all respect the time of validity). Let N_m represent the final physical coordinate generated with a m-th order calculation using N steps. Ultimately, we seek to characterize differences like $N_m - N'_{m'}$. The quantity 1_∞ is the exact answer.

Single step

The Lagrangian series solution for a single step has the form

$$1_\infty = a(t)\left(1 + \sum_{i=1}^{\infty} \frac{b^{(i)}(t)}{a(t)}\Delta_0^i\right)X_0, \tag{A.45}$$

where each $b^{(i)}$ satisfies

$$\ddot{b}^{(i)} - \frac{H_0^2 a_0^3 b^{(i)}}{a^3} = S^{(i)} \tag{A.46}$$

and initial conditions are specified at $t = t_0$. The initial conditions at each order and the forms for the first few $S^{(i)}$ are given in the text.

If $t_f - t_0 = \delta t << t_0$, then the solutions can be expanded in the small parameter $\delta t / t_0$. The solutions are

$$b^{(1)}(t)/a(t) \sim c^{(1)}\frac{\delta t}{t_0}, \tag{A.47}$$

$$b^{(i)}(t)/a(t) \sim c^{(i)}\left(\frac{\delta t}{t_0}\right)^{i+1} \text{ for } i \geq 2. \tag{A.48}$$

The coefficients $c^{(i)}$ depend on the angle θ and have a weak dependence on the Lagrangian order. The difference between the exact answer and the m-th order approximation for a single step is

$$1_\infty - 1_m = \left(\sum_{i=m+1}^{\infty} c^{(i)}\left(\frac{\delta t}{t_0}\right)^{i+1} \Delta_0^i\right)X_0. \tag{A.49}$$

As long as t_f is within the time of validity of LPT, by definition, the LPT series converges and from the equation above, the leading order error scales as $\sim (\delta t/t_0)^{m+2}\Delta^{m+1}$ (order terms first by powers of Δ and then by powers of $\delta t/t_0$).

Multiple steps

In general for a practical application one is limited to working at a finite Lagrangian order. In such cases, it becomes necessary to ask if convergence can be achieved by working at a finite Lagrangian order with increasing number of steps.

First, we outline the calculation. The initial data is subscripted by "0". For example, let the initial perturbed scale factor be $b_0 = b(t_0)$, the initial background scale factor a_0, the initial density contrast δ_0 and the initial velocity perturbation δ_{v0}. The Lagrangian expansion parameter Δ_0 and angle θ_0 follow from the relations $\delta_0 = \Delta_0 \cos\theta_0$ and $\delta_{v0} = \Delta_0 \sin\theta_0$. The physical coordinate is $r_0 = b_0 X_0$; for given r_0 the initial Lagrangian coordinate X_0 is fixed by choosing b_0 to be equal to a_0.

Consider taking N steps from initial to final time with an m-th order Lagrangian expansion. Assume that the final time is within the time of validity of the Lagrangian expansion. For definiteness, let the j-th time be $t_j = t_0 \beta^{j/N}$ where $\beta = t_f/t_0$ (so t_N is just the final time t_f). This geometric sequence of increasing steps is well-suited for an expanding background with a small growing perturbation. The scaling of differences like $N_m - 1_\infty$, $(N+1)_m - N_m$ and $N_{m+1} - N_m$ with N and m are all of interest. We expect the same scaling of these differences with N and m for any uniformly refined set of time steps.

A finite order Lagrangian expansion accurate to order m is a truncated representation of the full Lagrangian solution

$$b(t) = \sum_{i=0}^{m} b^{(i)}(t) \Delta_0^i. \tag{A.50}$$

At the beginning of the first step the scale factor at t_0 is advanced to t_1 and written as $b(t_0 \rightarrow t_1; \Delta_0, \theta_0)$. Note the explicit dependence on the perturbation parameters at t_0. Abbreviate the scale factor and its derivative for the truncated expression as b and $\dot{b}$. The background scale factor at time t_1 is a_1. At the end of the first step the Lagrangian coordinate X_1 and the new b_1 are inferred as described in the main body of the text by re-scaling quantities calculated at t_1. The new b_1 is *not* b. The net result for the full step $t_0 \rightarrow t_1$ is

$$\begin{aligned} X_1 &= X_0 \frac{b}{a_1} && \text{(A.51)} \\ b_1 &= a_1 && \text{(A.52)} \\ \dot{b}_1 &= \frac{\dot{b}}{b} a_1 && \text{(A.53)} \\ \delta_1 &= (1+\delta_0)\left(\frac{a_1}{b}\right)^3 - 1 && \text{(A.54)} \\ \delta_{v1} &= \frac{a_1 \dot{b}}{\dot{a}_1 b} - 1. && \text{(A.55)} \end{aligned}$$

The newly defined quantities subscripted by "1" will be used to initiate the next step. The updated perturbations imply new Lagrangian expansion parameter and angle according to

$$\begin{aligned} \Delta_1 &= \sqrt{\delta_1^2 + \delta_{v1}^2} && \text{(A.56)} \\ \cos\theta_1 &= \frac{\delta_1}{\Delta_1} && \text{(A.57)} \\ \sin\theta_1 &= \frac{\delta_{v1}}{\Delta_1}. && \text{(A.58)} \end{aligned}$$

The new physical position is $r_1 = b_1 X_1 = b X_0$. In a numerical calculation the truncated b is exact to floating point precision but contains an error because of the omitted orders; in a symbolic calculation b is known to order Δ_0^m.

The next step from $t_1 \rightarrow t_2$ involves a similar update with $b = b(t_1 \rightarrow t_2; \Delta_1, \theta_1)$

$$\begin{aligned} X_2 &= X_1 \frac{b}{a_2} && \text{(A.59)} \\ b_2 &= a_2 && \text{(A.60)} \end{aligned}$$

$$\dot{b}_2 = \frac{\dot{b}}{b} a_2 \tag{A.61}$$

$$\delta_2 = (1 + \delta_1) \left(\frac{a_2}{b} \right)^3 - 1 \tag{A.62}$$

$$\delta_{v2} = \frac{a_2 \dot{b}}{\dot{a}_2 b} - 1. \tag{A.63}$$

The new physical position is $r_2 = b_2 X_2$. This iterative scheme repeats for a total of N steps. It ultimately yields an approximation to the position at the final time denoted $N_m = b_N X_N$.

A difference like $(N + 1)_m - N_m$ may be calculated numerically for various N and m and the scaling fitted and inferred. In addition, one can approach the problem symbolically. To write N_m we need to expand the final result in powers of Δ_0. Note, for example, that Δ_1 and θ_1 are known as expansions in Δ_0 with coefficients that depend upon θ_0. Perturbation-related quantities are re-written systematically in terms of initial quantities. For example, $b(t_1 \to t_2; \Delta_1, \theta_1)$ may be expanded in powers of Δ_1 with coefficients depending upon θ_1. Next, all occurrences of Δ_1 and θ_1 are replaced by expansions in powers of Δ_0 and coefficients depending upon θ_0. All terms up to and including Δ_0^m are retained in the final result. This procedure is systematically repeated until all quantities are expressed in terms of initial data. Finally, the difference $(N+1)_m - N_m$ is calculated symbolically. Similar strategies allow construction of all the differences of interest.

To make analytic progress assume that $f_t = \beta - 1 = (t_f - t_0)/t_0 << 1$ is a small parameter. In a difference like $(N + 1)_m - N_m$ many "lower order" terms will coincide. Consider an ordering of terms by the powers of Δ_0 (first) and by powers of f_t (second). Define the leading-order difference to be the first non-vanishing term proportional to $\Delta_0^p f_t^q$ for smallest p and then smallest q. It is straightforward to apply this ordering to simplify the differences like $(N + 1)_m -$

N_m. The leading order differences satisfy the following simple equalities

$$\begin{aligned}
|1_\infty - N_m| &\sim |g_{N,m}| \\
|N_{m+1} - N_m| &\sim |g_{N,m}| \\
|(N+1)_m - N_m| &\sim |g_{N+1,m} - g_{N,m}|
\end{aligned} \tag{A.64}$$

where

$$\begin{aligned}
g_{N,m} &= K_{N,m} \cos\theta \sin^m \theta \Delta^{m+1} f_t^{m+2} \\
K_{N,m} &= \frac{1}{9}\left(\frac{-2}{3}\right)^m \left(\frac{N - \frac{m}{2+m}}{N^{m+1}}\right).
\end{aligned}$$

These differences can be compared with the numerical differences for which no expansion in f_t is carried out.

We verified the analytical scaling by the following numerical experiment. The parameters of the problem at the starting time t_0 are $\Delta_0 = 1/2$, $\theta_0 = -\pi/4$. The final time of interest t_f is close to the initial time so that $(t_f - t_0)/t_0 = 1/4$. The m-th order Lagrangian approximation is evaluated at this fixed final time with successively increasing number of steps. Values of m from 1 to 4 and values of N from 10 to 50 were considered. For geometric time steps $(t_{i+1} - t_i)/t_i = \beta^{1/N} - 1$ is independent of i and denoted $\delta t/t$ below.

The results are plotted in figure A.7. The points indicate the numerical data points and the solid lines indicate the analytical functions defined in eq. (A.64). The numerical calculation was done with a high enough precision that even small errors of the order of 10^{-14} are not contaminated by floating point errors. The agreement between the numerical experiment and the symbolic differences is very good.

Thus, the scaling of the errors implies that for a small total time step, any finite order Lagrangian scheme will yield convergent results upon taking

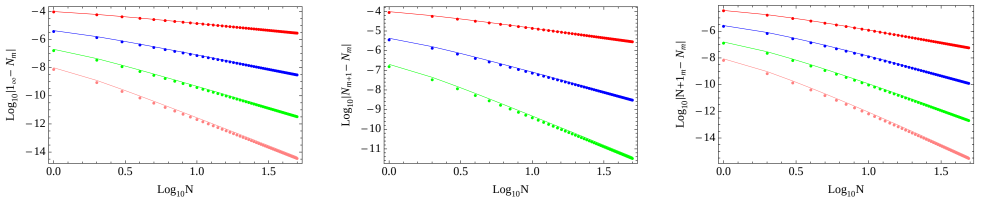

Figure A.7: The three panels show the log of the errors $|1_\infty - N_m|$, $|N_{m+1} - N_m|$ and $|(N+1)_m - N_m|$ vs. N. The final time t_f is the same for all these comparisons. The dots correspond to the data generated by the numerical experiment and lines correspond to the analytical formulas given in eq. (A.64). The lines from top to bottom correspond to $m = 1, 2, 3, 4$ respectively for the first and third panels and to $m = 1, 2, 3$ for the second panel. It is clear that for a fixed m, increasing the number of steps improves convergence. Conversely, for a fixed N, increasing the Lagrangian order m improves convergence.

multiple steps. Conversely, for a fixed number of steps, a higher order Lagrangian calculation will give better results.

It is useful to express the scaling in terms of the individual small step size $\delta t/t$. Under the assumptions that $(t_f - t_0)/t_0$ is small, $(t_f - t_0)/t_0 \sim N\delta t/t$. The scaling $|1_\infty - N_m| \sim N^{-m}\Delta^{m+1}((t_f - t_0)/t_0)^{m+2}$ can be re-written as $|1_\infty - N_m| \sim N((t_f - t_0)/t_0) \cdot \Delta^{m+1}(\delta t/t)^{m+1}$, which can be interpreted as an error of $((t_f - t_0)/t_0)\Delta^{m+1}(\delta t/t)^{m+1}$ per step. In the text, the quantity $\epsilon = \Delta\delta t/t$ is kept constant. For fixed initial and final times, the error scales $\propto N\epsilon^{m+1}$. If Δ does not change appreciably then the error is $\propto \Delta\epsilon^m$. Convergence is attained when $\epsilon \to 0$.

APPENDIX B

APPENDIX FOR CHAPTER 4

B.1 Mathematical Transformations

Changing the derivative with respect to r to that with respect to X in eqs. (4.1) and (4.2) involves the transformations outlined below.

B.1.1 Divergence Equation

$$\nabla_r \cdot \ddot{\mathbf{r}} = \frac{\partial \ddot{r}_i}{\partial r_i} = \frac{\partial \ddot{r}_i}{\partial X_l}\frac{\partial X_l}{\partial r_i} \tag{B.1}$$

where Einstein's repeated summation convention is followed.

The inverse transformation from X-space to r-space is given as

$$\frac{\partial X_l}{\partial r_i} = \frac{1}{2J}\epsilon_{lmn}\epsilon_{ijk}\frac{\partial r_j}{\partial X_m}\frac{\partial r_k}{\partial X_n} \tag{B.2}$$

where

$$J = \mathrm{Det}\left(\frac{\partial r_i}{\partial X_j}\right) = \epsilon_{abc}\frac{\partial r_1}{\partial X_a}\frac{\partial r_2}{\partial X_b}\frac{\partial r_3}{\partial X_c} = \frac{1}{6}\epsilon_{ipq}\epsilon_{jlm}\frac{\partial r_i}{\partial X_j}\frac{\partial r_p}{\partial X_l}\frac{\partial r_q}{\partial X_m} \tag{B.3}$$

and ϵ_{ijk} is the usual Levi-Civita symbol. Substituting in eq.(4.1) gives

$$\epsilon_{lmn}\epsilon_{ijk}\frac{1}{2J}\frac{\partial \ddot{r}_i}{\partial X_l}\frac{\partial r_j}{\partial X_m}\frac{\partial r_k}{\partial X_n} = -4\pi G\left(\frac{\rho_{m,0}a_0^3(1+\delta(\mathbf{X},t_0))}{J} + \rho_{d.e,0}(1+3w)\left(\frac{a_0}{a}\right)^{3(1+w)}\right). \tag{B.4}$$

Multiplying throughout by J and using eq. (B.3),

$$\begin{aligned} \frac{1}{2}\epsilon_{lmn}\epsilon_{ijk}\frac{\partial \ddot{r}_i}{\partial X_l}\frac{\partial r_j}{\partial X_m}\frac{\partial r_k}{\partial X_n} &= -4\pi G\rho_{m,0}a_0^3(1+\delta(\mathbf{X},t_0)) \\ &\quad -\frac{2\pi G}{3}\left(1+3w)\rho_{d.e,0}\left(\frac{a_0}{a}\right)^{3(1+w))}\epsilon_{lmn}\epsilon_{ijk}\frac{\partial r_i}{\partial X_l}\frac{\partial r_j}{\partial X_m}\frac{\partial r_k}{\partial X_n}\right). \end{aligned} \tag{B.5}$$

Using the definition of the $\hat{L}$ operator eq. (4.13), recasts eq. (B.5) as eq. (4.10).

B.1.2 Curl Equation : Irrotationality in Eulerian space

Consider the component of equation eq. (4.2) along the $\hat{r}_i$ direction. Again use (B.2) to write

$$(\nabla_r \times \ddot{\mathbf{r}})_i = \epsilon_{ijk}\frac{\partial \ddot{r}_k}{\partial r_j} = \epsilon_{ijk}\frac{\partial \ddot{r}_k}{\partial X_l}\frac{\partial X_l}{\partial r_j} = \frac{1}{2J}\epsilon_{ijk}\epsilon_{lmn}\epsilon_{jrs}\frac{\partial \ddot{r}_k}{\partial X_l}\frac{\partial r_r}{\partial X_m}\frac{\partial r_s}{\partial X_n} = 0. \tag{B.6}$$

Using the identity, $\epsilon_{ijk} = -\epsilon_{jik}$ and $\epsilon_{jik}\epsilon_{jrs} = \delta_{ir}\delta_{ks} - \delta_{is}\delta_{kr}$, one gets

$$(\nabla_r \times \ddot{\mathbf{r}})_i = -\epsilon_{lmn}\frac{\partial \ddot{r}_k}{\partial X_l}\frac{\partial r_i}{\partial X_m}\frac{\partial r_k}{\partial X_n} + \epsilon_{lmn}\frac{\partial \ddot{r}_k}{\partial X_l}\frac{\partial r_k}{\partial X_m}\frac{\partial r_i}{\partial X_n} = 2\epsilon_{lmn}\frac{\partial \ddot{r}_k}{\partial X_l}\frac{\partial r_k}{\partial X_m}\frac{\partial r_i}{\partial X_n} = 0. \tag{B.7}$$

Here, we have set each component of the vector $\nabla_r \times \mathbf{g}$ in the r basis equal to zero. In vector form

$$\epsilon_{lmn}\frac{\partial \ddot{r}_k}{\partial X_l}\frac{\partial r_k}{\partial X_m}\frac{\partial r_i}{\partial X_n}\hat{r}_i = \bar{0}. \tag{B.8}$$

One can also express the components of $\nabla_r \times \mathbf{g}$ in the X basis. The two basis vectors are related by

$$\hat{r}_i = \frac{\partial X_p}{\partial r_i}\hat{X}_p. \tag{B.9}$$

Re-expressing $\nabla_r \times \mathbf{g}$ in the $\hat{X}$ basis gives

$$\epsilon_{lmn}\frac{\partial \ddot{r}_k}{\partial X_l}\frac{\partial r_k}{\partial X_m}\frac{\partial r_i}{\partial X_n}\frac{\partial X_p}{\partial r_i}\hat{X}_p = 0. \tag{B.10}$$

But $\partial r_i/\partial X_n \cdot \partial X_p/\partial r_i = \delta_{pn}$ Since the basis vectors are all independent, the individual components must be zero. The simplified condition for each n is

$$\epsilon_{nlm}\frac{\partial \ddot{r}_k}{\partial X_l}\frac{\partial r_k}{\partial X_m} = 0. \tag{B.11}$$

Using the definition of the $\hat{T}$ operator eq. (4.14) recasts eq. (B.11) as eq. (4.10).

B.2 Properties of the $\hat{L}$ and $\hat{\mathbf{T}}$ operators

.

$$\hat{L}[c \cdot \mathbf{F}^{(\alpha)}, \mathbf{F}^{(\beta)}, \mathbf{F}^{(\gamma)}] \quad = \quad c \cdot \hat{L}[\cdot\mathbf{F}^{(\alpha)}, \mathbf{F}^{(\beta)}, \mathbf{F}^{(\gamma)}], \tag{B.12}$$

$$\hat{L}[\mathbf{F}^{(\alpha)}, \mathbf{F}^{(\beta)}, \mathbf{F}^{(\gamma)}] = \hat{L}[\mathbf{F}^{(\beta)}, \mathbf{F}^{(\alpha)}, \mathbf{F}^{(\gamma)}], \tag{B.13}$$

$$\hat{L}[\mathbf{F}^{(\alpha)} + \mathbf{F}^{(\eta)}, \mathbf{F}^{(\beta)}, \mathbf{F}^{(\gamma)}] = \hat{L}[\mathbf{F}^{(\alpha)}, \mathbf{F}^{(\beta)}, \mathbf{F}^{(\gamma)}] + \hat{L}[\mathbf{F}^{(\eta)}, \mathbf{F}^{(\beta)}, \mathbf{F}^{(\gamma)}]. \tag{B.14}$$

Similar properties hold for the $\hat{\mathbf{T}}$ operator. In addition

$$\hat{\mathbf{T}}[\mathbf{F}^{(\alpha)}, \mathbf{F}^{(\alpha)}] = 0. \tag{B.15}$$

B.3 Separating the spatial and temporal solutions

This section first explains the equations and initial conditions and then outlines the implementation algorithm.

B.3.1 Equations and initial conditions

For the first order, the equations to be solved have the form

$$D_t^L \left[\nabla_{\mathrm{x}} \cdot \mathbf{p}^{(1)}\right] = -\frac{3}{2} H_0^2 \Omega_{m,0} a_0^3 \delta(\mathbf{X}, t_0), \tag{B.16}$$

$$D_t^T \left[\nabla_{\mathrm{x}} \times \mathbf{p}^{(1)}\right] = 0. \tag{B.17}$$

and for higher order the form is

$$D_t^L \left[\nabla_{\mathrm{x}} \cdot \mathbf{p}^{(n)}\right] = S^{(n,L)}, \tag{B.18}$$

$$D_t^T \left[\nabla_{\mathrm{x}} \times \mathbf{p}^{(n)}\right] = \mathbf{S}^{(n,T)}. \tag{B.19}$$

These equations are subject to initial conditions:

At first order

$$\mathbf{p}^{(1,L/T)}(\mathbf{X}, t_0) = 0, \tag{B.20}$$

$$\dot{\mathbf{p}}^{(1,L/T)}(\mathbf{X}, t_0) = \mathbf{v}^{L/T}(\mathbf{X}, t_0). \tag{B.21}$$

At all higher orders $n > 1$,

$$\mathbf{p}^{(n,L/T)}(\mathbf{X}, t_0) = 0 \tag{B.22}$$

$$\dot{\mathbf{p}}^{(n,L/T)}(\mathbf{X}, t_0) = 0. \tag{B.23}$$

The form of the time derivative operators and the source terms are given in the text.

The initial perturbation is described by one scalar field corresponding to the initial density field and two vector fields corresponding to the curl-free and divergence-less parts of the velocity field. The initial acceleration field (vector) can be constructed from the initial density field via Poisson's equation and is also curl-free. All the three vector fields are taken to be of first order (by choice). Since the spatial and temporal operators in eqs. (B.16) and (B.17) commute, the first order displacement field can be written as a linear combination of these three independent vectors with purely time dependent coefficients. Splitting into the longitudinal and transverse components, the first order displacement $\mathbf{p}^{(1)}$ is written as

$$\mathbf{p}^{(1,L)} = b_\delta(t)\mathbf{F}_\delta(\mathbf{X}) + b_v^L(t)\mathbf{F}_v^L(\mathbf{X}), \tag{B.24}$$

$$\mathbf{p}^{(1,T)} = b_v^T(t)\mathbf{F}_v^T(\mathbf{X}). \tag{B.25}$$

The superscripts denote the order and type of the term. Substituting in eqs. (B.16) and (B.17) gives,

$$D_t^L b_\delta(t)[\nabla \cdot \mathbf{F}_\delta] + D_t^L b_v^L(t)[\nabla \cdot \mathbf{F}_v^L] = -\frac{3}{2}H_0^2\Omega_{m,0}a_0^3\delta(\mathbf{X}, t_0). \tag{B.26}$$

$$D_t^T b_v^T(t)[\nabla \times \mathbf{F}_v^T] = 0. \tag{B.27}$$

The initial conditions that $\mathbf{p}^{(1)}$ satisfies are given by eqs. (B.20) and (B.21). There is a choice to be made in how these initial conditions translate to conditions on the temporal and spatial functions. We choose to set the spatial functions as

$$\nabla \cdot \mathbf{F}_\delta = \delta(\mathbf{X}, t_0), \tag{B.28}$$

$$\mathbf{F}_v^L = \mathbf{v}^L(\mathbf{X}, t_0), \tag{B.29}$$

$$\mathbf{F}_v^T = \mathbf{v}^T(\mathbf{X}, t_0) \tag{B.30}$$

and the temporal equations as

$$D_t^L b_\delta(t) = -\frac{3}{2} H_0^2 \Omega_{m,0} a_0^3 \tag{B.31}$$

$$D_t^L b_v^L(t) = 0, \tag{B.32}$$

$$D_t^T b_v^T(t) = 0. \tag{B.33}$$

subject to the initial conditions

$$b_\delta(t_0) = 0 \tag{B.34}$$

$$\dot{b}_\delta(t_0) = 0 \tag{B.35}$$

$$b_v^{L,T}(t_0) = 0 \tag{B.36}$$

$$\dot{b}_v^{L,T}(t_0) = 1. \tag{B.37}$$

The Poisson equation eq. (B.28) is subject to periodic boundary conditions and is solved using Fourier transforms. This prescription completely specifies the first order solution.

At higher orders ($n > 1$), the source terms are combinations of lower order terms. The general structure of a longitudinal and transverse source terms at the n-th order is of the form

$$S^{(n,L)} = \sum_{\substack{\alpha,\beta,\gamma \\ \alpha+\beta+\gamma=n}} h^L_{\alpha,\beta,\gamma}(t) \cdot \hat{L}[\mathbf{F}^{(\alpha)}, \mathbf{F}^{(\beta)}, \mathbf{F}^{(\gamma)}] \tag{B.38}$$

$$\mathbf{S}^{(n,T)} = \sum_\alpha h^T_\alpha(t) \hat{\mathbf{T}}[\mathbf{F}^{(\alpha)}, \mathbf{F}^{(n-\alpha)}]. \tag{B.39}$$

For the longitudinal term, α, β, γ can take any value from 0 to $n-1$ and $\mathbf{F}^{(0)} = \mathbf{X}$. For the transverse term, α can take values from 1 to $n-1$.

It is easy to calculate all the independent source terms symbolically at all orders using the symmetries and properties of the $\hat{L}$ and $\hat{\mathbf{T}}$ operators. Let $Z_{n,L}$ and $Z_{n,T}$ denote the number of such independent longitudinal and transverse terms respectively (see table B.1). The form for the longitudinal and transverse displacements can then be taken as

$$\mathbf{p}^{(n,L)} = \sum_{i=1}^{Z_{n,L}} b_i^{(n,T)}(t)\mathbf{F}_i^{(n,T)}(\mathbf{X}) \tag{B.40}$$

$$\mathbf{p}^{(n,T)} = \sum_{i=1}^{Z_{n,T}} b_i^{(n,T)}(t)\mathbf{F}_i^{(n,T)}(\mathbf{X}) \tag{B.41}$$

where the spatial functions $\mathbf{F}^{(n,L)}$ and $\mathbf{F}^{(n,T)}$ satisfy an equation of the form

$$\nabla_X \cdot \mathbf{F}^{(n,L)} = \hat{L}[\mathbf{F}^{(\alpha)}, \mathbf{F}^{(\beta)}, \mathbf{F}^{(\gamma)}] \tag{B.42}$$

$$\nabla_X \times \mathbf{F}^{(n,T)} = \hat{\mathbf{T}}[\mathbf{F}^{(\alpha)}, \mathbf{F}^{(n-\alpha)}] \tag{B.43}$$

and the temporal functions $b^{(n,L)}(t)$ and $b^{(n,T)}(t)$ satisfy

$$D_t^L b^{(n,L)}(t) = h^L_{\alpha,\beta,\gamma}(t) \tag{B.44}$$

$$D_t^T b^{(n,T)}(t) = h^T_{\alpha}(t) \tag{B.45}$$

The temporal equations at all orders higher than the first are subject to the initial conditions $b^{(n,L/T)}(t_0) = 0, \dot{b}^{(n,L/T)}(t_0) = 0$. The spatial equations are subject to periodic boundary conditions.

B.3.2 Algorithm

1. Specify the order of the scheme and the number of initial functions at first order. In general $Z_{1,L} = 2$ and $Z_{1,T} = 1$. If the initial conditions start with

Table B.1: Number of transverse and longitudinal terms as a function of Lagrangian order and type of initial conditions.

Order	$\mathbf{v}^T = 0$	$\mathbf{v}^T \neq 0$
n=1	$Z_L = 2, Z_T = 0$	$Z_L = 2, Z_T = 1$
n=2	$Z_L = 3, Z_T = 1$	$Z_L = 6, Z_T = 3$
n=3	$Z_L = 12, Z_T = 8$	$Z_L = 37, Z_T = 27$

zero transverse velocity then $Z_{1,T} = 0$.

2. Construct all the longitudinal and source terms formally $\hat{L}[\mathbf{F}^{(\alpha)}, \mathbf{F}^{(\beta)}, \mathbf{F}^{(\gamma)}]$ and $\hat{\mathbf{T}}[\mathbf{F}^{(\alpha)}, \mathbf{F}^{(\beta)}]$. Counting the terms determines $Z_{n,L}$, $Z_{n,T}$.

3. Substitute the ansatz $\mathbf{r} = a(t)\mathbf{X} + \sum_n \mathbf{p}^{(n,L)} + \sum_n \mathbf{p}^{(n,T)}$ in the equation

$$\begin{aligned} \hat{L}[\ddot{\mathbf{r}}, \mathbf{r}, \mathbf{r}] &= -3H_0^2\Omega_{m,0}a_0^3(1 + \delta(\mathbf{X}, t_0)) \\ &\quad -\frac{H_0^2}{2}(1 + 3w)\Omega_{d.e,0}\left(\frac{a_0}{a}\right)^{3(1+w)} \hat{L}[\mathbf{r}, \mathbf{r}, \mathbf{r}] \qquad \text{(B.46)} \\ \hat{\mathbf{T}}[\ddot{\mathbf{r}}, \mathbf{r}] &= 0 \qquad \text{(B.47)} \end{aligned}$$

The form for the displacement vectors is given by eq. (B.40) and eq. (B.41). Use properties of the $\hat{L}$ and $\hat{\mathbf{T}}$ operators given in Appendix B.2 to simplify.

4. Obtain the time-dependent coefficients of the terms $\hat{L}[\mathbf{F}^{(\alpha)}, \mathbf{F}^{(\beta)}, \mathbf{F}^{(\gamma)}]$ and $\hat{\mathbf{T}}[\mathbf{F}^{(\alpha)}, \mathbf{F}^{(\beta)}]$. These are the source terms for the temporal equations. Construct the set of temporal equations which have the form eq. (B.44) and eq. (B.45) and are subject to the initial conditions given above.

5. The symbolic spatial sources are then used to solve the spatial equations.

B.4 Numerical implementation of the LPT scheme

This implementation of the LPT scheme consists of two parts. The first part consists of symbolically obtaining all the spatial and temporal equations to be solved and the second part is the numerical implementation of the solution.

The symbolic manipulations involved and the algorithm for the first part are outlined in Appendix B.3. The main point is that the displacement vector at each order can be written as a sum of many terms of which each term is of the type $b(t)\mathbf{F}(\mathbf{X})$. At the n-th order there are $Z_{n,L}$ such terms that correspond to the longitudinal functions and $Z_{n,T}$ such terms that correspond to the transverse functions denoted as $b^{(n,L/T)}$ and $\mathbf{F}^{(n,L/T)}(\mathbf{X})$. The temporal functions $b(t)$ all satisfy second order O.D.E with two initial conditions and the spatial equations at each order are of two types

$$\nabla_X \cdot \mathbf{F}^L(\mathbf{X}) = S^L(\mathbf{X}) \tag{B.48}$$

$$\nabla_X \times \mathbf{F}^T(\mathbf{X}) = \mathbf{S}^T(\mathbf{X}) \tag{B.49}$$

where $S^L(\mathbf{X})$ and $\mathbf{S}^T(\mathbf{X})$ are known scalar and vector source terms that depend on partial derivatives of lower order displacement fields. The spatial equations are subject to periodic boundary conditions.

The second part of the scheme consists of numerically solving these equations. The separation of the spatial and temporal equations allows them to be solved independent of each other. The temporal equations are solved together as a set of simultaneous second order differential equations using a standard ODE solver (NDSolve in *Mathematica* was used here). The spatial equations are solved on a three dimensional grid using Fourier transforms. The three main operations involved in obtaining the spatial part of the solution are calculating partial derivatives for the source terms, solving the divergence equation and solving the curl equation of the form mentioned above. These are done on a equispaced grid using discrete Fourier transforms and the technical details for them are given in appendices B.6, B.5, B.7. The algorithm for obtaining the full solution is outlined below.

B.4.1 Algorithm

1. Set up the grid in coordinate and Fourier space. This grid stays fixed for the entire simulation. Let L_x, L_y, L_z and N_1, N_2, N_3 denote the dimensions of the box and resolution in each dimension respectively. Choose the center of the box to be the origin. The grid coordinates in the spatial directions extend from $-L/2$ to $L/2$.

   $$x[i] = \begin{cases} (i-1)\Delta_x & i = 1, \dots N/2+1 \\ (i-1)\Delta_x - L & i = N/2+2 \dots N \end{cases} \tag{B.50}$$

   where $\Delta_x = L/N$.

   In Fourier space, the grid coordinates extend from $-k_c$ to k_c where k_c is the Nyquist frequency $k_c = 2\pi \cdot N/(2L)$.

   $$k[i] = \begin{cases} (i-1)\Delta_k & i = 1, \dots N/2+1 \\ (i-1)\Delta_k - 2k_c & i = N/2+2 \dots N \end{cases} \tag{B.51}$$

   where $\Delta_k = 2k_c/N = 2\pi/L$.

2. Get the symbolic forms of the temporal equations and spatial source terms. This in general depends on the number and type of functions at the first order and the order of the scheme. The algorithm is described in Appendix B.3.

3. Solve the temporal part

    (a) Specify the initial time t_0 and final time t_f.

    (b) Assign values to the cosmological parameters that dictate the background evolution a_0, H_0, $\Omega_{m,0}, \Omega_{de,0}$.

    (c) Specify the initial conditions for each of the temporal functions at all orders (see Appendix B.3).

    (d) Solve the temporal equations for all temporal functions $b^{(n,L/T)}(t)$. Store all $b_i^{(n,L)}(t)$ $(i = 1, \dots Z_{n,L})$ and $b_i^{(n,T)}(t)$ $(i = 1, \dots Z_{n,T})$.

4. Solve the spatial part.

    (a) Set up the arrays corresponding to the initial density field $\delta(\mathbf{X}, t_0)$ and velocity field $\mathbf{v}(\mathbf{X}, t_0)$. If the longitudinal and transverse parts of the velocity field are not known independently, extract them as follows: Solve $\nabla_X \cdot \mathbf{v}^L(\mathbf{X}, t_0) = \nabla_X \cdot \mathbf{v}(\mathbf{X}, t_0)$ for $\mathbf{v}^L(\mathbf{X}, t_0)$. Set $\mathbf{v}^T(\mathbf{X}, t_0) = \mathbf{v}(\mathbf{X}, t_0) - \mathbf{v}^L(\mathbf{X}, t_0)$.

    (b) At first order solve $\nabla_X \cdot \mathbf{F}_\delta = \delta(\mathbf{X}, t_0)$ and set $\mathbf{F}_v^{L,T} = \mathbf{v}^{L,T}(\mathbf{X}, t_0)$.

    (c) At second order evaluate the sources $S^L(\mathbf{X})$ and $\mathbf{S}^T(\mathbf{X})$ on the grid for the divergence equation and solve the divergence equation and curl equations for the longitudinal and transverse terms respectively. Refer to the definitions and the Appendices B.6, B.5, B.7 for the numerical implementation of the solutions.

    (d) Repeat the previous step for all higher orders until the maximum order is reached. Store all spatial solutions for $\mathbf{F}_i^{(n,L)}(\mathbf{X})$ $(i = 1, \dots Z_{n,L})$ and $\mathbf{F}_i^{(n,T)}(\mathbf{X})$ $(i = 1, \dots Z_{n,T})$.

5. Reconstruct the physical position and velocity at any later time t.

$$\begin{aligned}\mathbf{r} &= a(t)\mathbf{X} + \mathbf{p}(\mathbf{X}, t) && \text{(B.52)}\\ \dot{\mathbf{r}} &= \dot{a}(t)\mathbf{X} + \dot{\mathbf{p}}(\mathbf{X}, t) && \text{(B.53)}\end{aligned}$$

where

$$\begin{aligned}\mathbf{p}(\mathbf{X}, t) &= \sum_n \mathbf{p}^{(n)}(\mathbf{X}, t) && \text{(B.54)}\\ &= \sum_n \left[\sum_{i=1}^{Z_{n,L}} b_i^{(n,L)}(t)\mathbf{F}_i^{(n,L)}(\mathbf{X}) + \sum_{i=1}^{Z_{n,T}} b_i^{(n,T)}(t)\mathbf{F}_i^{(n,T)}(\mathbf{X})\right]\\ \dot{\mathbf{p}}(\mathbf{X}, t) &= \sum_n \dot{\mathbf{p}}^{(n)}(\mathbf{X}, t) && \text{(B.55)}\\ &= \sum_n \left[\sum_{i=1}^{Z_{n,L}} \dot{b}_i^{(n,L)}(t)\mathbf{F}_i^{(n,L)}(\mathbf{X}) + \sum_{i=1}^{Z_{n,T}} \dot{b}_i^{(n,T)}(t)\mathbf{F}_i^{(n,T)}(\mathbf{X})\right]\end{aligned}$$

6. Compute the density at any later time t.

$$J(\mathbf{X}, t) = Det\left(\frac{\partial r_i}{\partial X_j}\right) \tag{B.56}$$

$$\delta(\mathbf{X}, t) = \frac{(1 + \delta(\mathbf{X}, t))a(t)^3}{J(\mathbf{X}, t)} - 1 \tag{B.57}$$

7. If multiple steps are being taken, reinitialize the system as follows:

   Let the initial and final time in the previous step be denoted as t_0 and t_1 respectively and Lagrangian coordinates as $\mathbf{X}_0$ and $\mathbf{X}_1$ respectively. The physical position and velocity of the particles is not altered by the labeling. This sets the relationship between the coordinate labels $\mathbf{X}_0$ and $\mathbf{X}_1$ and sets the initial velocity field for the next step.

$$\begin{aligned}\mathbf{r}(t_1) &= a_1\mathbf{X}_1 = a_1\mathbf{X}_0 + \mathbf{p}(\mathbf{X}_0, t_1). && \text{(B.58)}\\ \dot{\mathbf{r}}(t_1) &= \dot{a}_1\mathbf{X}_1 + \dot{\mathbf{p}}(\mathbf{X}_1, t_1) && \text{(B.59)}\end{aligned}$$

$$\begin{aligned}\dot{\mathbf{p}}(\mathbf{X}_1, t_1) &= \dot{\mathbf{p}}(\mathbf{X}_0, t_1) - \frac{\dot{a}_1}{a_1}\mathbf{p}(\mathbf{X}_0, t_1), && \text{(B.60)}\\ \delta(\mathbf{X}_1, t_1) &= \frac{(1 + \delta(\mathbf{X}_0, t_0))a_1^3}{J(\mathbf{X}_0, t_1)} - 1. && \text{(B.61)}\end{aligned}$$

The physical density and velocity at the end of the previous step are obtained at the equispaced grid locations in the $\mathbf{X}_0$ space. But it is required that the initial conditions be given on the grid equispaced in the $\mathbf{X}_1$ space. This is equivalent to a non equispaced grid in the $\mathbf{X}_0$ space at time t_1.

The steps below outline the reinitialization routine.

(a) Set $t_0 = t_1$ and $t_1 = t_2$, where t_2 is the final time of interest for the next step.

(b) Get new values for a_0, H_0, $\Omega_{m,0}$, $\Omega_{d.e.,0}$. The initial conditions for the temporal functions $b^{(n,L/T)}(t)$ stay the same.

(c) Interpolate the functions in the r.h.s of eq. (B.60) and eq. (B.61) and the function $\mathbf{p}(\mathbf{X_0}, t_1)/a_1$ to obtain a symbolic function that can be evaluated at any point $\mathbf{X}_0$. Interpolation should be done using periodic functions.

(d) Solve for

$$\mathbf{X}_1^{grid} = \mathbf{X}_0 + \frac{\mathbf{p}(\mathbf{X}_0, t_1)}{a_1}. \tag{B.62}$$

This is done iteratively. $\mathbf{X}_0^{(0)} = \mathbf{X}_1^{grid}$ and solving $\mathbf{X}_0^{(1)} = \mathbf{X}_1^{grid} - \mathbf{p}(\mathbf{X}_0^{(0)}, t_1)/a_1$, $\mathbf{X}_0^{(2)} = \mathbf{X}_1^{grid} - \mathbf{p}(\mathbf{X}_0^{(1)}, t_1)/a_1$,etc. This iterative scheme involves knowing the displacement at all points (not just at grid values) in the $\mathbf{X}_0$ space. The values at the non-grid points in the $\mathbf{X}_0$ space are evaluated by interpolation of the values at the grid points in the $\mathbf{X}_0$ space.

(e) Evaluate the interpolated functions for density and velocity at the off grid points $\mathbf{X}_0$. These correspond to the new density and velocity on the equispaced grid in $\mathbf{X}_1$ space.

8. Return to step 2.

B.5 Solving Poisson's equation on the grid

This section outlines the algorithm to solve for $\nabla_X \cdot \mathbf{F} = S(\mathbf{X})$, where $\mathbf{F}$ is a longitudinal function i.e. $\nabla_X \times \mathbf{F} = 0$.

Since the function is curl-less it can be represented by $\mathbf{F} = \nabla_X \phi$. The divergence equation is then transformed to Poisson's equation

$$\nabla_X^2 \phi(\mathbf{X}) = S(\mathbf{X}) \tag{B.63}$$

and is solved by the method of Fourier transforms.

The discrete fourier representation of $\phi(x)$ at the grid point labeled by x_n in one dimensions is

$$\tilde{\phi}(k_n) = \frac{1}{\sqrt{N}} \sum_{m=1}^{N} \phi(x_m) e^{i k_n x_m} \tag{B.64}$$

and the inverse fourier transform is defined as

$$\phi(x_m) = \frac{1}{\sqrt{N}} \sum_{n=1}^{N} \tilde{\phi}(k_n) e^{-i k_n x_m}. \tag{B.65}$$

The solution to eq. (B.63) is obtained by the following steps:

1. Take the three dimensional Fourier transform of the source $\tilde{S}(\mathbf{k})$.
2. Set the zero frequency terms to be zero i.e. set $\tilde{S}(k_x = 0, k_y = 0, k_z = 0) = 0$.
3. Divide by $-(k_x^2 + k_y^2 + k_z^2)$.
4. Take inverse Fourier transform.

This gives

$$\phi(\mathbf{X}) = Inv.FT \left[\frac{\tilde{S}(\mathbf{k})}{-(k_x^2 + k_y^2 + k_z^2)} \right]. \tag{B.66}$$

To avoid the singularity at $k_x = 0, k_y = 0, k_z = 0$, the component $\tilde{S}(\mathbf{k} = \bar{0})$ is set to 0. If the original data has the property $\tilde{S}(\mathbf{k} = \bar{0})$, then this operation introduces no error. This property is equivalent to

$$\sum_{i=1}^{N_1} \sum_{j=1}^{N_2} \sum_{k=1}^{N_3} S_{i,j,k} = 0. \tag{B.67}$$

where $S_{i,j,k}$ are the values of the source on the three dimensional grid. In the continuous form this property is $\int_V dX_1 dX_2 dX_3 S(\mathbf{X}) = 0$. The initial data (which sets the first order spatial terms) is assumed to satisfy this property. At higher orders, it is necessary to check that all source terms satisfy this condition (see Appendix B.8).

B.6 Taking partial derivatives on the grid

This section outlines the algorithm to take partial derivatives using Fourier transforms.

Consider first a function $\phi(x)$ in one dimension at a grid point denoted by x_m.

$$\phi(x_m) = \frac{1}{\sqrt{N}} \sum_{n=1}^{N} \tilde{\phi}(k_n) e^{-ik_n x_m}. \tag{B.68}$$

Taking the derivative gives

$$\left.\frac{d\phi}{dx}\right|_{x_m} = \frac{1}{\sqrt{N}} \sum_{n=1}^{N} -ik_n \tilde{\phi}(k_n) e^{-ik_n x_m} \tag{B.69}$$

If $\phi(x)$ is a real function and x is a real variable, then it is required that $d\phi/dx$ be a real function of x i.e. $d\phi/dx = (d\phi/dx)^*$, where * denotes the complex conjugate. Taking complex conjugate of the previous equation gives,

$$\left.\frac{d\phi}{dx}\right|_{x_m}^{*} = \frac{1}{\sqrt{N}} \sum_{n=1}^{N} ik_n \tilde{\phi}^*(k_n) e^{ik_n x_m} \tag{B.70}$$

Consider the difference between eq. (B.69) and eq. (B.70). If ϕ is a real function then $\tilde{\phi}^*(k_n) = \tilde{\phi}(-k_n)$. The positive k values in the first term cancel the negative k terms in the second term except when $k = k_c$ since the negative Nyquist value is not explicitly represented on the grid. Thus, the discrete representation of a derivative taken using Fourier transforms has the property

$$\left.\frac{d\phi}{dx}\right|_{x_m}^{*} - \left.\frac{d\phi}{dx}\right|_{x_m} = \frac{1}{\sqrt{N}} ik_c\tilde{\phi}(k_c) = \frac{\sqrt{N}}{L}\pi i\tilde{\phi}(k_c) \tag{B.71}$$

For the derivative to be real, the quantity on the r.h.s of the above equation should be zero. Therefore, it is necessary to impose that the components corresponding to the Nyquist frequency be zero. If the function is bandwidth limited and has no power in components greater than or equal to the Nyquist frequency, the r.h.s is equal to zero and no error is made in the representation.

The algorithm for the partial derivative follows:

1. Fourier transform $\phi(\mathbf{X})$ to get $\tilde{\phi}(\mathbf{k})$.
2. Assign zeros to all the Fourier components of $\phi(\mathbf{X})$ on the entire 2-d boundary in k-space corresponding to the Nyquist frequencies i.e. $\tilde{\phi}(\mathbf{k}) = 0$ if k_x, k_y or $k_z = k_c$.
3. The partial derivative of a function with respect to the X_1 coordinate is then

$$\frac{\partial\phi}{\partial X_1} = InvF.T\left[-ik_x\tilde{\phi}(\mathbf{k})\right] \tag{B.72}$$

B.7 Solving the curl equation on the grid

All the higher order transverse functions require solving an equation of the type $\nabla \times \mathbf{F}^T = \mathbf{S}(\mathbf{X})$, where the source vector $\mathbf{S}(\mathbf{X})$ is known on a $N_1 \times N_2 \times N_3$ grid.

Since $\mathbf{F}^T$ is divergence-less, we can choose it to be of the form $\mathbf{F}^T = \nabla \times \mathbf{A}$.

$$\nabla \times \mathbf{F}^T = \nabla \times (\nabla \times \mathbf{A}) = \nabla(\nabla \cdot \mathbf{A}) - \nabla^2 \mathbf{A}. \tag{B.73}$$

It is always possible to choose $\mathbf{A}$ to satisfy $\nabla \cdot \mathbf{A} = 0$ (gauge freedom). If $\nabla \cdot \mathbf{A} \neq 0$, redefine $\mathbf{A}$ as $\mathbf{A} \to \mathbf{A} + \nabla\lambda$ where $\nabla^2\lambda = -\nabla \cdot \mathbf{A}$. $\mathbf{F}^T$ remains unchanged under this transformation. The equation to solve for then becomes

$$\nabla^2 \mathbf{A} = -\mathbf{S}(\mathbf{X}) \tag{B.74}$$

which is Poisson's equation for each component of $\mathbf{A}$ and is solved by the algorithm outlined in section (B.5).

B.8 Check that the longitudinal and source terms are compensated.

We want to prove that the volume integral of the source terms $\hat{L}[\mathbf{F}^a, \mathbf{F}^b, \mathbf{F}^c]$ and $\hat{\mathbf{T}}[\mathbf{F}^a, \mathbf{F}^b]$ is zero. Since the functions are all periodic, we denote the space as a 3-dimensional torus $\mathbf{T}^3$.

B.8.1 Longitudinal terms

To prove

$$I = \epsilon_{ijk}\epsilon_{pqr} \int_{\mathbf{T}^3} dX_1 dX_2 dX_3 \frac{\partial F_i^{(\alpha)}}{\partial X_p} \frac{\partial F_j^{(\beta)}}{\partial X_q} \frac{\partial F_k^{(\gamma)}}{\partial X_r} = 0. \tag{B.75}$$

Proof: Write $I = \epsilon_{ijk} I'$ where

$$I' = \epsilon_{pqr} \int_{\mathbf{T}^3} dX_1 dX_2 dX_3 \frac{\partial F_i^{(\alpha)}}{\partial X_p} \frac{\partial F_j^{(\beta)}}{\partial X_q} \frac{\partial F_k^{(\gamma)}}{\partial X_r} \tag{B.76}$$

First integrate over the variable corresponding to X_r. Without loss of generality, consider the case $r = 3$. Integrating by parts over X_3, we get

$$I' = \epsilon_{pq3} \int_{\mathbf{T}^3} dX_1 dX_2 \left[\frac{\partial F_i^{(\alpha)}}{\partial X_p} \frac{\partial F_j^{(\beta)}}{\partial X_q} \int dX_3 \frac{\partial F_k^{(\gamma)}}{\partial X_3} \bigg|_{\mathbf{T}^3} - \int dX_3 \frac{\partial}{\partial X_3} \left(\frac{\partial F_i^{(\alpha)}}{\partial X_p} \frac{\partial F_j^{(\beta)}}{\partial X_q} \right) F_k^{\gamma} \right] \tag{B.77}$$

The first term in the above expression is zero because F_k^{γ} is periodic and we get

$$I' = -\epsilon_{pq3} \int_{\mathbf{T}^3} dX_1 dX_2 dX_3 \frac{\partial}{\partial X_3} \left(\frac{\partial F_i^{(\alpha)}}{\partial X_p} \frac{\partial F_j^{(\beta)}}{\partial X_q} \right) F_k^{\gamma} \tag{B.78}$$

In general, for any I_{pqr},

$$\begin{aligned} I' &= -\epsilon_{pqr} \int_{\mathbf{T}^3} dX_1 dX_2 dX_3 \frac{\partial}{\partial X_r} \left(\frac{\partial F_i^{(\alpha)}}{\partial X_p} \frac{\partial F_j^{(\beta)}}{\partial X_q} \right) F_k^{\gamma} \\ &= -\epsilon_{pqr} \int_{\mathbf{T}^3} dX_1 dX_2 dX_3 \left[\left(\frac{\partial^2 F_i^{(\alpha)}}{\partial X_r \partial X_p} \right) \frac{\partial F_j^{(\beta)}}{\partial X_q} + \left(\frac{\partial^2 F_j^{(\beta)}}{\partial X_r \partial X_q} \right) \frac{\partial F_i^{(\alpha)}}{\partial X_p} \right] F_k^{\gamma} \\ &= -\epsilon_{pqr} \int_{\mathbf{T}^3} dX_1 dX_2 dX_3 \left(\frac{\partial^2 F_i^{(\alpha)}}{\partial X_r \partial X_p} \right) \frac{\partial F_j^{(\beta)}}{\partial X_q} F_c^k - \epsilon_{pqr} \int_{\mathbf{T}^3} dX_1 dX_2 dX_3 \left(\frac{\partial^2 F_j^{(\beta)}}{\partial X_r \partial X_q} \right) \frac{\partial F_i^{(\alpha)}}{\partial X_p} F_k^{\gamma} \end{aligned}$$

The first integrand is symmetric under the exchange $r \leftrightarrow p$ and the second under the exchange $r \leftrightarrow q$. ϵ_{pqr} is antisymmetric under these exchanges. Therefore, $I' = 0$ for every triplet (p, q, r) and $I = 0$.

B.8.2 Transverse terms

To prove

$$I = \int_{\mathbf{T}^3} dX_1 dX_2 dX_3 \left[-\epsilon_{nlm} \frac{\partial F_k^{(\alpha)}}{\partial X_l} \frac{\partial F_k^{(\beta)}}{\partial X_l} \right] = 0. \tag{B.79}$$

Proof: Rewrite the integrand

$$-\epsilon_{nlm} \frac{\partial F_k^{(\alpha)}}{\partial X_l} \frac{\partial F_k^{(\beta)}}{\partial X_m} = -\epsilon_{nlm} \frac{\partial}{\partial X_l} \left(F_k^{(\alpha)} \frac{\partial F_k^{(\beta)}}{\partial X_m} \right) + \epsilon_{nlm} F_k^{(\alpha)} \frac{\partial^2 F_k^{(\beta)}}{\partial X_l \partial X_m} \tag{B.80}$$

The second term is zero because of the ϵ_{nlm} is antisymmetric under exchange of l and m.

$$I = -\epsilon_{nlm} \int_{\mathbf{T}^3} \frac{\partial}{\partial X_l} \left(F_k^{(\alpha)} \frac{\partial F_k^{(\beta)}}{\partial X_m} \right) dX_1 dX_2 dX_3 \tag{B.81}$$

Consider $n = 1$ and integrate over the variable corresponding to l.

$$I = -\epsilon_{123} \int_{\mathbf{T}^3} dX_1 dX_3 \left[F_k^{(\alpha)} \frac{\partial F_k^{(\beta)}}{\partial X_m} \right]_{\mathcal{B}} + (2 \leftrightarrow 3) \tag{B.82}$$

Since all the lower order terms are periodic, the terms in the brackets evaluated on the boundary $\mathcal{B}$ add up to zero. The net integral for $n = 1$ is zero. Similarly for $n = 2, 3$.

These results ensure that the sources for all Poisson equations encountered in this scheme integrate to zero on the grid.

B.9 Setting the initial conditions along the Zeldovich curve

Zeldovich initial conditions are those for which the background and perturbation have the same big bang time. This is also equivalent to having no growing mode in the solutions. The first order solution depends on the initial density and velocity fields and in the absence of any initial transverse velocity, the first order solution is

$$\mathbf{p}^{(1)}(\mathbf{X}, t) = b_\delta(t)\mathbf{F}_\delta(\mathbf{X}) + b_v^L(t)\mathbf{F}_v^L(\mathbf{X}) \tag{B.83}$$

where b_δ and b_v^L satisfy eqs. (B.31) and (B.32).

At very early times (recombination) the universe is purely matter dominated with $\Omega \approx 1$ and the evolution of the spatial functions is

$$b_\delta(t) \;=\; -\frac{2}{5}a_0 \left(\frac{t}{t_0}\right)^{-1/3} - \frac{3}{5}a_0 \left(\frac{t}{t_0}\right)^{4/3} + a_0 \left(\frac{t}{t_0}\right)^{2/3}, \tag{B.84}$$

$$b_v(t) \;=\; -\frac{3t_0}{5}\left(\frac{t}{t_0}\right)^{-1/3} + \frac{3t_0}{5}\left(\frac{t}{t_0}\right)^{4/3}. \tag{B.85}$$

The terms $(t/t_0)^{-1/3}$ and $(t/t_0)^{4/3}$ arise from the homogenous part of the solution to the differential equation and the particular solution to eq. (B.31) scales as $(t/t_0)^{2/3}$. The net $\mathbf{p}^{(1)}$ is

$$\mathbf{p}^{(1)} = \left(\frac{t}{t_0}\right)^{-1/3}\left[-\frac{2a_0}{5}\mathbf{F}_\delta - \frac{3t_0}{5}\mathbf{F}_v^L\right] + \left(\frac{t}{t_0}\right)^{4/3}\left[-\frac{3a_0}{5}\mathbf{F}_\delta + \frac{3t_0}{5}\mathbf{F}_v^L\right] + a_0\left(\frac{t}{t_0}\right)^{2/3}\mathbf{F}_\delta. \tag{B.86}$$

"Zeldovich initial conditions" correspond to no perturbation at the big bang singularity at $t = 0$. Imposing this requirement at first order, gives a relation between the initial velocity and density field at first order.

$$\mathbf{F}_v^L = -\frac{2}{3}\cdot\frac{a_0}{t_0}\mathbf{F}_\delta = -\dot{a}(t_0)\mathbf{F}_\delta \tag{B.87}$$

Note, that this does not guarantee that there are no decaying modes at $t = 0$ from the higher order solution. The temporal derivative operator is the same at all orders and hence the homogenous part of the solution at all orders will have terms of the form $(t/t_0)^{-1/3}$. These terms will be multiplied by spatial terms $\mathbf{F}(\mathbf{X})$ which get determined by combinations of lower order terms. The other alternate way to set the initial velocity to satisfy Zeldovich conditions is to choose the velocity at each point based on the non-linear Zeldovich condition given by the spherical top-hat. In this case, the relationship in eq. (B.87) is not satisfied and although the velocity and density lie on the non-linear top-hat Zeldovich curve, decaying terms are present already at first order. The first prescription is used more often in literature and in this paper. For simulations starting at recombination, the differences in the two ways of setting the initial conditions are very small ($\sim 10^{-8}$).

B.10 Spherical tophat

This section describes the details involved in setting up the compensated top-hat configurations for sections 4.4.1 and 4.4.2

The exact compensated top-hat function consists of a spherical overdense region surrounded by a compensating underdense vacuum region. Let a and b be the radii of the overdense and compensating regions respectively. The initial density profile is given by

$$\rho(X,t_i) = \begin{cases} (1+\delta_i) & 0 \le X < a \\ 0 & a \le X < b \\ 1 & X \ge b \end{cases} \tag{B.88}$$

where $X = |\mathbf{X}|$. The choice of δ and a determines the width of the vacuum region $b - a$. Making δ too small makes it difficult to resolve the vacuum region with a moderate size (64^3) grid. Set $\delta_i = 10$ $a = 1/4$ and $b = 11^{1/3}/4$. The box length L_{box} is chosen to be two units in length centered around the point $(1/10, -1/11, 1/(2\pi))$. The choice of parameters ensures that the entire profile is well represented within the box and the offset ensures that no special symmetry is exploited in the test. The profile is discontinuous at $X = a$ and $X = b$. The Fourier transform of a discontinuous function has power at all wavenumbers and the Gibbs phenomenon prevents such functions from being completely represented by Fourier transforms on any finite size grid. In order, to get smooth initial conditions, this profile is smoothed with a gaussian filter of width σ. The smoothed density profile is

$$\rho_\sigma(X,t_i) = \int_0^{L_{box}} \rho(X,t_i) \cdot \frac{\exp(-X^2/2\pi\sigma^2)}{(2\pi\sigma^2)^{3/2}} d^3X \tag{B.89}$$

where $\rho(X,t_i)$ is given by eq. (B.88). The smoothing is performed analytically in real space and the smoothed function is then evaluated on the grid. In order to ensure periodicity of the initial conditions, the contribution from twenty six nearest neighbors was added.

For the profile in section 4.4.1, the smoothing parameter is varied inversely with the grid size so that the original top-hat is recovered in the limit that $\sigma \to 0$ and $N_s \to \infty$. The justification for this choice is described below. For the density profile in section 4.4.2, the smoothing parameter is fixed at $\sigma = 1/18$ and only the grid size N_s is varied.

B.10.1 Scaling of the error

There are two sources of error between the analytic and numerical initial density. One arises from the smoothing and the other from the discrete representation of the discontinuous top-hat. The former dominates when the smoothing width is large and the latter when the when the width is small. Thus, for a fixed N, there is a certain value of σ for which the net error (smoothing + Gibbs error) is minimum.

Consider the difference between the original discontinuous top-hat and its smoothed version represented on a discrete grid with N_s points along each axis. Figure B.1 shows a schematic representation of the transition boundary at $X = a$. The error between the exact step and its smooth version occurs in the transition region whose width scales proportional to the smoothing parameter σ. If the transition region is defined to be between ninety and ten percent of the maximum, the width of the transition region is approximately 1.5 σ. If L is the length of the box, then $\bar{n} = N_s^3/L^3$ is the density of points in the transition region. The value of the function is underestimated for half of these points and overestimated for the other half and volume of the region is $4\pi a^2 \cdot 1.5\sigma$. Therefore, the root mean square error in the representation of the function is $\approx \sqrt{\frac{1}{N_s^3} \cdot \left(\frac{A}{2}\right)^2 \cdot 4\pi a^2 \cdot (1.5\sigma) \cdot \bar{n}}$ which scales as $\sqrt{\sigma}$.

The aliasing error arises because the top-hat function is discontinuous and therefore its fourier transform is not bandwidth limited. This gives rise to the Gibbs phenomenon or ringing artifacts in the step function. The overshoot is around 20% of the maximum value and mainly occurs along the discontinuous surface. Since the surface is represented by N_s^2 points the r.m.s Gibbs error scales as $\sqrt{1/N_s^3 \cdot N_s^2} \sim 1/\sqrt{N_s}$. In order to balance the smoothing error and the Gibbs error the scaling $\sigma \sim 1/N_s$ was chosen.

B.10.2 Effect of periodic boundary conditions

The exact solution is known for a single isolated top-hat initial configuration. However, the solution using Fourier transforms assumes that the system is periodic. The evolution of an isolated system and a periodic system is different because in the latter system, matter in each box will be affected by the force due to the matter in the neighboring boxes. The ideal limit of an isolated system is attained only in the limit that the box size is increased along with the resolution N_s. However, for the sphere, the total contribution to the force from neighbors arises only from the monopole term which is set exactly to zero because the density is compensated. Because of spherical symmetry and the fact that the inner and outer spheres have the same center, all the higher multipole moments in potential are zero. So, the copies do not exert any force on the central box. Thus it suffices to consider the convergence of sequence of answers obtained by

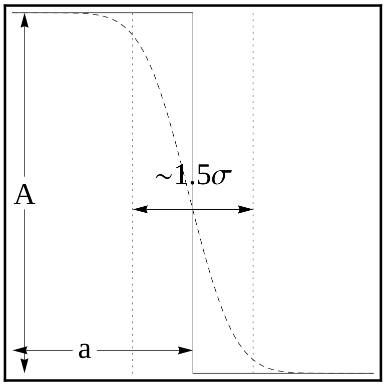

Figure B.1: Schematic representation of the error due to smoothing a step function by convolving it with a Gaussian. As the width of the transition region decreases, the smooth function approaches the discontinuous top-hat.

simultaneously decreasing σ and increasing N_s. The box size does not need to be changed.

B.11 Realizing a Gaussian field

The initial fractional overdensity $\delta(\mathbf{x})$ can be written as as a series expansion in terms of its Fourier coefficients

$$\delta(\mathbf{x}) = \frac{V}{(2\pi)^3} \int \tilde{\delta}(\mathbf{k}) e^{-i\mathbf{k}\cdot\mathbf{x}} d^3k \tag{B.90}$$

where $\tilde{\delta}(\mathbf{k})$ satisfies

$$\langle \tilde{\delta}(\mathbf{k}) \tilde{\delta}(\mathbf{k}') \rangle = \frac{2\pi^2 P(k)}{V} \tag{B.91}$$

where V is the volume of the box, and $P(k)$ is the matter power spectrum. The finite resolution of the numerical grid, requires smoothed initial distributions.

The Fourier coefficients of the smoothed density on any scale R are given by $\tilde{\delta}_R(\mathbf{k}) = W(k, R)\tilde{\delta}(\mathbf{k})$, where $W(k, R)$ is the smoothing window function. The window function has the form $W(k, R) = e^{-1/2(kR)^2}$ for a Gaussian k-space filter. The shape of the linear power spectrum is chosen to be

$$P(k) = \frac{k^n}{(1 + P_2 k^{1/2} + P_3 k + P_r k^{3/2} + P_5 k^2)^{2P_6}} \tag{B.92}$$

The coefficients P_i are given in Klypin [41] and $n = 1$. $P(k)$ is normalized so that $\sigma_8 \equiv \sigma(R = 8h^{-1}\text{Mpc}) = 0.8$, where the variance of the density fluctuation smoothed on a scale R is

$$\sigma_R^2 = \int_0^\infty P(k) W(k, R)^2 k^2 dk. \tag{B.93}$$

where $W(k, R)$ is the Fourier transform of the window function in real space.

The form for $P(k)$ above is the linear matter power spectrum today. To set initial conditions at any starting scale factor a, requires multiplication by the corresponding growth factors.

$$P(k, a) = P(k) \left(\frac{D(a)}{D(a = 1)} \right)^2 \tag{B.94}$$

where the growth function $D(a)$ is

$$D(a) = \frac{5}{2} \Omega_m \frac{H(a)}{H_0} \int_0^a \frac{da'}{(a' H(a') H_0)^3}. \tag{B.95}$$

In the above expression $H(a)$ is the Hubble parameter and H_0 is its value at the initial time. The finite size of the simulation grid requires the discrete version of the definition of Fourier transform which is given as

$$\delta(\mathbf{k}) = \sum \tilde{\delta}(\mathbf{k}) e^{-i\mathbf{k}\cdot\mathbf{x}} \tag{B.96}$$

Note, here that an implementation in *Mathematica* will have to account for the differences of normalization in the definition of Fourier transforms. The prescription here is not generic to any particular implementation. The prescription for each $\tilde{\delta}(\mathbf{k})$ is

$$\tilde{\delta}(\mathbf{k}) = \sqrt{\frac{2\pi^2 P(k)}{L^3}} (a_k + i b_k) \tag{B.97}$$

where a_k, b_k are gaussian random numbers with mean zero and variance 1.

For the initial densities in sections 4.4.3 and 4.4.4, the box size was taken to be $L_{box} = 100$, $N_s = 16$ and the initial power spectrum was smoothed over 50 Mpc using a gaussian filter, followed by a sharp k-space truncation for $k > k_{niq}/2$.

APPENDIX C

APPENDIX FOR CHAPTER 5

C.1 Time dependence of the Zeldovich condition for dark energy

The evolution of the background and perturbation in the presence of dark energy is

$$\begin{aligned}\frac{\ddot{a}}{a} &= -\frac{H_i^2}{2}\left(\frac{\Omega_{m,i}a_i^3}{a^3} + (1+3w)\Omega_{d.e,i}\left(\frac{a_i}{a}\right)^{f(a)}\right) && \text{(C.1)}\\ \frac{\ddot{b}}{b} &= -\frac{H_i^2}{2}\left(\frac{\Omega_{m,i}a_i^3(1+\delta_i)}{b^3} + (1+3w)\Omega_{d.e,i}\left(\frac{a_i}{a}\right)^{f(a)}\right) && \text{(C.2)}\end{aligned}$$

where $H_i, \Omega_{m,i}, \Omega_{d.e,i}$ are the Hubble parameter and density parameters at the initial time t_i and are related as

$$\begin{aligned}\Omega_{m,i} &= \Omega_{m,0}\frac{H_0^2}{H_i^2 a_i^3} = \frac{\Omega_{m,0}a_i^{-3}}{\Omega_{m,0}a_i^{-3} + \Omega_{d.e,0}a_i^{-3(1+w)}} && \text{(C.3)}\\ \Omega_{de,i} &= \Omega_{d.e,0}\frac{H_0^2}{H_i^2 a_i^3} = \frac{\Omega_{d.e,0}a_i^{-3(1+w)}}{\Omega_{m,0}a_i^{-3} + \Omega_{d.e,0}a_i^{-3(1+w)}} && \text{(C.4)}\end{aligned}$$

where $\Omega_{m,0}, \Omega_{d.e,0}, H_0$ are the values of the density parameters and Hubble constant today. The initial conditions are $a(t_i) = a_i, \dot{a}(t_i) = \dot{a}_i, b(t_i) = a_i$ and $\dot{b}(t_i) = \dot{a}_i(1+\delta_{v,i})$.

For a pure matter universe the perturbation equation can be integrated to get a first order equation for $b(t)$ and an expression for the bang time, but for a general dark energy term this cannot be done analytically. The bang time for the perturbation is evaluated by numerically integrating the second order equation. One can then solve for the pair $(\delta_0, \delta_{v,0})$ which gives the same bang times for the background and the perturbation. In the case of pure matter, this pair is independent of the initial starting time t_i. But for general dark energy models, it depends on time. This can be seen by changing variables $x = a/a_i, y = b/a_i$, $t' = t_i H_i$. The two equations then read

$$\frac{d^2x}{dt'^2} = -\frac{1}{2}\left(\frac{\Omega_{m,i}}{x^3} + (1+3w)\Omega_{d.e,i}\left(\frac{1}{x}\right)^{3(1+w)}\right), \tag{C.5}$$

$$\frac{d^2y}{dt'^2} = -\frac{1}{2}\left(\frac{\Omega_{m,i}(1+\delta_i)}{y^3} + (1+3w)\Omega_{d.e,i}\left(\frac{1}{x}\right)^{3(1+w)}\right), \tag{C.6}$$

with initial conditions $x(t'_i) = 1, \dot{x}(t'_i) = 1, y(t'_i) = 1, \dot{y}(t'_i) = (1 + \delta_{v,i})$ where the dots denote the derivative with respect to. t'. For a pure matter universe $\Omega_{d.e,i} = 0$ and $\Omega_{m,i} = 1$ for all starting times. The bang time for the background in these units is 2/3 and the pair $\delta_i, \delta_{v,i}$ is independent of t_i. However, the presence of the dark energy term implies that $\Omega_{m,i}$ and $\Omega_{d.e,i}$ change with time (eq. (C.4)) and this implies that the equal bang time pair $(\delta_i, \delta_{v,i})$ is no longer independent of t_i.

The situation is somewhat subtle when the dark energy is not a cosmological constant. For cosmologies with $w > -1$, the equation for the perturbation is singular when the scale factor of the background $a(t) = 0$. Therefore, the bang time for the perturbation is always greater than or equal to the bang time for the background. However, it is still possible to find a unique value of δ_v for which the bang times are equal. The Zeldovich curves for different cosmologies are plotted in the text.

BIBLIOGRAPHY

[1] Susanne Adler and Thomas Buchert. Lagrangian theory of structure formation in pressure-supported cosmological fluids. Astronomy and Astrophysics, 343:317324, March 1999.

[2] Andreas Albrecht and Constantinos Skordis. Phenomenology of a realistic accelerating universe using only Planck-Scale physics. Physical Review Letters, 84:2076–2079, March 2000.

[3] J. S. Bagla and T. Padmanabhan. Cosmological n-body simulations. Pramana, 49:161, August 1997.

[4] M. Bartelmann, M. Doran, and C. Wetterich. Non-linear structure formation in cosmologies with early dark energy. Astronomy and Astrophysics, 454:27–36, July 2006.

[5] N. Bartolo, E. Komatsu, S. Matarrese, and A. Riotto. Non-Gaussianity from inflation: Theory and observations. astro-ph/0406398, June 2004. Phys.Rept. 402 (2004) 103-266.

[6] C. M. Baugh, E. Gaztañaga, and G. Efstathiou. A comparison of the evolution of density fields in perturbation theory and numerical simulations - II. counts-in-cells analysis. Monthly Notices of the Royal Astronomical Society, 274:1049–1070, June 1995.

[7] Rachel Bean, Steen H. Hansen, and Alessandro Melchiorri. Early-universe constraints on dark energy. Physical Review D, 64:103508, November 2001.

[8] F. Bernardeau, M. J. Chodorowski, E. L. Lokas, R. Stompor, and A. Kudlicki. Non-linearity and stochasticity in the density-velocity

relation. Monthly Notices of the Royal Astronomical Society, 309:543–555, October 1999.

[9] F. Bernardeau, S. Colombi, E. Gaztañaga, and R. Scoccimarro. Large-scale structure of the universe and cosmological perturbation theory. Physics Reports, 367:13, September 2002.

[10] Francis Bernardeau. The quasi-Gaussian density-velocity relationship. The Astrophysical Journal, 390:L61–L64, May 1992.

[11] Edmund Bertschinger. Simulations of structure formation in the universe. Annual Review of Astronomy and Astrophysics, 36:599654, 1998.

[12] Maciej Bilicki and Michal Chodorowski. The velocity-density relation in the spherical model. 0809.3513, September 2008.

[13] F. R Bouchet. Introductory overview of eulerian and lagrangian perturbation theories. astro-ph/9603013, March 1996.

[14] F. R. Bouchet, S. Colombi, E. Hivon, and R. Juszkiewicz. Perturbative lagrangian approach to gravitational instability. Astronomy and Astrophysics, 296:575, April 1995.

[15] F. R. Bouchet, R. Juszkiewicz, S. Colombi, and R. Pellat. Weakly nonlinear gravitational instability for arbitrary omega. Astrophysical Journal, 394:L5L8, July 1992.

[16] Y. Brenier, U. Frisch, M. Henon, G. Loeper, S. Matarrese, R. Mohayaee, and A. Sobolevski. Reconstruction of the early universe as a convex optimization problem. Monthly Notices of the Royal Astronomical Society, 346:501–524, December 2003.

[17] T. Buchert. Lagrangian theory of gravitational instability of Friedman-Lemaitre cosmologies - a generic Third-Order model for nonlinear clustering. Monthly Notices of the Royal Astronomical Society, 267:811, April 1994.

[18] T. Buchert. Lagrangian perturbation approach to the formation of large-scale structure. astro-ph/9509005, September 1995. IOP Press Amsterdam (1996) 543-564.

[19] T. Buchert, A. Dominguez, and J. Perez-Mercader. Extending the scope of models for large-scale structure formation in the universe. Astronomy and Astrophysics, 349:343353, September 1999.

[20] Thomas Buchert. Lagrangian theory of gravitational instability of Friedman-Lemaitre cosmologies and the 'Zel'dovich approximation'. Monthly Notices of the Royal Astronomical Society, 254:729737, February 1992.

[21] Thomas Buchert and Jurgen Ehlers. Lagrangian theory of gravitational instability of Friedman-Lemaitre cosmologies second-order approach: an improved model for non-linear clustering. Monthly Notices of the Royal Astronomical Society, 264:375387, September 1993.

[22] R. R. Caldwell, Rahul Dave, and Paul J. Steinhardt. Cosmological imprint of an energy component with general equation of state. Physical Review Letters, 80:1582–1585, February 1998.

[23] Jordan Carlson, Martin White, and Nikhil Padmanabhan. A critical look at cosmological perturbation theory techniques. 0905.0479, May 2009. Phys.Rev.D80:043531,2009.

[24] Paolo Catelan. Lagrangian dynamics in Non-Flat universes and Non-Linear gravitational evolution. *astro-ph/9406016*, June 1994. Mon.Not.Roy.Astron.Soc.276:115,1995.

[25] C. Chicone. *Ordinary Differential Equations with Applications, 2nd Edition (section 1.1, 1.12)*. Texts in Applied Mathematics, New York: Springer-Verlag, 2006.

[26] Asantha Cooray, Daniel E Holz, and Robert Caldwell. Measuring dark energy spatial inhomogeneity with supernova data. *0812.0376*, December 2008.

[27] Martn Crocce, Sebastin Pueblas, and Romn Scoccimarro. Transients from initial conditions in cosmological simulations. *Monthly Notices of the Royal Astronomical Society*, 373:369381, November 2006.

[28] Neal Dalal, Olivier Doré, Dragan Huterer, and Alexander Shirokov. The imprints of primordial non-gaussianities on large-scale structure: scale dependent bias and abundance of virialized objects. *0710.4560*, October 2007. Phys.Rev.D77:123514,2008.

[29] Avishai Dekel. Dynamics of cosmic flows. *Annual Review of Astronomy and Astrophysics*, 32:371–418, 1994.

[30] Michael Doran and Georg Robbers. Early dark energy cosmologies. *astro-ph/0601544*, January 2006. JCAP 0606 (2006) 026.

[31] Jurgen Ehlers and Thomas Buchert. Newtonian cosmology in lagrangian formulation: Foundations and perturbation theory. *General Relativity and Gravitation*, 29:733764, June 1997.

[32] Daniel J. Eisenstein, Hee-Jong Seo, Edwin Sirko, and David N. Spergel. Improving cosmological distance measurements by reconstruction of the baryon acoustic peak. Astrophysical Journal, 664:675679, August 2007.

[33] Daniel J. Eisenstein, Hee-Jong Seo, and Martin White. On the robustness of the acoustic scale in the Low-Redshift clustering of matter. Astrophysical Journal, 664:660674, August 2007.

[34] Matthew J Francis, Geraint F Lewis, and Eric V Linder. Can early dark energy be detected in Non-Linear structure? 0808.2840, August 2008. Mon.Not.Roy.Astron.Soc.394:605-614,2008.

[35] Uriel Frisch, Sabino Matarrese, Roya Mohayaee, and Andrei Sobolevski. A reconstruction of the initial conditions of the universe by optimal mass transportation. Nature, 417:260–262, May 2002.

[36] Margherita Grossi and Volker Springel. The impact of early dark energy on non-linear structure formation. 0809.3404, September 2008.

[37] Daniel E Holz and Robert M Wald. A new method for determining cumulative gravitational lensing effects in inhomogeneous universes. astro-ph/9708036, August 1997. Phys.Rev. D58 (1998) 063501.

[38] Brown J.W. and Churchill R.V. Complex Variables and Applications. Weily, 1996.

[39] G. Karakatsanis, T. Buchert, and A. L. Melott. Temporal optimization of lagrangian perturbation schemes. Astronomy and Astrophysics, 326:873–884, October 1997.

[40] Masumi Kasai. Tetrad-based perturbative approach to inhomogeneous universes: A general relativistic version of the zel'dovich approximation.

Physical Review D, 52(10):5605, November 1995. Copyright (C) 2009 The American Physical Society; Please report any problems to prola@aps.org.

[41] Anatoly Klypin. Numerical simulations in cosmology i: Methods. astro-ph/0005502, May 2000.

[42] E. Komatsu, J. Dunkley, M. R. Nolta, C. L. Bennett, B. Gold, G. Hinshaw, N. Jarosik, D. Larson, M. Limon, L. Page, D. N. Spergel, M. Halpern, R. S. Hill, A. Kogut, S. S. Meyer, G. S. Tucker, J. L. Weiland, E. Wollack, and E. L. Wright. Five-Year wilkinson microwave anisotropy probe observations: Cosmological interpretation. Astrophysical Journal Supplement Series, 180:330376, February 2009.

[43] E. Komatsu, K. M. Smith, J. Dunkley, C. L. Bennett, B. Gold, G. Hinshaw, N. Jarosik, D. Larson, M. R. Nolta, L. Page, D. N. Spergel, M. Halpern, R. S. Hill, A. Kogut, M. Limon, S. S. Meyer, N. Odegard, G. S. Tucker, J. L. Weiland, E. Wollack, and E. L. Wright. Seven-Year wilkinson microwave anisotropy probe (WMAP) observations: Cosmological interpretation. http://adsabs.harvard.edu/abs/2010arXiv1001.4538K, January 2010.

[44] Ofer Lahav, Per B. Lilje, Joel R. Primack, and Martin J. Rees. Dynamical effects of the cosmological constant. Monthly Notices of the Royal Astronomical Society, 251:128–136, July 1991.

[45] Landau and Lifschitz. Complex Variables and Applications. Weily, 1996.

[46] Eric V Linder and Adrian Jenkins. Cosmic structure growth and dark energy. astro-ph/0305286, May 2003. Mon.Not.Roy.Astron.Soc. 346 (2003) 573.

[47] Eric V. Linder and Georg Robbers. Shifting the universe: early dark energy and standard rulers. Journal of Cosmology and Astro-Particle Physics, 06:004, June 2008.

[48] Eric V Linder and Martin White. Going nonlinear with dark energy cosmologies. astro-ph/0508401, August 2005. Phys.Rev.D72:061304,2005.

[49] Chung-Pei Ma. Analytical approximation to the nonlinear power spectrum of gravitational clustering. The Astrophysical Journal, 508:L5L8, November 1998.

[50] Chung-Pei Ma, R. R. Caldwell, Paul Bode, and Limin Wang. The mass power spectrum in quintessence cosmological models. The Astrophysical Journal, 521:L1L4, August 1999.

[51] S. Matarrese, O. Pantano, and D. Saez. A relativistic approach to gravitational instability in the expanding universe - Second-Order lagrangian solutions. Monthly Notices of the Royal Astronomical Society, 271:513, December 1994.

[52] Sabino Matarrese, Ornella Pantano, and Diego Saez. General-relativistic approach to the nonlinear evolution of collisionless matter. Physical Review D, 47:13111323, February 1993.

[53] Sabino Matarrese and David Terranova. Post-Newtonian cosmological dynamics in lagrangian coordinates. Monthly Notices of the Royal Astronomical Society, 283:400418, November 1996.

[54] Patrick McDonald, Hy Trac, and Carlo Contaldi. Dependence of the non-linear mass power spectrum on the equationof state of dark energy.

Monthly Notices of the Royal Astronomical Society, 366:547556, February 2006.

[55] Pierluigi Monaco. A lagrangian dynamical theory for the mass function of cosmic structures - i. dynamics. Monthly Notices of the Royal Astronomical Society, 287:753770, June 1997.

[56] David F. Mota, Douglas J. Shaw, and Joseph Silk. On the magnitude of dark energy voids and overdensities. The Astrophysical Journal, 675:2948, March 2008.

[57] F. Moutarde, J.-M. Alimi, F. R. Bouchet, R. Pellat, and A. Ramani. Precollapse scale invariance in gravitational instability. Astrophysical Journal, 382:377381, December 1991.

[58] Dipak Munshi, Varun Sahni, and Alexei A Starobinsky. Non-Linear approximations to gravitational instability: A comparison in the Quasi-Linear regime. astro-ph/9402065, February 1994. Astrophys.J. 436 (1994) 517.

[59] Sharvari Nadkarni-Ghosh and David F Chernoff. Extending the domain of validity of the lagrangian approximation. 1005.1217, May 2010.

[60] Adi Nusser, Avishai Dekel, Edmund Bertschinger, and George R. Blumenthal. Cosmological velocity-density relation in the quasi-linear regime. The Astrophysical Journal, 379:6–18, September 1991.

[61] Boyd John. P. Chebyshev and Fourier Spectral Methods, chapter 1(see online version). Dover, New York, 2001.

[62] J. A. Peacock and S. J. Dodds. Non-linear evolution of cosmological power

spectra. Monthly Notices of the Royal Astronomical Society, 280:L19L26, June 1996.

[63] P. J. E. Peebles. The peculiar velocity field in the local supercluster. The Astrophysical Journal, 205:318–328, April 1976.

[64] W. J. Percival. Cosmological structure formation in a homogeneous dark energy background. Astronomy and Astrophysics, 443:819830, December 2005.

[65] S. Perlmutter, G. Aldering, G. Goldhaber, R. A. Knop, P. Nugent, P. G. Castro, S. Deustua, S. Fabbro, A. Goobar, D. E. Groom, I. M. Hook, A. G. Kim, M. Y. Kim, J. C. Lee, N. J. Nunes, R. Pain, C. R. Pennypacker, R. Quimby, C. Lidman, R. S. Ellis, M. Irwin, R. G. McMahon, P. Ruiz-Lapuente, N. Walton, B. Schaefer, B. J. Boyle, A. V. Filippenko, T. Matheson, A. S. Fruchter, N. Panagia, H. J. M. Newberg, W. J. Couch, and The Supernova Cosmology Project. Measurements of omega and lambda from 42 High-Redshift supernovae. The Astrophysical Journal, 517:565–586, June 1999.

[66] Peebles P.J.E. Principles of Physical Cosmology (chapter 10, pages 268-269). Princeton University Press, 1993.

[67] W.H. Press, S.A. Teukolsky, W.T. Vetterling, and B.P. Flannery. Numerical Recipes in C++. Cambridge University Press, 2002.

[68] Adam G. Riess, Alexei V. Filippenko, Peter Challis, Alejandro Clocchiatti, Alan Diercks, Peter M. Garnavich, Ron L. Gilliland, Craig J. Hogan, Saurabh Jha, Robert P. Kirshner, B. Leibundgut, M. M. Phillips, David Reiss, Brian P. Schmidt, Robert A. Schommer, R. Chris Smith, J. Spyromilio,

Christopher Stubbs, Nicholas B. Suntzeff, and John Tonry. Observational evidence from supernovae for an accelerating universe and a cosmological constant. The Astronomical Journal, 116:1009–1038, September 1998.

[69] Varun Sahni and Peter Coles. Approximation methods for non-linear gravitational clustering. astro-ph/9505005, May 1995. Phys.Rept.262:1-135,1995.

[70] Varun Sahni and Sergei Shandarin. Accuracy of lagrangian approximations in voids. Monthly Notices of the Royal Astronomical Society, 282:641645, September 1996.

[71] Roman Scoccimarro. Transients from initial conditions: a perturbative analysis. Monthly Notices of the Royal Astronomical Society, 299:10971118, October 1998.

[72] Roman Scoccimarro and Ravi K. Sheth. PTHALOS: a fast method for generating mock galaxy distributions. Monthly Notices of the Royal Astronomical Society, 329:629640, 2002.

[73] Edwin Sirko. Initial conditions to cosmological N-Body simulations, or, how to run an ensemble of simulations. The Astrophysical Journal, 634:728–743, November 2005.

[74] R. E. Smith, J. A. Peacock, A. Jenkins, S. D. M. White, C. S. Frenk, F. R. Pearce, P. A. Thomas, G. Efstathiou, and H. M. P. Couchman. Stable clustering, the halo model and non-linear cosmological power spectra. Monthly Notices of the Royal Astronomical Society, 341:13111332, June 2003.

[75] Volker Springel, Simon D. M White, Adrian Jenkins, Carlos S Frenk, Naoki Yoshida, Liang Gao, Julio Navarro, Robert Thacker, Darren Croton, John Helly, John A Peacock, Shaun Cole, Peter Thomas, Hugh Couchman, August Evrard, Joerg Colberg, and Frazer Pearce. Simulating the joint evolution of quasars, galaxies and their large-scale distribution. astro-ph/0504097, April 2005. Nature 435:629-636,2005.

[76] Michael A Strauss and Jeffrey A Willick. The density and peculiar velocity fields of nearby galaxies. astro-ph/9502079, February 1995. Phys.Rept.261:271-431,1995.

[77] Takayuki Tatekawa. Improving the lagrangian perturbative solution for a cosmic fluid: Applying shanks transformation. Physical Review D, 75:44028, February 2007.

[78] Richard C. Tolman. Effect of inhomogeneity on cosmological models. Proceedings of the National Academy of Science, 20:169176, March 1934.

[79] R. Ali Vanderveld, Éanna Flanagan, and Ira Wasserman. Luminosity distance in "Swiss cheese" cosmology with randomized voids. i. single void size. Physical Review D, 78:83511, October 2008.

[80] Christian Wagner, Licia Verde, and Lotfi Boubekeur. N-body simulations with generic non-Gaussian initial conditions i: Power spectrum and halo mass function. 1006.5793, June 2010.

[81] C. Wetterich. Cosmologies with variable newton's "constant". Nuclear Physics B, 302:645–667, June 1988.

[82] C. Wetterich. Phenomenological parameterization of quintessence. Physics Letters B, 594:17–22, July 2004.

[83] Inc. Wolfram Research. Mathematica Edition: Version 7.0.1. Wolfram Research, Inc. Place of publication: Champaign, Illinois, 2008.

[84] Ya. B. Zel'Dovich. Gravitational instability: An approximate theory for large density perturbations. Astronomy and Astrophysics, 5:8489, March 1970.